

Physical Modelling of Complex Systems

Thibeau Wouters

May 24, 2021

Contents

1 Population dynamics	1
1.1 Logistic growth	1
1.2 Sustained Harvesting	3
1.3 Gompertz Law	6
1.4 Delays	8
2 Concepts of non-linear dynamics	11
2.1 Rabbit versus sheep	11
2.2 Classification of linear systems	15
2.3 Phase portrait in two dimensions	17
3 Quasi steady state approximation	20
3.1 Linear example of quasi steady-state approximation	20
3.2 Enzymatic degradation	22
3.3 Two subunit enzyme	25

4 Motifs	28
4.1 Motifs in the E. Coli Gene Regulatory Network	28
4.1.1 Selfregulation	28
4.1.2 Feed forward loops	29
4.2 Positively autoregulated protein	30
4.3 Genetic toggle switch	34
5 Non-linear oscillators and limit cycles	39
5.1 The Goodwin model	39
5.1.1 Three components	39
5.1.2 Generalization to N components	44
6 Chaos	46
6.1 The Lorenz system	46
6.1.1 From waterwheel to Lorenz	46
6.1.2 Fixed points of the Lorenz equations	47
6.1.3 Hopf bifurcation	49
6.2 The Rössler system	50
6.2.1 Numerical exploration and orbit diagram	50
6.2.2 Fixed points and stability	53
6.2.3 1D map for the Rössler system	55
6.3 The logistic map	57
6.3.1 Behaviour of the dynamics as a function of r	57
6.3.2 Orbit diagram	65
6.4 The sine and tent map	67
6.4.1 Orbit diagrams	67

6.4.2	Comparison with the logistic map	71
7	Synchronization	73
7.1	The period of a non-uniform oscillator	73
7.2	Triangle wave in firefly model	74
7.2.1	Comparison between firefly models	78
8	Travelling wave solutions of reaction diffusion models	80
8.1	Fisher-Kolmogorov equation	80
8.1.1	Minimal speed and the phase portrait method	80
8.1.2	Numerical integration	81
8.1.3	Approximate solution	85
8.2	Travelling waves in bistable systems	88
8.2.1	Spatial dynamical system and fixed points	88
8.2.2	Heteroclinic orbit and wavelike solution	89
8.3	Special solution of the Fisher-Kolmogorov equation	92
9	Pattern formation	95
9.1	Homogeneous steady state solutions	95
9.2	Turing instability	96
9.3	Spatiotemporal dynamics	100
9.3.1	Varying b	102
9.3.2	Varying initial condition	103
9.3.3	Varying domain size	106

1 Population dynamics

1.1 Logistic growth

We solve the logistic equation

$$\dot{N} = \alpha N \left(1 - \frac{N}{K}\right), \quad (1.1.1)$$

via the change of variables $y = 1/N$, with initial condition $N = N_0$. We have $\dot{y} = -1/N^2 \dot{N}$ and $y(0) = 1/N_0$, so that

$$\dot{y} = -\frac{1}{N^2} \dot{N} = -\alpha y + \frac{\alpha}{K}. \quad (1.1.2)$$

It is easy to see that a solution to this equation, with the correct initial condition, is given by

$$y(t) = \left(\frac{1}{N_0} - \frac{1}{K}\right) e^{-\alpha t} + \frac{1}{K}. \quad (1.1.3)$$

From this, we can find the solution for N , by using $y = 1/N$. This results in

$$N(t) = \frac{N_0 K}{N_0 + (K - N_0)e^{-\alpha t}} = \frac{K}{1 + \left(\frac{K-N_0}{N_0}\right) e^{-\alpha t}}. \quad (1.1.4)$$

We now solve the above differential equation numerically. For this, a function in Python is written which discretizes time into N time steps of equal length Δt , such that the differential equation $\dot{N} = f(N)$ is solved by iteratively solving $N(t + \Delta t) \approx N(t) + f(N(t))\Delta t$. In Figure 1.1.1 below, we plot the exact solution, given by equation (1.1.4), along with the solution obtained by the numerical method for $\alpha = 3$ and $K = 10^3$. One solution has initial condition $N_0 = 10$, while the other has $N_0 = 10^5$. The two graphs clearly coincide in both cases.

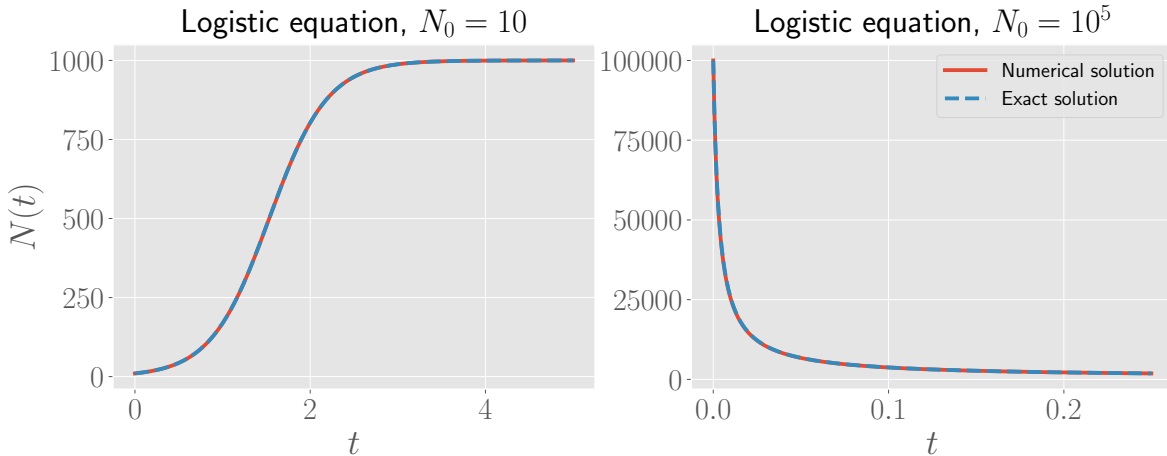


Figure 1.1.1: Exact and numerically obtained solutions to the logistic differential equation, for $\alpha = 3$ and $K = 10^3$. *Left:* for $N_0 = 10$. *Right:* for $N_0 = 10^5$.

The two fixed points of the logistic equation (1.1.1) are

$$N_1^* = 0, \quad N_2^* = K. \quad (1.1.5)$$

We now perform a linear stability analysis of this differential equation around the fixed point $N^* = K$. Using $f(N^*) = 0$ by definition of fixed point, the Taylor expansion gives for $N \approx N^*$

$$\dot{N} = f(N) \approx f'(N^*)(N - N^*) + \dots \quad (1.1.6)$$

We define $\eta(t) = N(t) - N^*$, such that the solution to the linearised equation is given by

$$\eta(t) = A e^{\pm t/\tau}, \quad \tau = \frac{1}{|f'(N^*)|}, \quad (1.1.7)$$

where the sign in the exponent is the sign of $f'(N^*)$ and τ is a characteristic relaxation time. A short computation shows

$$f'(N) = \alpha - \frac{2\alpha N}{K}, \quad (1.1.8)$$

such that $f'(N^*) = -\alpha < 0$. Hence the fixed point N^* is a stable fixed point, and the characteristic relaxation time is $\tau = 1/\alpha$. This was already clear from the two specific examples discussed in Figure 1.1.1: the solutions tend towards the value K , as is clear by letting $t \rightarrow +\infty$ in the exact solution (1.1.4). The long time behaviour we expect to see is an exponential in time as given by equation (1.1.7). Indeed, after a large amount of time, the system should be close to the fixed point, at which the linear approximation should be correct, of which the solution is an exponential.

We verify the above statements graphically. We plot $\log |\eta(t)| = \log |N(t) - N^*|$ as a function of t . According to our earlier remarks, we expect the plot to represent a straight line for large enough time periods. In Figure 1.1.2 below, this is indeed the case, for both the exact as well as the numerically obtained solutions shown in Figure 1.1.1. The long time behaviour indeed follows a straight line with slope close to $-\frac{1}{\tau} = -3$.

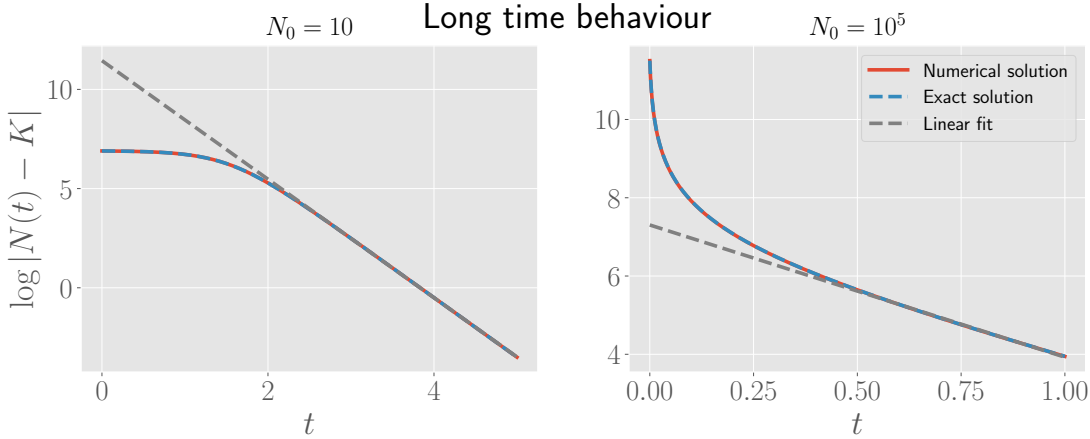


Figure 1.1.2: Long time behaviour of the solutions shown in Figure 1.1.1. The grey dashed line represents a linear fit through the second half of the data (for more details, see the notebook). *Left:* $N_0 = 10$, the slope of the fit is -2.9873 . *Right:* $N_0 = 10^5$, the slope of the fit is -3.3781 .

1.2 Sustained Harvesting

In this section, we consider a population evolving following a logistic growth. The population is subject to harvesting, for which we consider two types of models:

$$\dot{N} = \alpha N \left(1 - \frac{N}{K}\right) - EN \quad (1.2.1)$$

$$\dot{N} = \alpha N \left(1 - \frac{N}{K}\right) - Y_0, \quad (1.2.2)$$

where α and K are fixed, while E and Y_0 can vary. We refer to equation (1.2.1) as *constant effort* harvesting, while equation (1.2.2) is called *constant yield* harvesting. We say that there is a *sustained harvesting* if a stable fixed point with $N^* > 0$ exists. The *yield* is the fraction of harvested population per unit time, which is $Y = EN$ and $Y = Y_0$ for case (1.2.1) and (1.2.2) respectively.

We now show that for E and Y_0 sufficiently large, the above equations have no stable fixed point $N^* > 0$, i.e., there is no sustained harvesting. Moreover, we will show that for large E and Y_0 , there are no fixed points at all. This can be shown graphically, but perhaps it is even simpler (and also more exact) if we just solve for the fixed points.

To find the fixed points, we should look for solutions of $\dot{N} = 0$. These equations are

$$0 = -\frac{\alpha}{K}N^2 + (\alpha - E)N \quad (1.2.3)$$

$$0 = -\frac{\alpha}{K}N^2 + \alpha N - Y_0, \quad (1.2.4)$$

for the constant effort and constant yield case, respectively. These are quadratic equations, and hence both equations have at most two fixed points. Let us first look at the solutions of equation (1.2.3). The solutions are

$$N_1^* = 0, \quad N_2^* = \frac{K}{\alpha}(\alpha - E), \quad (1.2.5)$$

and it is clear that for $E \geq \alpha$, the above solutions are both negative, assuming α and K are positive numbers as in the previous problem. We also note that for $E = 0$, i.e. the ordinary logistic equation, these two solutions are the fixed points found the previous section. For the constant yield harvesting, the solutions to equation (1.2.4) are

$$N_{\pm}^* = \frac{K \left(\alpha \pm \sqrt{\alpha^2 - 4 \frac{\alpha Y_0}{K}} \right)}{2\alpha}. \quad (1.2.6)$$

From equation (1.2.6), we see that there are fixed points appearing if

$$\alpha^2 - 4 \frac{\alpha Y_0}{K} \geq 0, \quad (1.2.7)$$

which translates into the condition

$$Y_0 \leq \frac{\alpha K}{4} \quad (1.2.8)$$

for the yield parameter. If Y_0 is strictly larger than the right hand side of the above inequality, there are no fixed points. If $Y_0 = \frac{\alpha K}{4}$, then there is a single fixed point $N^* = K/2$. Again we note that for $Y_0 = 0$, i.e. the ordinary logistic equation, this gives us the two fixed points of the logistic equation.

Now we look at values for E and Y_0 low enough such that fixed points are present and determine the stability of these fixed points. Let us first look at the case of constant effort harvesting. As discussed above, strictly positive fixed points appear if $E < \alpha$, and the fixed points are given in equation (1.2.5). If we write (1.2.1) as $\dot{N} = f_e(N)$, then the stability of a fixed point N^* is determined by the sign of $f'_e(N^*)$. A short computation shows

$$f'_e(N) = \alpha - E - \frac{2\alpha}{K}N, \quad (1.2.9)$$

such that

$$f'_e(N_1^*) = \alpha - E > 0, \quad f'_e(N_2^*) = -(\alpha - E) < 0, \quad (1.2.10)$$

where we used that $E < \alpha$. Hence, N_1^* is an unstable fixed point, while N_2^* is a stable fixed point. This agrees with the results from the previous section, if we let E tend to zero.

Now consider the constant yield case. Denoting equation (1.2.2) as $\dot{N} = f_y(N)$, we find

$$f'_y(N) = \alpha - \frac{2\alpha}{K}N, \quad (1.2.11)$$

and evaluating at the fixed points given in equation (1.2.6), this gives

$$f'_y(N_{\pm}^*) = \mp \sqrt{\alpha^2 - 4 \frac{\alpha Y_0}{K}}. \quad (1.2.12)$$

For $Y_0 < \frac{\alpha K}{4}$, there is an unstable fixed point N_-^* and a stable fixed point N_+^* . If $Y_0 = \frac{\alpha K}{4}$, there is a single fixed point $N^* = K/2$, and $f'_y(K/2) = 0$. For this specific value of Y_0 , we can rewrite $f_y(N)$ as

$$f_y(N) = -\frac{\alpha}{K}N^2 + \alpha N - \frac{\alpha K}{4} = -\frac{\alpha}{K} \left(N - \frac{K}{2} \right)^2. \quad (1.2.13)$$

Hence $f_y(N) \leq 0$ for all values of N , which implies the flow is always to the left for this value of Y_0 . Hence the fixed point $N^* = K/2$ is a half-stable fixed point.

Now we consider the range of parameters in which a stable fixed point N^* is present in both cases, which is $E < \alpha$ and $Y_0 < \frac{\alpha K}{4}$. We wish to compare the yield of the two methods, denoted as Y_1 and Y_2 respectively, when evaluated at the positive stable fixed point, while keeping α and K constant. The yield for the second method is, of course, constant and satisfies $Y_2 = Y_0 < \frac{\alpha K}{4}$. The yield for the first case can be written as a function of the parameter E :

$$Y_1 \equiv Y_1(E) = EN^* = \frac{K}{\alpha}E(\alpha - E). \quad (1.2.14)$$

To find the maximum yield for this scenario, we differentiate the above function with respect to E and find its zero. This results in $E = \alpha/2$, which indeed satisfies $E < \alpha$, and gives the maximal yield

$$Y_{\max} \equiv \frac{\alpha K}{4}. \quad (1.2.15)$$

Moreover, for any value of Y_0 in the second scenario, we have $Y_2 < Y_1$.

Harvesting at a constant yield is in general not a good strategy. To justify this claim, we first note that the yield is smaller than the yield in the constant effort harvesting scenario. There is an additional drawback of the constant yield harvesting. We look at the right hand sides of the two differential equations (1.2.1) and (1.2.4), plotted both as a function of N in Figure 1.2.1 below. We take again $\alpha = 3$, $K = 10^3$, and also take E and Y_0 in the range such that there are two fixed points for each case, such as $E = 2$ and $Y_0 = 500$ in the plot below.

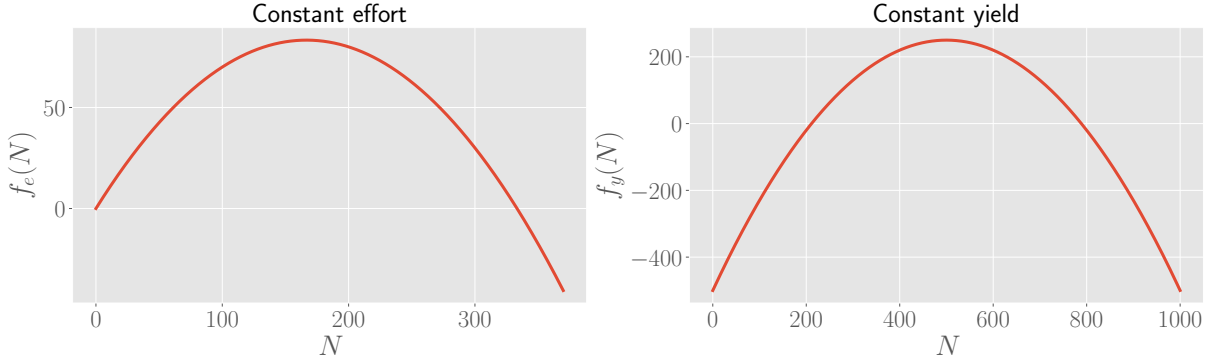


Figure 1.2.1: Right hand sides of the two differential equations (1.2.1) and (1.2.4) as functions of N , for $\alpha = 3$ and $K = 10^3$ fixed. *Left:* constant effort, with $E = 2$. *Right:* constant yield, with $Y_0 = 500$.

The problem with the constant yield method is the unstable fixed point N_-^* , which has a value of $N_-^* \approx 200$ in the figure above. If the initial population size N_0 lies below this fixed point, then the population will decrease in size until it goes extinct, and harvest is no longer possible. Since N_0 is likely unknown to us, the method of constant yield has the risk of letting the population go extinct if the value Y_0 is too high. The constant effort method is therefore preferred over the constant yield method. Indeed, as shown above, the unstable fixed point in this scenario is always located at $N = 0$, such that for any value of $E < \alpha$ and any N_0 , the population will tend to the stable fixed point after long time. Hence this method guarantees that the population will not go extinct and we can continue to do sustained harvesting, as long as $E < \alpha$.

1.3 Gompertz Law

According to the Gompertz model for population growth the individuals of a population follow the differential equation

$$\dot{N} = \alpha N \log\left(\frac{K}{N}\right). \quad (1.3.1)$$

Note that the fixed points of the Gompertz equation are $N^* = 0$ and $N^* = K$, which are identical to the fixed points of the logistic equation.

Consider the change of variable $y = \log N$. Then $\dot{y} = \frac{1}{N} \dot{N}$, and hence the above differential equation becomes

$$\dot{y} = \frac{1}{N} \dot{N} = \alpha (\log K - y). \quad (1.3.2)$$

This closely resembles the differential equation (1.1.2); the solution with initial condition $N(0) = N_0$ (and hence $y(0) = \log N_0$) is given by

$$y(t) = (\log N_0 - \log K) e^{-\alpha t} + \log K. \quad (1.3.3)$$

From this, we find that the solution to equation (1.3.1) with initial condition $N(0) = N_0$ is

$$N(t) = K \left(\frac{N_0}{K} \right)^{e^{-\alpha t}}. \quad (1.3.4)$$

In Figure 1.3.1 below, we plot the exact solutions to the logistic equation and the Gompertz equation for the parameters $\alpha = 3$, $K = 10^3$, and for initial conditions $N_0 = 10$, $N_0 = 10^5$, respectively. For the initial condition of the plot on the left hand side, the Gompertz law gives a greater rate of growth of the population, while for the initial condition of the plot on the right hand side, the converse is true. Moreover, for the plot on the left hand side, the curve for the Gompertz model converges quicker towards the stable fixed point compared to the logistic curve, while for the right hand side again the converse holds.

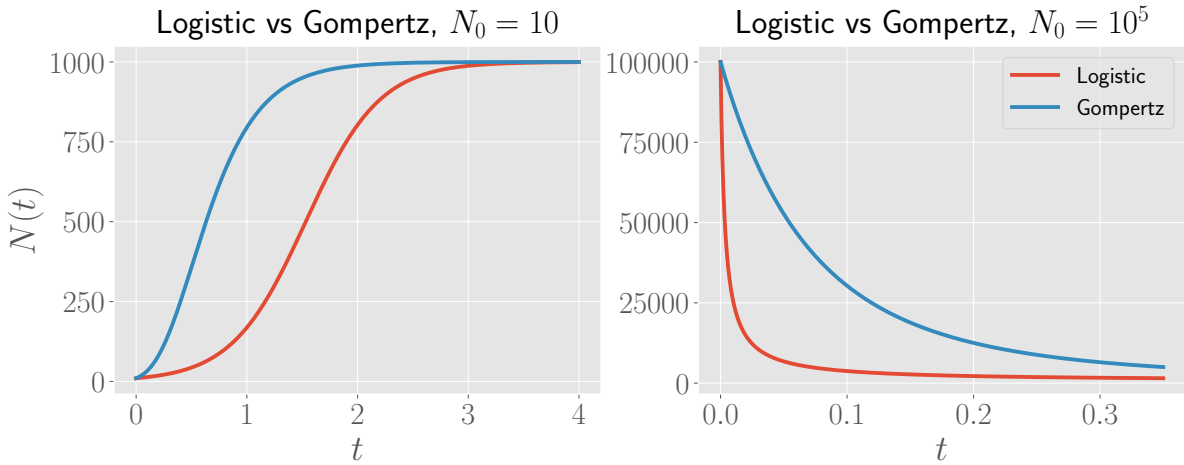


Figure 1.3.1: Exact solutions of the logistic and the Gompertz equation for $\alpha = 3$ and $K = 10^3$. *Left:* initial condition $N_0 = 10$. *Right:* initial condition $N_0 = 10^5$

To understand this behaviour, we need to compare the right hand sides of both differential equations as a function of N . These functions are shown in Figure 1.3.2. For small N , i.e. $N \ll K$, the right hand side is larger in absolute value for the Gompertz model, while for large N , i.e. $N \gg K$, it is larger in absolute value for the logistic model, which agrees with the observed behaviour of the solutions in Figure 1.3.1.

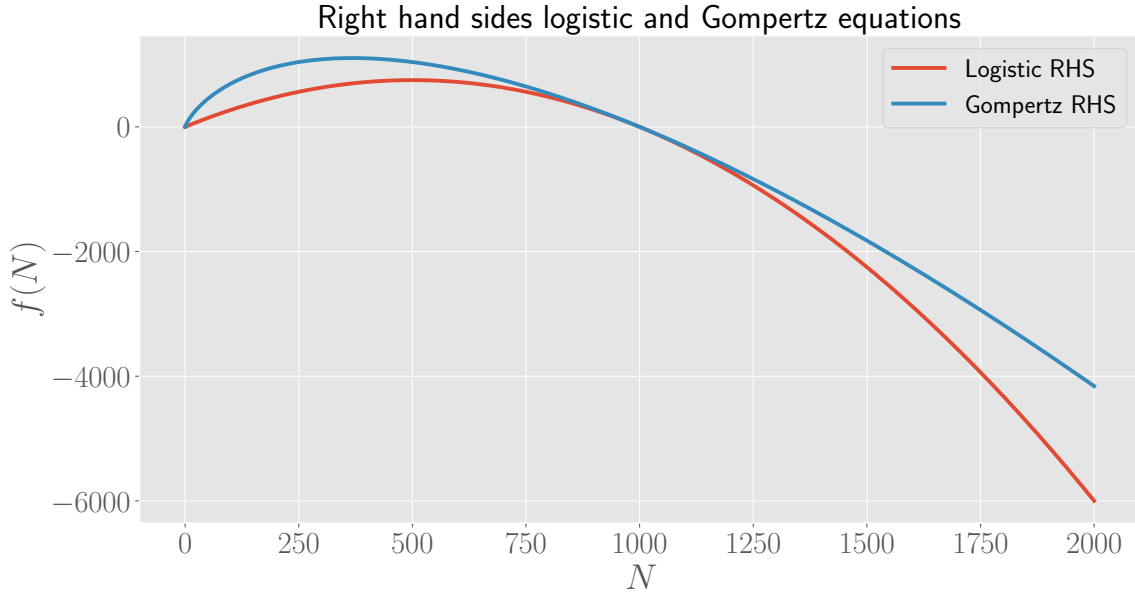


Figure 1.3.2: Right hand sides of the logistic and the Gompertz equation as functions of N , for $\alpha = 3$ and $K = 10^3$.

Note that both functions have a zero at $N = K$, as stated earlier. Moreover, we see from the figure above that the derivatives of both functions at this point are identical. Hence the two models have the same fixed point, and the same characteristic relaxation time to the stable fixed point. From this discussion and Figure 1.3.2, we can hence conclude that for $N \approx K$, the two models are almost identical to each other. However, far away from the fixed point, the two models clearly give different results, as shown in Figure 1.3.1.

1.4 Delays

In general, first order non-linear differential equations cannot have oscillating solutions. However, oscillating solutions are possible if the equation contains some delay. To justify this claim, we consider a delay in the logistic growth

$$\dot{N}(t) = \alpha N(t) \left(1 - \frac{N(t-T)}{K} \right), \quad (1.4.1)$$

where we fix $T = 3$, $\alpha = 1$ and $K = 10^3$.

We solve the above equation numerically with initial conditions $N(t) = 10$ for $t \leq 0$, and $N(t) = 10^5$, for $t \leq 0$. The two solutions are shown in Figure 1.4.1. For the first initial condition, oscillations already appear around $t \approx 10$, while for the second initial condition, the oscillations appear much later, around $t \approx 300$.

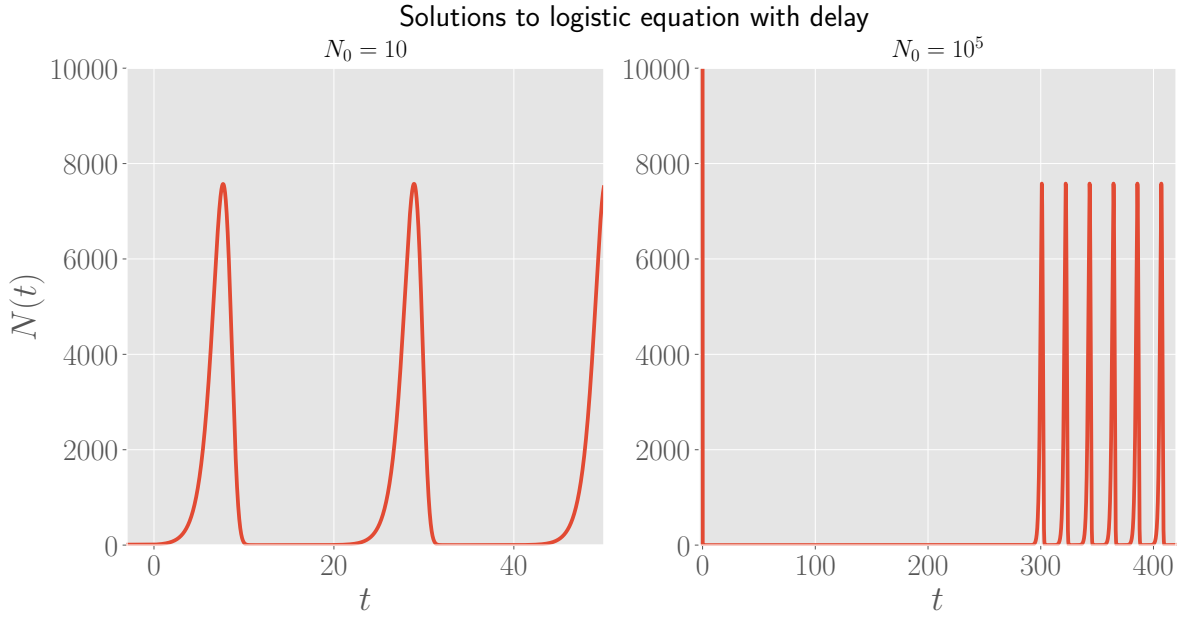


Figure 1.4.1: Solutions to the logistic equation with a delay, equation (1.4.1), with $T = 3$, $\alpha = 3$ and $K = 10^3$. *Left:* $N_0 = 10$. *Right:* $N_0 = 10^5$.

At long times, both the solutions are identical, except for possibly a phase shift. Indeed, once the oscillations are present for both of the solutions, they are identical to each other, up to a translation on the time axis. This is verified by plotting both solutions in the same figure, and restricting the range in time to an interval in which both solutions are oscillating, as shown in Figure 1.4.2.

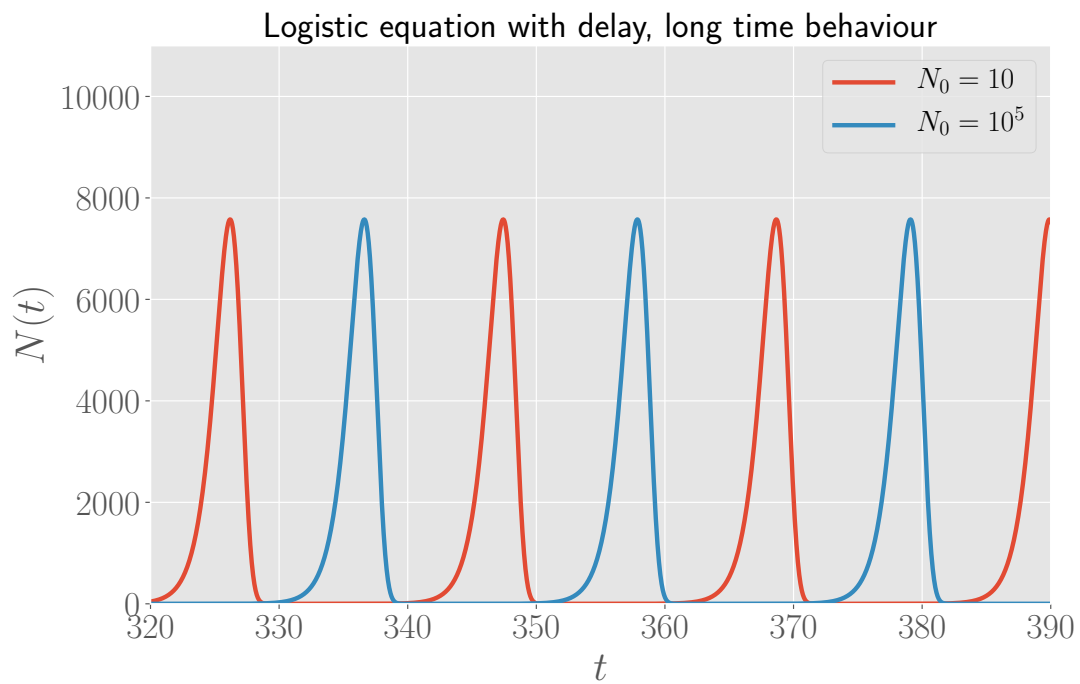


Figure 1.4.2: Long time behaviour of the two solutions shown in Figure 1.4.1, for $320 \leq t \leq 390$.

2 Concepts of non-linear dynamics

2.1 Rabbit versus sheep

We consider the following model for two competing populations, which belongs to the class of Lotka-Volterra models:

$$\begin{cases} \dot{N} = N(3 - N - 2M) \\ \dot{M} = M(2 - N - M) \end{cases}. \quad (2.1.1)$$

The two populations follow a logistic growth, but compete for common resources. This interaction is indicated by the negative non-linear cross terms. The system has four fixed points, which are solutions to the equations

$$\begin{cases} N(3 - N - 2M) = 0 \\ M(2 - N - M) = 0 \end{cases}. \quad (2.1.2)$$

The first obvious solution is $(N, M) = (0, 0)$. Other solutions are found by letting $N = 0$ but $M \neq 0$ and vice versa. These result in the solutions $(N, M) = (0, 2)$ and $(N, M) = (3, 0)$. If $N \neq 0$ and $M \neq 0$, there is one more solution. Indeed, then the system of equations (2.1.2) becomes

$$\begin{cases} 3 - N - 2M = 0 \\ 2 - N - M = 0. \end{cases} \quad (2.1.3)$$

The second equation gives $M = -N + 2$, substituting this in the first equation then gives $N = 1$ such that $M = 1$. Hence $(N, M) = (1, 1)$ is another fixed point of the system of equations.

We now determine the nature of these fixed points. For this, we will need the Jacobian matrix associated to the system of equations (2.1.1). If we write $\dot{N} = f(N, M)$ and $\dot{M} = g(N, M)$, then the Jacobian matrix is

$$J(N, M) = \begin{pmatrix} \partial_N f & \partial_M f \\ \partial_N g & \partial_M g \end{pmatrix} = \begin{pmatrix} 3 - 2N - 2M & -2N \\ -M & 2 - N - 2M \end{pmatrix}. \quad (2.1.4)$$

The nature of the fixed point is determined by the trace and determinant of the Jacobian, evaluated at the fixed point. Below, we will often compute the discriminant

$$\Delta = \text{tr}^2 A - 4 \det A. \quad (2.1.5)$$

Let us first investigate the fixed point $(N, M) = (0, 0)$. The Jacobian evaluated at this fixed point gives

$$J(0, 0) = \begin{pmatrix} 3 & 0 \\ 0 & 2 \end{pmatrix}. \quad (2.1.6)$$

We can directly see the two eigenvalues of the matrix are $\lambda_1 = 3$ and $\lambda_2 = 2$. Hence this fixed point is an unstable node. For the second fixed point, $(N, M) = (0, 2)$ we have

$$J(0, 2) = \begin{pmatrix} -1 & 0 \\ -2 & -2 \end{pmatrix}. \quad (2.1.7)$$

Since the matrix is triangular, we can see that its eigenvalues are $\lambda_1 = -1$ and $\lambda_2 = -2$. Hence both eigendirections are stable, and this fixed point is a stable node. For the third fixed point, $(N, M) = (0, 3)$, we have

$$J(3, 0) = \begin{pmatrix} -3 & -6 \\ 0 & -1 \end{pmatrix}. \quad (2.1.8)$$

As before, we can directly read off the eigenvalues since the matrix is triangular. We find $\lambda_1 = -3$ and $\lambda_2 = -1$, such that both eigendirections are stable, and this fixed point is also a stable node. Finally, for the fourth fixed point, $(N, M) = (1, 1)$, we have

$$J(1, 1) = \begin{pmatrix} -1 & -2 \\ -1 & -1 \end{pmatrix}. \quad (2.1.9)$$

For this matrix we find $\det J(1, 1) = -1$, such that the fourth fixed point is a saddle node. A short calculation shows that the eigenvalues are $\lambda_{\pm} = -1 \pm \sqrt{2}$, such that indeed one eigenvalue is positive, while the other eigenvalue is negative. The eigenvectors corresponding to these eigenvalues are $\mathbf{v}_- = (\sqrt{2}, -1)$ and $\mathbf{v}_+ = (\sqrt{2}, 1)$.

The full phase portrait is given below in Figure 2.1.1 below, from which we can deduce some general features. The two fixed points on the axes attract solutions from all directions, while the fixed point $(1, 1)$ attracts solutions from one direction, but repels solutions from another direction. When close to the origin, solutions get repelled away from the origin.

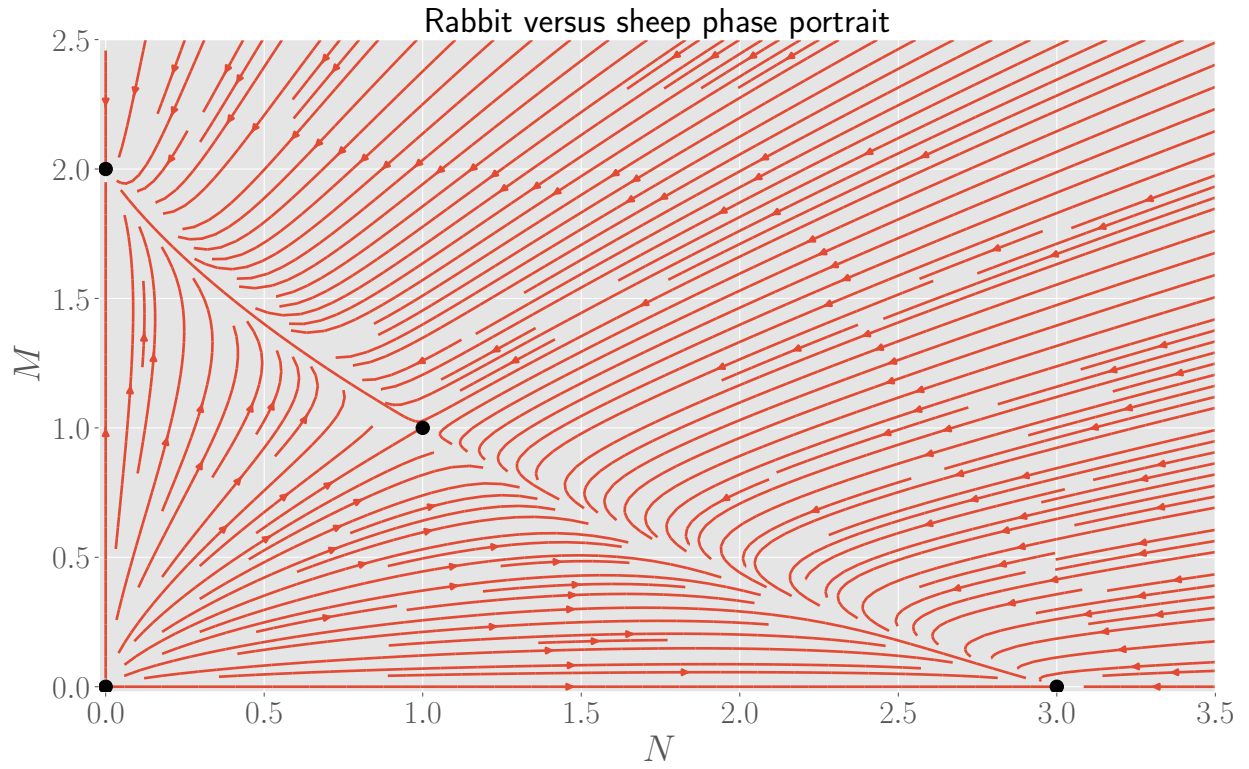


Figure 2.1.1: Phase portrait of the system of equations in (2.1.1). The black dots indicate the fixed points.

We can also verify the eigendirections of the saddle node. A close-up of the saddle node $(N, M) = (1, 1)$ is given in Figure 2.1.2 below. The phase portrait close to this saddle node agrees with our expectations based on the earlier analytic computations.

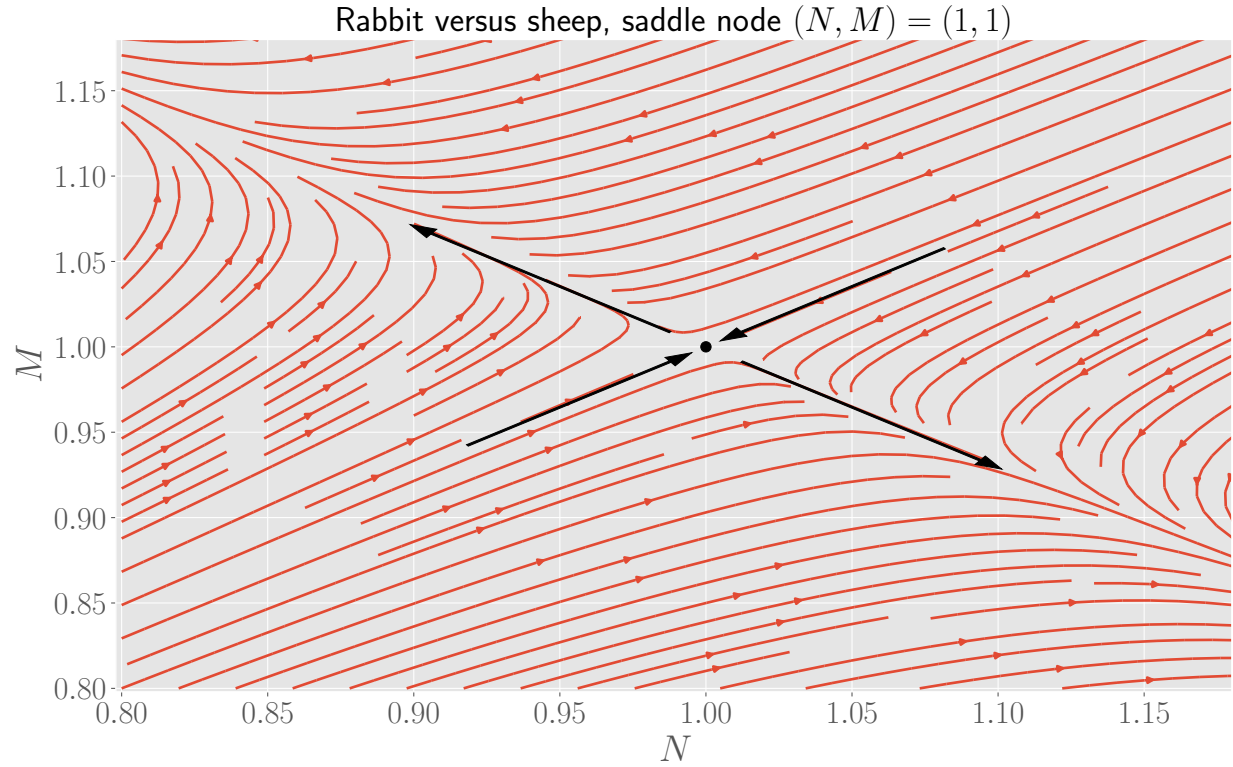


Figure 2.1.2: Close-up of the saddle node $(N, M) = (1, 1)$, the black dot in the plot. The two arrows denote the eigenvectors of the Jacobian matrix $J(1, 1)$, the direction of the arrow denoting attraction or repulsion.

We can also conclude from Figure 2.1.1 that the two populations can not coexist with each other. Indeed, for almost all initial conditions, the phase portrait shows that the solutions tend towards either the fixed point $(N, M) = (2, 0)$ or the fixed point $(N, M) = (0, 3)$. In both cases, this means that one of the species goes extinct. There is an exception to this scenario, namely for initial conditions which lie on the straight line through the fixed point $(N, M) = (1, 1)$ and with slope $1/\sqrt{2}$, i.e. along the attractive eigendirection of that fixed point. Indeed, Figure 2.1.2 shows that in that case, the solution is attracted towards $(N, M) = (1, 1)$, and the two populations can live together. Of course, if the initial condition is located precisely at the fixed point $(1, 1)$, the two species can also coexist with each other. However, the set of points on which coexistence is possible has measure zero, such that this is in fact an exotic scenario. For a generic initial condition, one of the populations tends towards extinction.

2.2 Classification of linear systems

We discuss the nature of the fixed point $(x, y) = (0, 0)$ for a few systems of linear differential equations. The first system is

$$\begin{cases} \dot{x} = y \\ \dot{y} = -2x - 3y \end{cases}. \quad (2.2.1)$$

To determine the nature of the fixed point $(x, y) = (0, 0)$, we compute the Jacobian, and evaluate it at the fixed point. However, since the differential equations are linear, the Jacobian is constant:

$$J_1(x, y) = J_1 = \begin{pmatrix} 0 & 1 \\ -2 & -3 \end{pmatrix}. \quad (2.2.2)$$

We have $\text{tr } J_1 = -3$, $\det J_1 = 2$ and hence $\Delta = 1 > 0$, where Δ was defined in equation (2.1.5). Therefore, this is a stable node. The eigenvalues and -vectors of this matrix are

$$\lambda_1 = -1, \lambda_2 = -2, \quad \mathbf{v}_1 = \begin{pmatrix} -1/2 \\ 1 \end{pmatrix}, \mathbf{v}_2 = \begin{pmatrix} -1 \\ 1 \end{pmatrix} \quad (2.2.3)$$

The phase portrait, as well as the eigendirections found above, are shown in Figure 2.2.1 below.

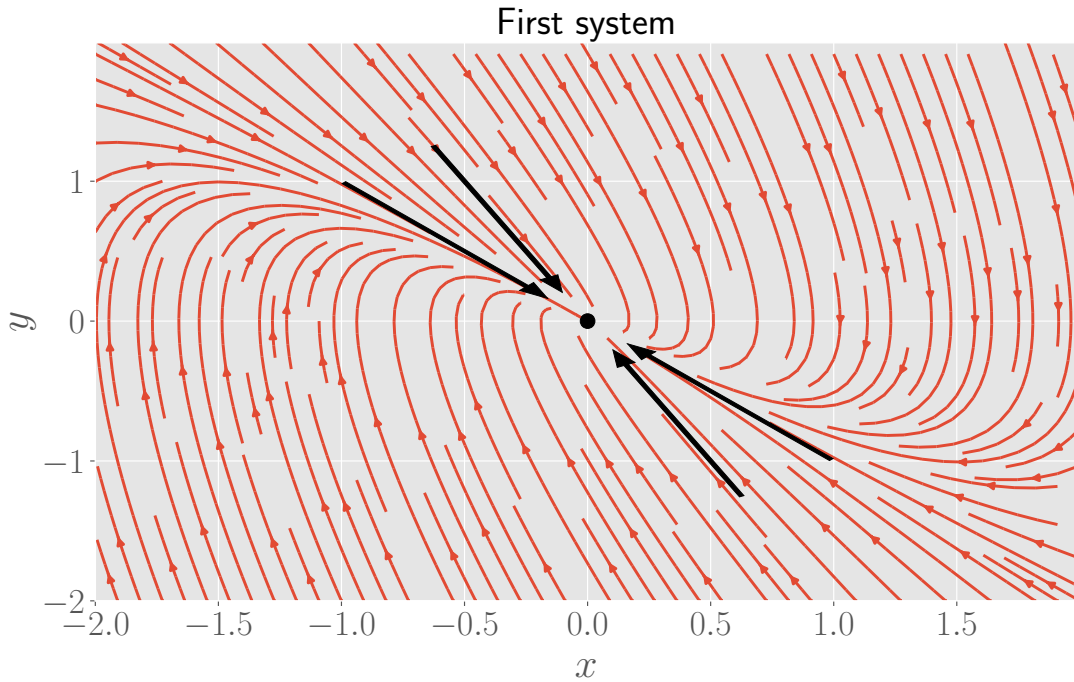


Figure 2.2.1: Phase portrait and eigendirections of the origin as fixed point for the first system. The direction of the arrows denotes attraction towards the origin.

The second system of equations is

$$\begin{cases} \dot{x} = -3x + 4y \\ \dot{y} = -x + y \end{cases}. \quad (2.2.4)$$

Again, the Jacobian is constant, and given by

$$J_2 = \begin{pmatrix} -3 & 4 \\ -1 & 1 \end{pmatrix}, \quad (2.2.5)$$

such that $\text{tr } J_2 = -2$ and $\det J_2 = 1$ and hence $\Delta = 0$. Hence this is a limiting case, for which the linear stability analysis is inconclusive. A short calculation shows that this matrix has a degenerate eigenvalue

$$\lambda = -1, \quad \mathbf{v} = \begin{pmatrix} 2 \\ 1 \end{pmatrix}. \quad (2.2.6)$$

The phase portrait, as well as the eigendirection found above, are shown in Figure 2.2.2 below.

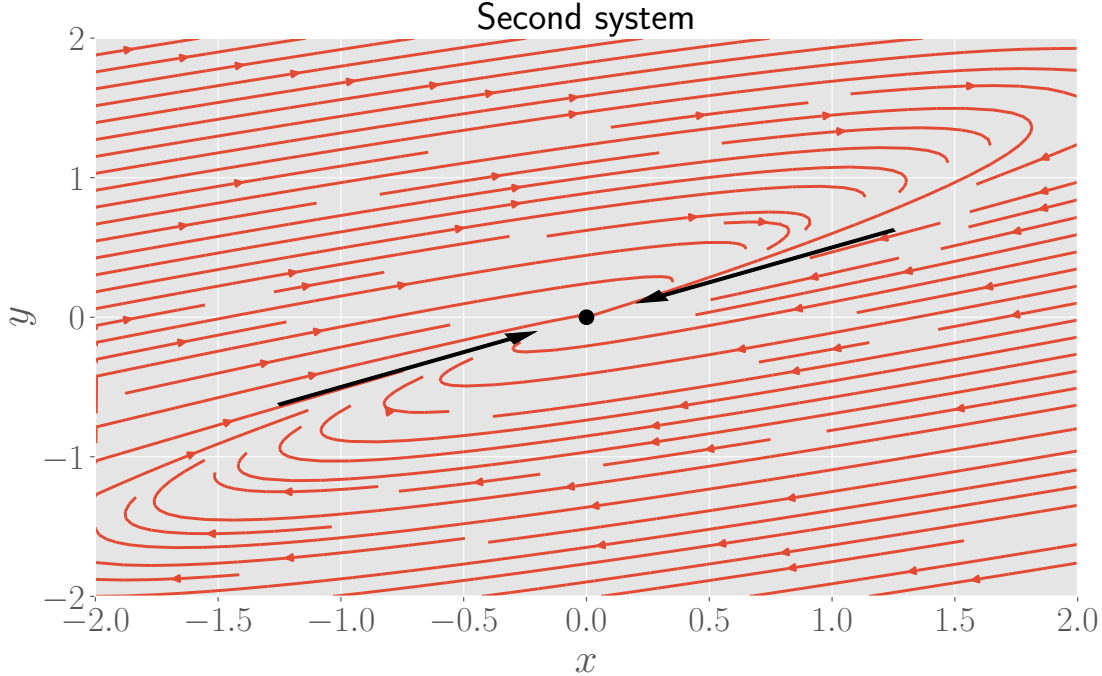


Figure 2.2.2: Phase portrait and eigendirection of the origin as fixed point for the second system. The direction of the arrows denotes attraction towards the origin.

The third system of equations is

$$\begin{cases} \dot{x} = -3x + 4y \\ \dot{y} = -2x + 3y \end{cases}. \quad (2.2.7)$$

Again, the Jacobian is constant, and given by

$$J_3 = \begin{pmatrix} -3 & 4 \\ -2 & 3 \end{pmatrix}, \quad (2.2.8)$$

such that we have $\text{tr } J_3 = 0$ and $\det J_3 = -1$. Since $\det J_3 < 0$, the origin is guaranteed to be a saddle node. A short calculation shows that the eigenvalues and -vectors of this matrix are

$$\lambda_+ = 1, \lambda_- = -1, \quad \mathbf{v}_+ = \begin{pmatrix} 1 \\ 1 \end{pmatrix}, \quad \mathbf{v}_- = \begin{pmatrix} 2 \\ 1 \end{pmatrix}. \quad (2.2.9)$$

The phase portrait, as well as the eigendirections found above, are shown in Figure 2.2.3 below.

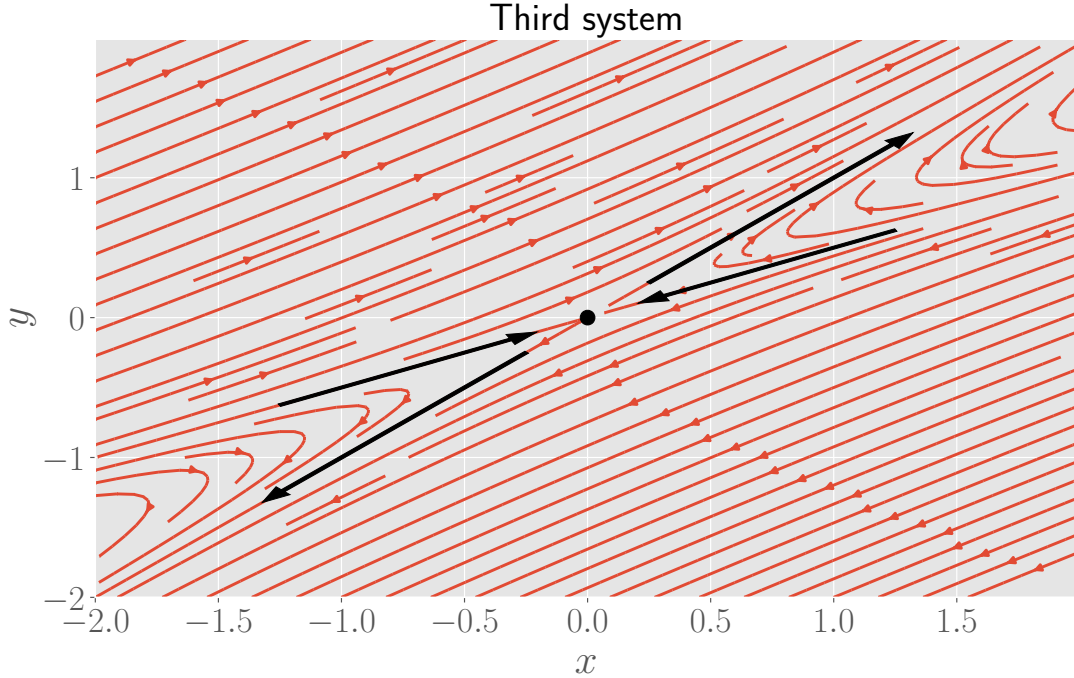


Figure 2.2.3: Phase portrait and eigendirections of the origin as fixed point for the third system. The direction of the arrows denotes attraction towards or repulsion away from the origin.

2.3 Phase portrait in two dimensions

Consider the following system of differential equations

$$\begin{cases} \dot{x} = x - y \\ \dot{y} = 1 - e^x \end{cases}. \quad (2.3.1)$$

We are interested in the nullclines, which are the curves in the plane for which $\dot{x} = 0$ or $\dot{y} = 0$. The equation $\dot{x} = 0$ gives $y = x$ and hence this nullcline is a straight line with slope one. The second equation, $\dot{y} = 0$, gives $e^x = 1$, so the solution to this equation is $x = 0$, which is the y -axis. The fixed points are the intersections between these two nullclines, and hence the origin is a fixed point for our system of equations. The nullclines divide the (x, y) -plane into regions with different signs for \dot{x} and \dot{y} . These regions are shown in Figure 2.3.1 below. We have

- Region I: $\dot{x} > 0$ and $\dot{y} < 0$,
- Region II: $\dot{x} < 0$ and $\dot{y} < 0$,
- Region III: $\dot{x} < 0$ and $\dot{y} > 0$,
- Region IV: $\dot{x} > 0$ and $\dot{y} > 0$.

In Figure 2.3.1, we also show the expected behaviour of the phase portrait. That is, we sketch the behaviour of a few solutions (increasing or decreasing in x , increasing or decreasing in y) for a few initial conditions in the four different regions. We also made use of the fact that whenever a solution crosses a nullcline, the line tangent to the curve at that point is parallel to the x - or y -axis.

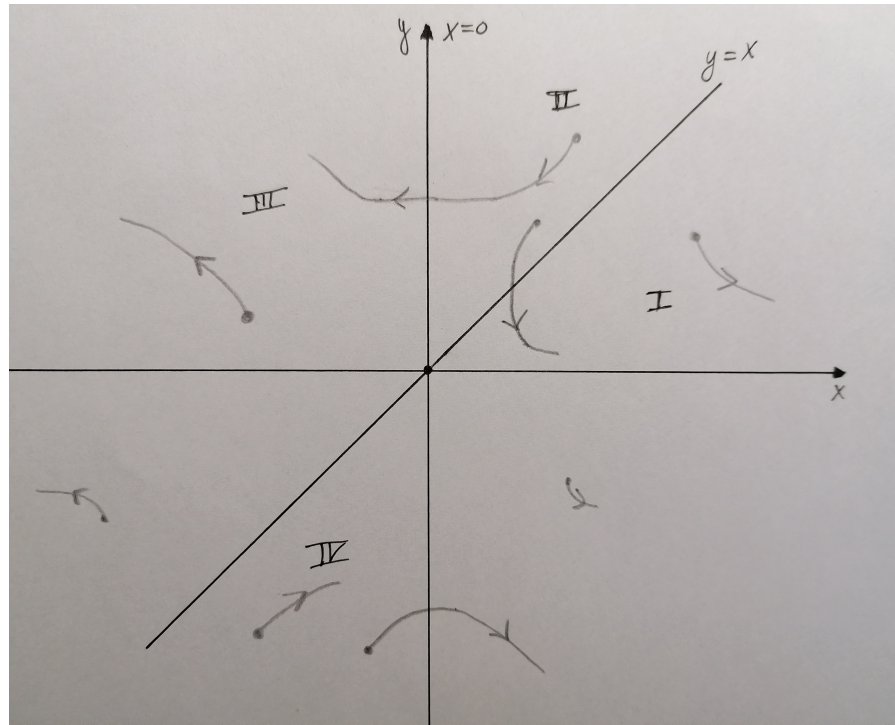


Figure 2.3.1: Sketch of the phase portrait of the system of equations (2.3.1) and the four different regions.

We now verify these findings by plotting the solutions to the system of equations obtained via a numerical computation, for the initial conditions $(1, 2)$, $(1, 1.5)$, $(-1, -2)$ and $(-1, -1.2)$. This is shown in Figure 2.3.2 below, where we also plot the phase portrait. Comparing with our sketch, we see that the solutions indeed agree with the expected behaviour, based on the signs of \dot{x} and \dot{y} in the four regions partitioned by the nullclines. We can also check that when the solutions cross the nullclines, they are parallel to the x - or y -axis.

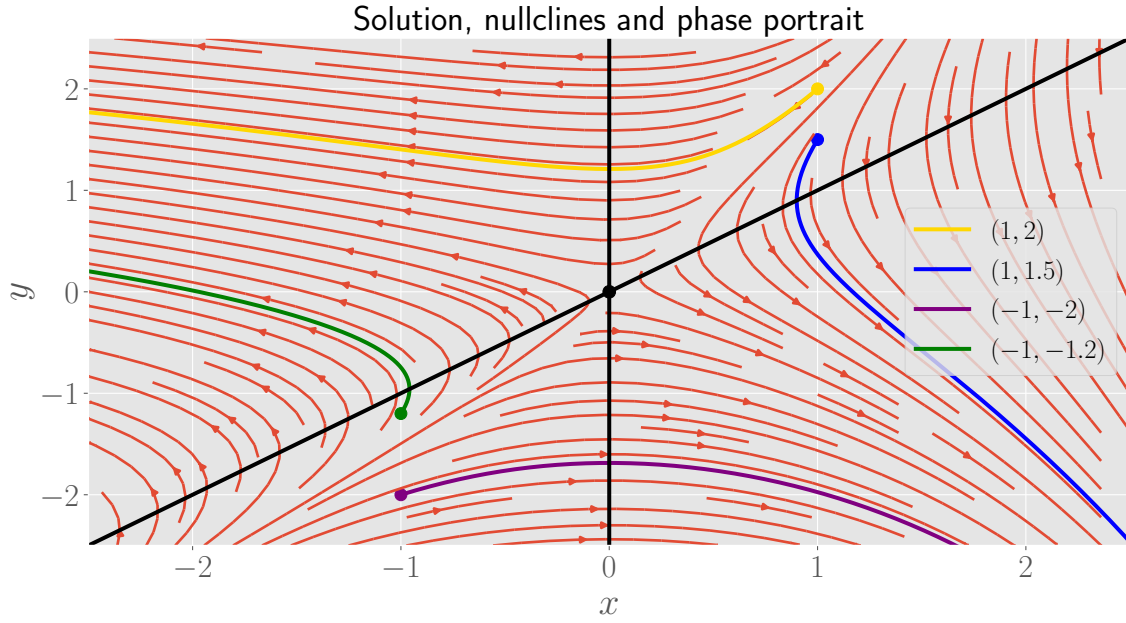


Figure 2.3.2: Solutions to the system of equations (2.3.2), with initial conditions given in the legend and the phase portrait. The black lines denote the two nullclines and their intersection, the origin, is the fixed point.

3 Quasi steady state approximation

3.1 Linear example of quasi steady-state approximation

When dealing with N coupled first-order differential equations, one can use the so-called *quasi-steady-state approximation* (QSSA). This approximation can be applied if one variable evolves much faster than the others. Let us suppose that $x_1(t)$ is this 'fast' variable. We then take $\dot{x}_1 = 0$, from which one obtains $x_1(t)$ as a function of the other $N - 1$ variables. The procedure is known in mathematics as singular perturbation theory.

As an example of this method, we consider the following system of linear differential equations

$$\begin{cases} \dot{x} = -3x + y \\ \dot{y} = 100(2x - y) \end{cases}, \quad (3.1.1)$$

with initial conditions $x(0) = 1$ and $y(0) = 0$. The fast variable can be identified by looking at a plot of the solutions, obtained via numerically solving the above set of differential equations as in the previous assignment. Figure 3.1.1 below shows the solutions for the given initial conditions. It is clear that y is the fast changing variable in this scenario.

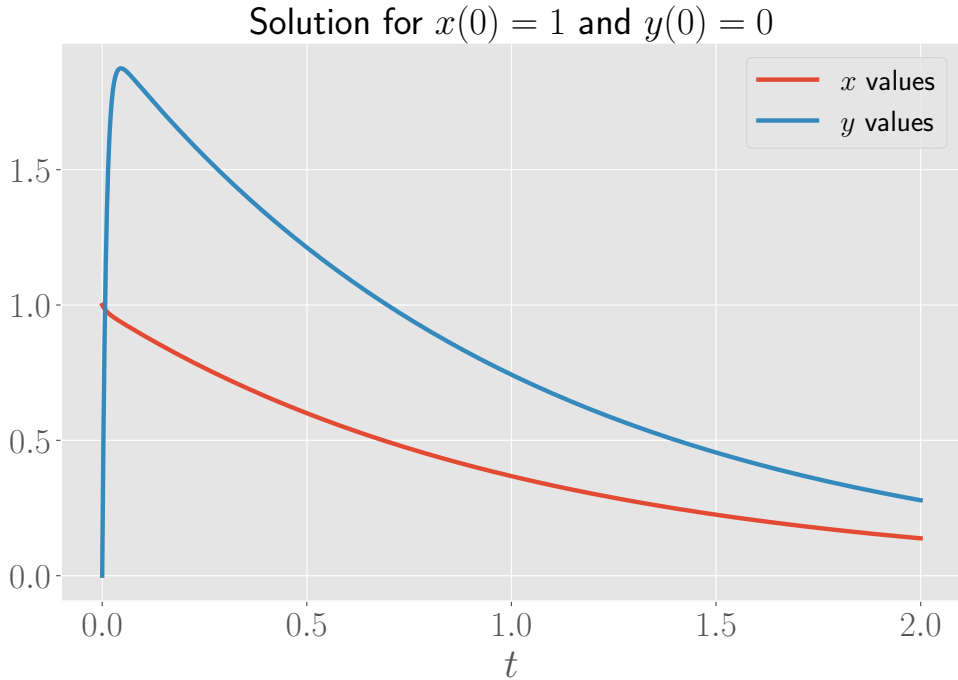


Figure 3.1.1: Solution to the set of differential equations (3.1.1) for initial conditions $x(0) = 1$ and $y(0) = 0$. From this, we can identify y as the fast variable.

As a brief side remark, we note that we can rewrite the system of differential equations in a matrix form

$$\dot{\Omega}(t) = M\Omega(t), \quad \Omega(t) = \begin{pmatrix} x(t) \\ y(t) \end{pmatrix}, \quad (3.1.2)$$

where M is a 2×2 matrix. Using this notation, the system can be solved exactly, and the solution can be expressed in terms of the eigenvectors and eigenvalues of M . We will give the general outline of this method. By diagonalising the matrix M , we find an invertible matrix P (of which the columns are the eigenvectors of M) and a diagonal matrix D containing the corresponding eigenvalues λ_1 and λ_2 , such that $M = PDP^{-1}$. Substituting this into the above differential equation and multiplying both sides of the equation to the left by P^{-1} , this becomes

$$P^{-1}\dot{\Omega} = DP^{-1}\Omega, \quad (3.1.3)$$

and if we define variables u and v as linear combinations of x and y , via

$$\begin{pmatrix} u \\ v \end{pmatrix} = P^{-1}\Omega, \quad (3.1.4)$$

then the set of differential equations is transformed into the following differential equations

$$\begin{cases} \dot{u} &= \lambda_1 u \\ \dot{v} &= \lambda_2 v \end{cases}, \quad (3.1.5)$$

of which the solutions are exponentials in time. The solutions for x and y are then found by multiplying by P . For our case, the matrix M is

$$M = \begin{pmatrix} -3 & 1 \\ 200 & -100 \end{pmatrix}, \quad (3.1.6)$$

and its eigenvalues and eigenvectors can easily be computed numerically (as done for example [here](#)), and we find

$$P = \begin{pmatrix} \frac{\sqrt{10209}+97}{400} & \frac{-\sqrt{10209}+97}{400} \\ 1 & 1 \end{pmatrix}, \quad D = \begin{pmatrix} \frac{-103+\sqrt{10209}}{2} & 0 \\ 0 & \frac{-103-\sqrt{10209}}{2} \end{pmatrix} \quad (3.1.7)$$

$$P^{-1} = \begin{pmatrix} \frac{-200}{\sqrt{10209}} & \frac{1}{2} + \frac{97}{2\sqrt{10209}} \\ \frac{200}{\sqrt{10209}} & \frac{1}{2} - \frac{97}{2\sqrt{10209}} \end{pmatrix}. \quad (3.1.8)$$

Following the general outline given above gives us the exact solutions for x and y . However, the details will not be provided here, since this is a tedious exercise and the expressions become quite cumbersome. Moreover, the numerical solutions to the differential equations are sufficient for us to capture the idea of the QSSA.

We now apply the QSSA to our set of differential equations, by setting $\dot{y} = 0$. This allows us to express $y(t)$ in function of $x(t)$. From equation (3.1.1), we see that in the QSSA we

have $y = 2x$. We will compare the QSSA to the numerical solutions, by reproducing Figure 3.1.1 and also plotting the curve $y_{\text{QSSA}}(t) = 2x(t)$. The result is shown in Figure 3.1.2 below, with the QSSA shown as a grey dashed line.

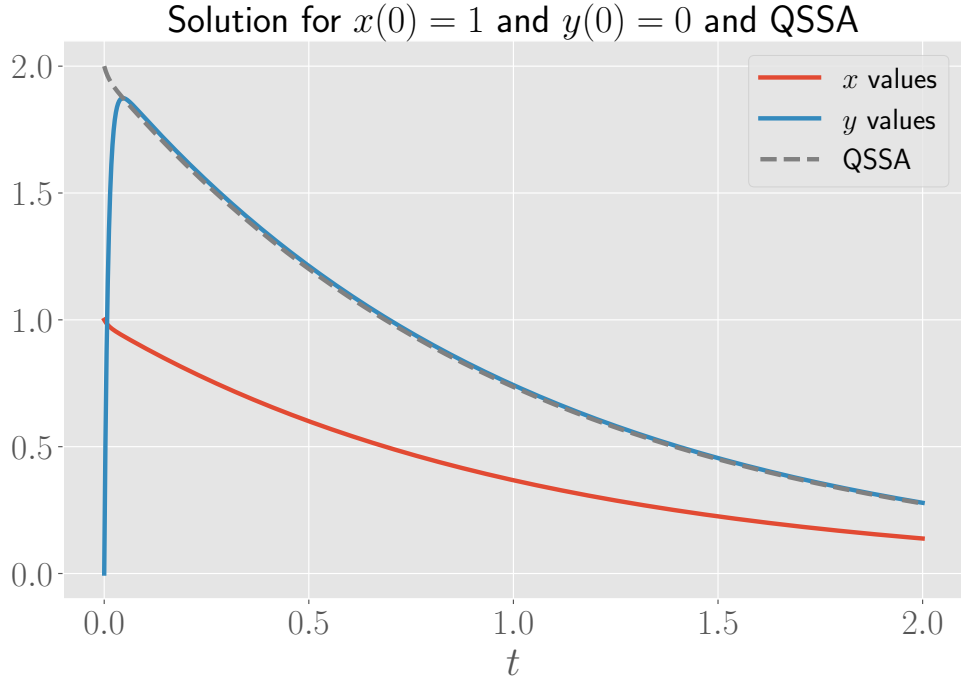


Figure 3.1.2: Solution to the system of differential equations (3.1.1) for initial conditions $x(0) = 1$ and $y(0) = 0$, along with the curve showing the QSSA $y = 2x$.

We see that approximation is very close to the exact (i.e., without the QSSA) solution for almost all values of t . However, for small t , the fast variable is varying much, and this variation is not captured by the approximation. Hence we can conclude that while the QSSA is a good approximation if one wants to deduce the long time behaviour of ‘fast variables’, it does not provide an accurate description of the solutions for times close to zero.

3.2 Enzymatic degradation

In many situations a chemical X is degraded, meaning that it breaks into fragments which do not participate to the reactions anymore. Spontaneous degradation of X , i.e. a reaction $X \rightarrow \emptyset$, is described in the mass action kinetics by a term $-\alpha x$, where x is the concentration of X , and α the degradation rate. Synthesis and degradation of a chemical are described by the equation

$$\frac{dx}{dt} = \beta - \alpha x, \quad (3.2.1)$$

where β is the creation rate, which can eventually depend on other chemical concentrations.

We consider here a different type of degradation due to the effect of an enzyme E on X. The enzymatic degradation is described by the following reactions



which describe the binding of X to the enzyme E and formation of a complex EX, through a reversible reaction, followed by the irreversible degradation of X. Once degradation has occurred, the free enzyme is released.

We will first write down the system of differential equations corresponding to the above scenario. For this, we write the chemical reactions in equation (3.2.2) in separate chemical reactions.



To find the differential equations governing these chemical reactions, we use mass action kinetics. Define

$$x \equiv [X] , \quad e \equiv [E] , \quad c \equiv [EX] . \quad (3.2.6)$$

Then we find

$$\begin{cases} \dot{e} &= -k_1ex + (k_{-1} + k')c \\ \dot{x} &= -k_1ex + k_{-1}c \\ \dot{c} &= k_1ex - (k_{-1} + k')c \end{cases} . \quad (3.2.7)$$

As expected, not all these differential equations are independent. Indeed, since X is the only chemical which exhibits degradation, the sum of the concentrations of E and EX should be constant. This is verified by looking at equation (3.2.7), which shows that

$$\frac{d(e + c)}{dt} = 0 . \quad (3.2.8)$$

Therefore, we can write $e + c = e_0 \equiv e(0)$ (we assume that at $t = 0$, there are no complex chemicals formed yet) and eliminate e from the above equations. This gives the equivalent set of differential equations

$$\begin{cases} \dot{x} &= -k_1e_0x + (k_1x + k_{-1})c \\ \dot{c} &= k_1e_0x - (k_1x + k_{-1} + k')c \\ e + c &= e_0 \end{cases} . \quad (3.2.9)$$

We will now apply the QSSA, assuming that the complex is rapidly formed and hence c is the fast variable. Therefore, we are allowed to put $\dot{c} = 0$. Then we find that

$$c = \frac{k_1 e_0 x}{k_1 x + k_{-1} + k'} = \frac{e_0 x}{x + K_m}, \quad K_m \equiv \frac{k_{-1} + k'}{k_1}, \quad (3.2.10)$$

where K_m is the so-called Michaelis-Menten constant. Substituting this result for c back into the equation of \dot{x} , and doing some straightforward algebraic manipulations, we find

$$\frac{dx}{dt} = \frac{-k' e_0 x}{x + K_m}. \quad (3.2.11)$$

We see that in this approximation, the equation for \dot{x} contains a degradation term which is different from the degradation term in equation (3.2.1), and can be called *enzymatic degradation*. In Figure 3.2.1 below, we make a plot of this enzymatic degradation curve. As is already clear from the equation in (3.2.11), this curve has saturation and becomes approximately constant for large x . The concentration of the complex has the same feature and also has a plateau for large x , as seen from equation (3.2.10). The explanation is that for a large concentration of substrate particles X , all enzymes are bound to the substrate chemicals X . Since the reaction needs an enzyme to occur, there are no additional reactions occurring unless an enzyme becomes free again and available to link with another substrate chemical. Hence the formation of complexes does not speed up beyond this point.

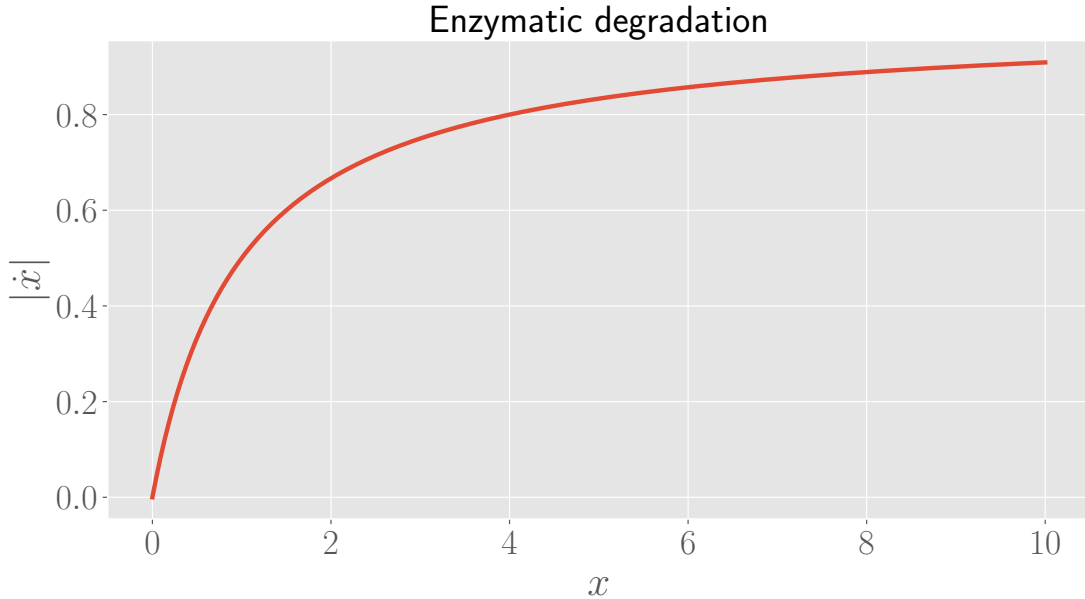


Figure 3.2.1: Plot of the absolute value of the enzymatic degradation curve, defined in equation (3.2.11), with all parameters set to 1.

3.3 Two subunit enzyme

We consider an enzyme which is formed by two subunits and which we denote as EE. Each subunit is capable of transforming a substrate S into a product P. The reactions are



As before, we will use mass action kinetics to find the relevant differential equations. Define $s \equiv [S]$, $e \equiv [E]$, $c_1 \equiv [EES]$, $c_2 \equiv [SEES]$ and $p = [P]$. The system of equations governing the reactions is

$$\begin{cases} \dot{s} &= -k_1 es + k_{-1} c_1 + k_{-2} c_2 - k_2 c_1 s \\ \dot{e} &= -k_1 es + (k_{-1} + k_3) c_1 \\ \dot{c}_1 &= k_1 es - (k_{-1} + k_3) c_1 - k_2 c_1 s + (k_{-2} + k_4) c_2 \\ \dot{c}_2 &= k_2 c_1 s - (k_{-2} + k_4) c_2 \\ \dot{p} &= k_3 c_1 + k_4 c_2 \end{cases}. \quad (3.3.5)$$

As before, we have a conservation equation

$$\frac{d(e + c_1 + c_2)}{dt} = 0, \quad (3.3.6)$$

from which we find that $e + c_1 + c_2 \equiv e_0$ is constant. Again, we assume no complex chemicals are formed at $t = 0$. We now apply the QSSA for c_1 and c_2 , and hence set $\dot{c}_1 = 0 = \dot{c}_2$. This gives

$$\begin{cases} 0 &= k_1 es - (k_{-1} + k_3) c_1 - k_2 c_1 s + (k_{-2} + k_4) c_2 \\ 0 &= k_2 c_1 s - (k_{-2} + k_4) c_2. \end{cases} \quad (3.3.7)$$

Define

$$K_{m1} = \frac{k_{-1} + k_3}{k_1}, \quad K_{m2} = \frac{k_{-2} + k_4}{k_2}. \quad (3.3.8)$$

The second condition, $\dot{c}_2 = 0$, can be written as

$$c_2 = \frac{s}{K_{m2}} c_1, \quad (3.3.9)$$

Subsituting this in the equation $\dot{c}_1 = 0$ gives

$$k_1 es = k_1 K_{m1} c_1 - k_2 c_1 s + (k_{-2} + k_4) \frac{s}{K_{m2}} c_1, \quad (3.3.10)$$

and using the definitions of K_{m1} and K_{m2} , this can be further simplified. The outcome is

$$c_1 = \frac{es}{K_{m1}}, \quad c_2 = \frac{es^2}{K_{m1}K_{m2}}. \quad (3.3.11)$$

Now we are able to derive the rate of production of the P particles. We will divide the equation for \dot{p} by $e_0 = e + c_1 + c_2$, and get

$$\frac{1}{e_0} \frac{dp}{dt} = \frac{k_3 c_1 + k_4 c_2}{e + c_1 + c_2} \quad (3.3.12)$$

$$= \frac{k_3 \frac{es}{K_{m1}} + \frac{k_4 es^2}{K_{m1}K_{m2}}}{e + \frac{es}{K_{m1}} + \frac{es^2}{K_{m1}K_{m2}}}, \quad (3.3.13)$$

where we used the expressions for c_1 and c_2 found above. We see that the dependence on e cancels in the right hand side. We can further simplify the right hand side, and we end up with

$$\frac{dp}{dt} = \frac{k_3 K_{m2} e_0 s + k_4 e_0 s^2}{K_{m1} K_{m2} + K_{m2} s + s^2}. \quad (3.3.14)$$

Now we consider the limit $K_{m1} \rightarrow +\infty$, $K_{m2} \rightarrow 0$ such that $K_{m1} K_{m2} \rightarrow K = \text{cte}$. Inserting these limits in the above equation, this gives

$$\frac{dp}{dt} \rightarrow \frac{k_4 e_0 s^2}{K + s^2}. \quad (3.3.15)$$

Hence in this limit, the kinetics has the form of Hill kinetics, with the Hill exponent equal to 2.

Up until now, we considered arbitrary values for the rates k_i . Now, we consider the rates to be given by

$$k_1 = 2k_2, \quad k_{-2} = 2k_{-1} \quad k_4 = 2k_3. \quad (3.3.16)$$

This corresponds to the situation where the two subunits of the enzyme work independently from each other. For example, the equality $k_1 = 2k_2$ tells us that the reaction to the right in (3.3.1) is twice as strong as the reaction going to the right in (3.3.3): this is because in the former, there are two binding sites available, working independently, whereas in the latter, one of the sites is already occupied and hence only one of the binding sites can participate in the reaction. Hence the former reaction has a probability to occur which is twice as large as the latter. For the equality $k_{-2} = 2k_{-1}$, the substrate S can more easily break off from the complex SEES than from the complex EES, again with twice the probability to occur. This is because the substrate from either side of SEES can break off the complex, and since both sites are independent, this gives a factor two. The same conclusion holds for the equality $k_4 = 2k_3$: both subunits can produce a product particle, and since both work independent from each other, this reaction occurs with a rate equal to twice the rate compared to the case in which only one site is occupied.

Using these rates, we have $K_{m2} = 4K_{m1}$. We can use this in equation (3.3.14) to find

$$\frac{dp}{dt} = \frac{2k_3e_0s(2K_{m1} + s)}{4K_{m1}^2 + 4K_{m1}s + s^2}. \quad (3.3.17)$$

In the denominator, we recognise $(2K_{m1} + s)^2$, and this simplifies with the factor in the numerator, yielding

$$\frac{dp}{dt} = \frac{2k_3e_0s}{2K_{m1} + s} \equiv \frac{v_{\max}s}{K_m + s}, \quad (3.3.18)$$

where we defined the parameters

$$v_{\max} = 2k_3e_0, \quad K_m = 2K_{m1}. \quad (3.3.19)$$

The equation (3.3.18) implies that the system follows the usual Michaelis-Menten kinetics for the rates given in equation (3.3.16).

4 Motifs

4.1 Motifs in the E. Coli Gene Regulatory Network

The regulatory network of the bacteria E. Coli is given to us in a `txt` file, where a number of different proteins, represented as nodes, are in interaction with each other, represented as edges. The file `coliInterFullNames.txt` gives a dictionary linking the number value to the name of the protein. From this, we see that there are 424 different proteins in the E. Coli bacteria which are relevant for our problem. Hence the number of nodes of the network is $N = 424$. The number of edges is given by the number of rows in the file `coliInterFullVec.txt`, and we find that $E = 577$ for our problem. We will look for motifs in the gene regulatory network of E. Coli.

4.1.1 Selfregulation

We are first of all interested in the number of selfregulating proteins N_{self} in the E. Coli network. This number can be determined via a Python script, which checks whenever the number in the x and y column of the given data match with each other, indicating that this row represents an interaction of a certain protein with itself. There are 58 selfregulating proteins: 14 are self activators, 41 are self repressors and for 3 selfregulating proteins, the type of reaction is unknown.

We can analytically calculate the average number of selfregulating nodes in a random network, which we'll denote as $\langle N_{\text{self}} \rangle$. The following derivation is based on chapter 3 from Uri Alon's book [1].

In a random network, we choose a pair of nodes (X, Y) at random, of which one is the origin, and the other is the destination. There is a probability of $p_{\text{self}} = 1/N$ to form a self-edge (i.e. a pair of nodes with $X = Y$). Since there are E edges, the probability of having precisely k self-edges is therefore given approximately by a binomial distribution P with probability of success p_{self} , such that

$$P(k) = \binom{E}{k} p_{\text{self}}^k (1 - p_{\text{self}})^{E-k}. \quad (4.1.1)$$

The reason that it is *approximately* binomial is due to the fact that we ignored above that we cannot make two self-edges using the same node and hence p_{self} depends on the number of self-edges that are already formed. For sparse networks (defined later on), of which the E. Coli network is an example, p_{self} does not change much and the above probability distribution is a good approximation. The mean of the above distribution is

$$\langle N_{\text{self}} \rangle \approx E p_{\text{self}} \sim E/N. \quad (4.1.2)$$

For the parameters of the E. Coli network, this gives

$$\langle N_{\text{self}} \rangle \approx 1.3608. \quad (4.1.3)$$

We can also compare this by creating 2000 random networks (see later on) and compute the average number of selfregulating proteins. On a certain run of this algorithm, we found a value 1.3550, which is quite close to the analytically determined value.

We see that the E. Coli network has much more selfregulating proteins than expected for a random network, and hence we conclude that selfregulation is a network motif.

4.1.2 Feed forward loops

Another interesting regulation pattern is the feed forward loop (FFL). Note that we only consider the loops where all three proteins are different from each other as FFL's, and where all three interactions are activators, as denoted in Figure 4.1.1. To find the feed forward loops, we will create a dictionary in which every protein is represented as a key. The value corresponding to the key is a list of all the proteins that are activated by the 'key' protein. Using this, we can count the number of FFL's using the following logic. Let X, Y and Z be three proteins. Denote by P_X the set of all proteins activated by protein X . Then we count the number of FFL's N_{FFL} as follows:

$$\forall X : \forall Y \in P_X \setminus \{X\} : \forall Z \in P_Y \setminus \{X, Y\} : Z \in P_X \Rightarrow N_{\text{FFL}}+ = 1, \quad (4.1.4)$$

where $+$ = denotes we increase the value of N_{FFL} by one. Such a function is implemented in Python. In the E. Coli file, we then find 23 FFL's.

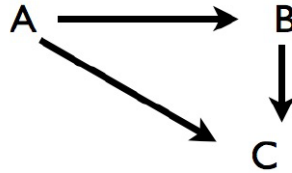


Figure 4.1.1: Schematic representation of the feed forward loop. Note that we will assume $A \neq B \neq C$, and that all three interactions represent activators.

We can analytically compute the expected number of FFL's in a random network. The following derivation is based on chapter 4 of Uri Alon's book [1].

We form random networks by inserting E edges between the N nodes. The total number of edges possible is $N(N - 1) + N = N^2$, where the first term represents edges between different nodes, while the second term represents self-edges. Hence the probability for a

certain edge to occur is $p = E/N^2$. The E. Coli network is an example of a *sparse* network, for which it holds that $p \ll 1$, since we have $p = 0.0032$. Let G be the subgraph representing the FFL. This subgraph has $n = 3$ nodes and $g = 3$ edges. To generate such a subgraph G in a larger graph, we need to choose n different nodes and place g edges between them. Finally, we have to take into account the probability p_{act} that each of the edges in the FFL is an activator. In the E. Coli network, about $p_{\text{act}} = 58.06\%$ of the interactions are activators. For the FFL, we then find

$$\langle N_{\text{FFL}} \rangle = N(N-1)(N-2)p^g p_{\text{act}}^g. \quad (4.1.5)$$

For the parameters of the E. Coli network, we then find

$$\langle N_{\text{FFL}} \rangle = 0.4897. \quad (4.1.6)$$

We will now compare this to the number of FFL's we would find in a random network. For this, a Python function is written which creates a random network with the same number of nodes and edges as the E. Coli file. A number of features from the E. Coli file are taken into account. First of all, we have to avoid that the function would give twice an interaction between two nodes in the same 'direction'. Second, we would like to create a random network of which the structure of the interactions is similar to the E. Coli network. For this, we first determine the relative amounts of activators, repressors, and unknown interactions in the E. Coli file. We find 58.06% of the interactions are activators, 36.92 % are repressors, and 5.03 % are unknown. When building our random network, we will use these numbers as probabilities to choose a certain type of interaction by generating a random number between 0 and 1. If one wants to create totally random networks, there is the option to give an equal probability for each interaction type.

The Python function then works schematically as follows: choose a pair of numbers (X, Y) , both between 1 and the desired number of nodes N . If the pair (X, Y) was already generated, discard and repeat this step (note that order matters, since this gives the 'direction' of interaction, namely from X to Y). If the pair (X, Y) was not yet generated, choose an interaction based on the given probabilities for them to occur. Repeat until the desired number of edges is reached.

Generating 2000 random networks, we find that the average number of FFL's occurring in a random network is 0.4880, which is quite close to the analytically determined value. We see that the number of FFL's in the E. Coli network is much higher than the average for a random network (especially if we would also count FFL's where not all the interactions are activating), and hence we can conclude that FFL is a network motif.

4.2 Positively autoregulated protein

The previous problem showed in an explicit example that autoregulation is a network motif. We consider here the case of a positively autoregulated protein whose production is governed

by the following differential equation

$$\frac{dX}{dt} = \frac{\beta X^n}{X^n + K^n} - \alpha X. \quad (4.2.1)$$

The first term is a Hill function with Hill coefficient n . We first non-dimensionalize the above differential equation by rescaling X and t appropriately. Assume that X is a concentration. Then α has the dimensions of an inverse time, and K the dimensions of a concentration. Define

$$\tau \equiv \alpha t, \quad U \equiv \frac{X}{K}. \quad (4.2.2)$$

Then the above differential equation becomes

$$\frac{dU}{d\tau} = \frac{\beta}{\alpha K} \frac{U^n}{U^n + 1} - U, \quad (4.2.3)$$

which is a differential equation depending on dimensionless coefficients. The dynamics is governed by a single parameter, namely $\gamma \equiv \beta/(\alpha K)$.

Let us first restrict to the case $n = 1$ in the differential equation (4.2.1), and look for fixed points of the equation. Thus we want to solve

$$\beta X - \alpha(X + K)X = 0, \quad (4.2.4)$$

of which the solutions are $X = 0$ and

$$X^* = \frac{\beta - \alpha K}{\alpha}. \quad (4.2.5)$$

We see that for $\beta > \alpha K$, the fixed point is positive. Defining the right hand side of (4.2.1) as $F_1(X)$ for $n = 1$, we find that the derivative is

$$F'_1(X) = \frac{\beta K}{(X + K)^2} - \alpha, \quad (4.2.6)$$

and hence, we can compute

$$F'_1(X^*) = \alpha \left(\frac{\alpha K}{\beta} - 1 \right). \quad (4.2.7)$$

For the values of the parameters in which the fixed point X^* is greater than zero, which is $\beta > \alpha K$, this is a stable fixed point since the above derivative is negative. Note that we will always assume $\alpha > 0$, since the second term in equation (4.2.1) represents the degradation of the protein.

We now solve the above differential equation numerically. We set the parameters to $\alpha = 1$, $\beta = 1$ and $K = 1/4$ and take as initial condition $X(0) = 10^{-3}$. Note that this satisfies $\beta > \alpha K$, and hence there is a stable fixed point X^* which is strictly positive. Using equation (4.2.5), we find that $X^* = 0.75$. We will compare the solution for the above

differential equation, representing an autoregulated protein, with a non-regulated protein, for which the differential equation was already seen before:

$$\frac{dX}{dt} = \beta - \alpha X. \quad (4.2.8)$$

We would like to recall (as is readily seen from the above differential equation), that the non-regulated protein differential equation has a fixed point for $X = \beta/\alpha$, and that this is always a stable fixed point. The analytic solution to the above differential equation was computed in the lectures, and we found

$$X(t) = \frac{\beta}{\alpha} \left(1 - e^{-\alpha t}\right). \quad (4.2.9)$$

Below, we take the same parameters for the non-regulated protein as for the auto-regulated protein, and hence the non-regulated equation has a fixed point at $X^* = 1$. The numerically obtained solutions for both differential equations are shown in Figure 4.2.1 below. As expected, both solutions tend towards their fixed point.

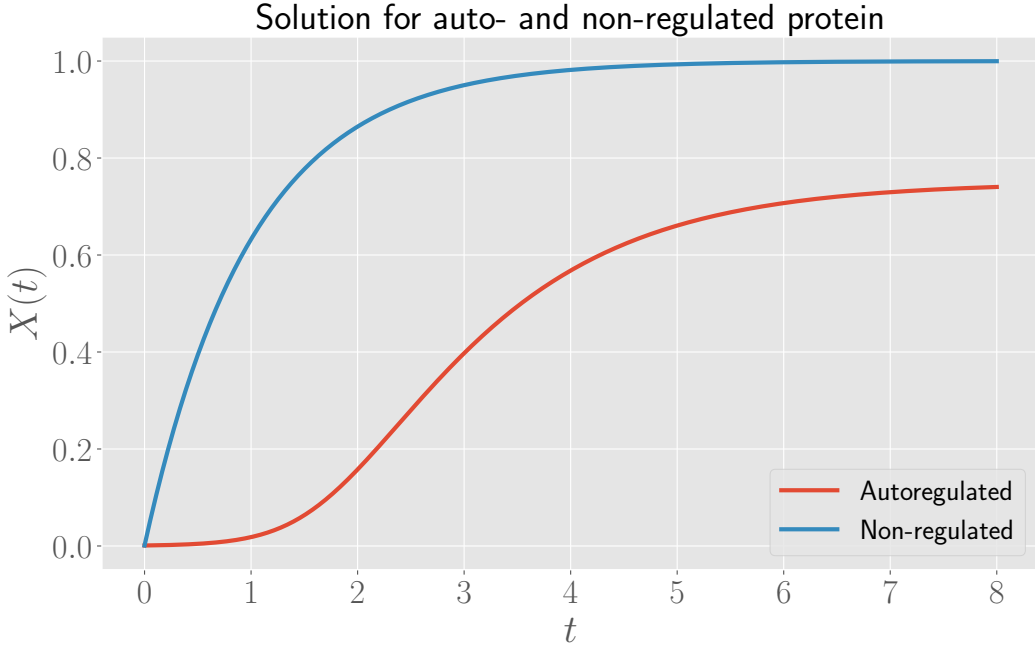


Figure 4.2.1: Numerical solutions for the autoregulated and non-regulated protein, with differential equations shown in (4.2.1) and (4.2.8), respectively, for the values $\alpha = \beta = 1$, $K = 1/4$ and initial condition $X(0) = 10^{-3}$.

We will now determine the response time, which is the time for the system to reach half of the stationary value concentration, for the two cases and compare them with each other.

The response time for the non-regulated system can be computed using the analytic solution given above, and for the parameters currently considered, we find

$$T_R^{\text{non}} = \frac{\ln 2}{\alpha} = 0.6931. \quad (4.2.10)$$

For the autoregulated system, we will use the graph in Figure 4.2.1 to estimate this value (recall that the stationary concentration is at $X^* = 0.75$ for the autoregulated protein). We find

$$T_R^{\text{auto}} \approx 2.9. \quad (4.2.11)$$

Hence the response time for the autoregulated protein is much longer than the response time for the non-regulated protein.

Now let us consider the case $n = 2$ in equation (4.2.1). We look for the fixed points of the differential equation and hence for solutions of the equation

$$\frac{\beta X^2}{X^2 + K^2} - \alpha X = 0. \quad (4.2.12)$$

A first solution is $X = 0$. Other solutions are solutions to the differential equation

$$\alpha X^2 - \beta X + \alpha K^2 = 0. \quad (4.2.13)$$

The solutions are

$$X_{\pm}^* = \frac{\beta \pm \sqrt{\beta^2 - 4\alpha^2 K^2}}{2\alpha}. \quad (4.2.14)$$

However, these fixed points only appear if $\beta > 2\alpha K$, since otherwise the square root is not a real number. For this range of the parameters, there is bistability. To prove this claim, let us consider the stability of the fixed points. Define the right hand side of (4.2.1) to be $F_2(X)$ for $n = 2$. A short calculation shows that

$$F'_2(X) = \frac{2\beta K^2 X}{(X^2 + K^2)^2} - \alpha, \quad (4.2.15)$$

from which we immediately see that the origin is always stable, for all values of the parameters. Determining the sign of $F'_2(X)$ at the solutions X_{\pm}^* is straightforward but more tedious, and it is much easier to plot F_2 and F'_2 for various values of the parameters via an applet such as Desmos. In [this Desmos applet](#), one can plot the two individual terms in (4.2.1) or both terms simultaneously and also the derivative of the right hand side. The applet also prints 'bistability' or 'no bistability', depending on the specific values of the parameters. We see that whenever there are three fixed points (i.e. for $\beta > 2\alpha K$, and hence whenever the applet prints 'bistability') the origin and the fixed point X_+^* are stable, while the fixed point X_-^* is unstable. Since $\beta > \alpha K$, the fixed point X^* is also stable. This is indeed the behaviour we expect from a system with bistability.

4.3 Genetic toggle switch

We consider two transcription factors mutually repressing each other. This system can become bistable and thus can be considered as a genetic switch. To understand qualitatively bistability, we consider the case in which the concentration of X is high such that the production of Y is repressed and Y has a low concentration. If this happens, Y cannot repress X , which then maintains its high concentration. The other possibility is a symmetric situation in which the role of X and Y is interchanged. Bistability occurs only for some specific choice of model and parameters. To understand this, the model we will consider is

$$\frac{dX}{dt} = \frac{\beta K^n}{Y^n + K^n} - \alpha X. \quad (4.3.1)$$

$$\frac{dY}{dt} = \frac{\beta K^n}{X^n + K^n} - \alpha Y. \quad (4.3.2)$$

We first perform a non-dimensionalization of the above differential equations. Assume that X and Y carry the dimensions of concentration. From the above equations, we see that α then is an inverse time, K has the dimension of concentration, and hence β carries dimensions concentration over time. So define

$$\tau \equiv \alpha t, \quad U \equiv \frac{X}{K}, \quad V \equiv \frac{Y}{K}. \quad (4.3.3)$$

Then the above differential equations become

$$\frac{dU}{d\tau} = \frac{\beta}{\alpha K} \frac{1}{V^n + 1} - U \quad (4.3.4)$$

$$\frac{dV}{d\tau} = \frac{\beta}{\alpha K} \frac{1}{U^n + 1} - V, \quad (4.3.5)$$

and these differential equations indeed have prefactors which are dimensionless. The form of these equations is similar to the non-dimensionalized equation in the previous exercise.

We now show that if $n = 1$, there is no bistability. For this, we will show that the above differential equations have a single fixed point (X^*, Y^*) with $X^* = Y^*$. The fixed point is a solution of the system of equations

$$\begin{cases} \beta K - \alpha(Y + K)X = 0 \\ \beta K - \alpha(X + K)Y = 0 \end{cases}. \quad (4.3.6)$$

By demanding that the second term in both equations equal each other, we easily derive the equation $X = Y$. Using $X = Y$ in the first equation, we find the equation

$$\alpha Y^2 + \alpha KY - \beta K = 0. \quad (4.3.7)$$

This quadratic equation has two solutions, but we will only keep one of the solutions since the other one is negative, which is physically impossible. The solution is

$$X^* = Y^* = \frac{-\alpha K + \sqrt{\alpha^2 K^2 + 4\alpha\beta K}}{2\alpha}. \quad (4.3.8)$$

Hence we can conclude that for $n = 1$, there is one fixed point (X^*, Y^*) which satisfies $X^* = Y^*$.

Now we consider the case $n = 2$. The fixed points are solutions of the system of equations

$$\begin{cases} \beta K^2 - \alpha X(Y^2 + K^2) = 0 \\ \beta K^2 - \alpha Y(X^2 + K^2) = 0 \end{cases}. \quad (4.3.9)$$

Like before, we can demand that the second term in the above equations are equal to each other. This gives the equation

$$XY^2 + K^2X = X^2Y + K^2Y, \quad (4.3.10)$$

and from this, we find

$$XY(Y - X) = K^2(Y - X). \quad (4.3.11)$$

One solution is given by $X^* = Y^*$, which is a symmetric solution. If we assume that the fixed point is not symmetric, i.e. that $X^* \neq Y^*$, we find that the asymmetric fixed points satisfy $X^*Y^* = K^2$.

These considerations allow us to explicitly find the fixed points. For the symmetric fixed points, we replace one of the above equations by $X = Y$. Using the first equation above then results in

$$\alpha X^3 + \alpha KX - \beta K^2 = 0. \quad (4.3.12)$$

The solution to this equation is obtained via the cubic formula, as given for example [here](#), and gives

$$X^* = \sqrt[3]{\frac{\beta K^2}{2\alpha} + \sqrt{\frac{\beta^2 K^4}{4\alpha^2} + \frac{K^6}{27}}} + \sqrt[3]{\frac{\beta K^2}{2\alpha} - \sqrt{\frac{\beta^2 K^4}{4\alpha^2} + \frac{K^6}{27}}}, \quad (4.3.13)$$

which is positive for all values of the parameters. It will prove to be convenient to write down the dependence of X^* on the dimensionless parameter $\gamma \equiv \beta/(2\alpha K)$ (note that there is a factor 2 different relative to the parameter γ from the previous exercise). We find

$$X^*(\gamma) = K \left(\sqrt[3]{\gamma + \sqrt{\gamma^2 + \frac{1}{27}}} + \sqrt[3]{\gamma - \sqrt{\gamma^2 + \frac{1}{27}}} \right). \quad (4.3.14)$$

To find the asymmetric fixed points, we replace one of the equations in (4.3.9) by $XY = K^2$, and hence $Y = K^2/X$. Substituting this in the first equation, we find the following quadratic equation for X

$$\alpha X^2 - \beta X + \alpha K^2 = 0. \quad (4.3.15)$$

The solutions of this equation are

$$X_{\pm} = \frac{\beta \pm \sqrt{\beta^2 - 4\alpha^2 K^2}}{2\alpha}, \quad (4.3.16)$$

and the relation $XY = K^2$ then gives the Y component of these fixed points. We will refer to the fixed points (X_+, Y_+) , (X_-, Y_-) as the 'asymmetric fixed points', and refer to (X^*, Y^*) as the 'symmetric fixed point'. We see that the asymmetric fixed points only exist for $\beta > 2\alpha K$. For $\beta < 2\alpha K$, there is only one symmetric fixed point. Hence we can conclude that $\beta = 2\alpha K$ is a bifurcation value. This can be verified graphically by playing with the various parameters and plotting the nullclines via [this Desmos applet](#).

To determine the nature of the fixed points, we have to calculate the Jacobian matrix. The Jacobian matrix is

$$J(X, Y) = \begin{pmatrix} -\alpha & -\frac{2\beta K^2 Y}{(Y^2 + K^2)^2} \\ -\frac{2\beta K^2 X}{(X^2 + K^2)^2} & -\alpha \end{pmatrix}. \quad (4.3.17)$$

The trace of the Jacobian matrix is -2α , and its determinant is

$$\det J(X, Y) = \alpha^2 - 4 \frac{\beta^2 K^4 XY}{(X^2 + K^2)^2 (Y^2 + K^2)^2}. \quad (4.3.18)$$

Note that for all three fixed points, the trace is always equal to -2α . Let us first look at the symmetric fixed point, for which $X^* = Y^*$. We then have¹

$$\det J(X, X) = \alpha^2 - 4 \frac{\beta^2 K^4 X^2}{(X^2 + K^2)^4}. \quad (4.3.19)$$

The sign of this determinant will flip for a certain value of X . For this, we will look for the roots of the equation $\det J(X, X) = 0$. We can use the formula for the difference of two squares, giving two equations. However, one of these equations will only hold for $\alpha = 0$ and $X = 0$, and is not physically relevant. Hence we only keep the equation

$$\alpha = \frac{2\beta K^2 X}{(X^2 + K^2)^2}. \quad (4.3.20)$$

To go further, we recall that X is a fixed point and hence satisfies equations (4.3.9). We can use this to rewrite

$$X^2 + K^2 = \frac{\beta K^2}{\alpha X}. \quad (4.3.21)$$

Substituting into our previous expression, we find that the root of $\det J(X, X) = 0$ lies at

$$X_0 \equiv \left(\frac{\beta K^2}{2\alpha} \right)^{1/3}. \quad (4.3.22)$$

¹We will drop the star superscript to simplify notation.

Using $\gamma = \beta/(2\alpha K)$, we find the following dependence of X_0 on γ

$$X_0(\gamma) = K\gamma^{1/3}. \quad (4.3.23)$$

We can verify, using the Desmos applet mentioned above, that $\det J(X, X)$ indeed changes sign when going from $X < X_0$ to $X > X_0$, from positive to negative. We expect this change of sign to occur at the bifurcation value $\beta = 2\alpha K$ or $\gamma = 1$. We can easily compute, using (4.3.14), that $X^*(\gamma = 1) = K$, and we see that $X_0(\gamma = 1) = K$. So at the bifurcation value, the symmetric fixed point is the root of $\det J(X, X) = 0$. Moreover, $X^*(\gamma)$ is an increasing function in γ , as is verified easily by a plot (see the Desmos applet). Hence we can conclude that for $\beta < 2\alpha K$, the symmetric fixed point is a stable fixed point, while it is a saddle node for $\beta > 2\alpha K$.

Let us now focus on the asymmetric fixed points. We will now show that the determinant of the Jacobian evaluated at (X_+, Y_+) and (X_-, Y_-) are equal to each other. First of all, note that for these fixed points, we have²

$$\begin{aligned} (X^2 + K^2)^2(Y^2 + K^2)^2 &= (X^2 + K^2)^2 \left(\frac{K^4}{X^2} + K^2 \right)^2 \\ &= \frac{K^4}{X^4} (K^2 + X^2)^4 \\ &= K^4 \left(X + \frac{K^2}{X} \right)^4, \end{aligned} \quad (4.3.24)$$

where in the first step, we used the defining relation for the asymmetric fixed points $XY = K^2$. As an intermediate step, we can show that

$$\begin{aligned} X + \frac{K^2}{X} &= \frac{\beta \pm \sqrt{\beta^2 - 4\alpha^2 K^2}}{2\alpha} + \frac{2\alpha K^2}{\beta \pm \sqrt{\beta^2 - 4\alpha^2 K^2}} \\ &= \frac{(\beta \pm \sqrt{\beta^2 - 4\alpha^2 K^2})^2 + 4\alpha^2 K^2}{2\alpha (\beta \pm \sqrt{\beta^2 - 4\alpha^2 K^2})} \\ &= \frac{2\beta^2 \pm 2\beta\sqrt{\beta^2 - 4\alpha^2 K^2}}{2\alpha(\beta \pm \sqrt{\beta^2 - 4\alpha^2 K^2})} = \frac{\beta}{\alpha}, \end{aligned} \quad (4.3.25)$$

and hence we can conclude that

$$(X^2 + K^2)^2(Y^2 + K^2)^2 = K^4 \left(\frac{\beta}{\alpha} \right)^4. \quad (4.3.26)$$

Using our earlier expression for the determinant, we find

$$\det J(X_{\pm}, Y_{\pm}) = \alpha^2 \left(1 - 4 \frac{\alpha^2 K^2}{\beta^2} \right), \quad (4.3.27)$$

²We will drop the plus and minus indices to simplify the notation.

which is indeed the same for both asymmetric fixed points. Moreover, the sign of this determinant is always positive, since these asymmetric fixed points only exist for $\beta > 2\alpha K$. Since the trace is equal to -2α , the asymmetric fixed points will always be stable (stable node or stable spiral).

In the aforementioned Desmos applet, we can plot the determinant and trace of the Jacobian evaluated for the one or three fixed points (depending on the range of parameters) in a $(\det A, \text{tr } A)$ plane, along with the curve $\text{tr } A = \frac{1}{4}(\det A)^2$ like we did in the lectures. We can use the applet to verify all of the above calculations and conclusions. Playing around with the parameters in the Desmos applet, we can verify graphically that the asymmetric fixed points are always stable (moreover, they are almost always stable nodes), while the symmetric fixed point is a saddle node for $\beta > 2\alpha K$ and stable for $\beta < 2\alpha K$.

Finally, we give the full phase portrait of the system for $n = 2$ and parameters $\alpha = 1 = \beta$ and $K = 1/4$ in Figure 4.3.1 below. We see that the fixed points indeed have the nature that we expected from the conclusions made above.

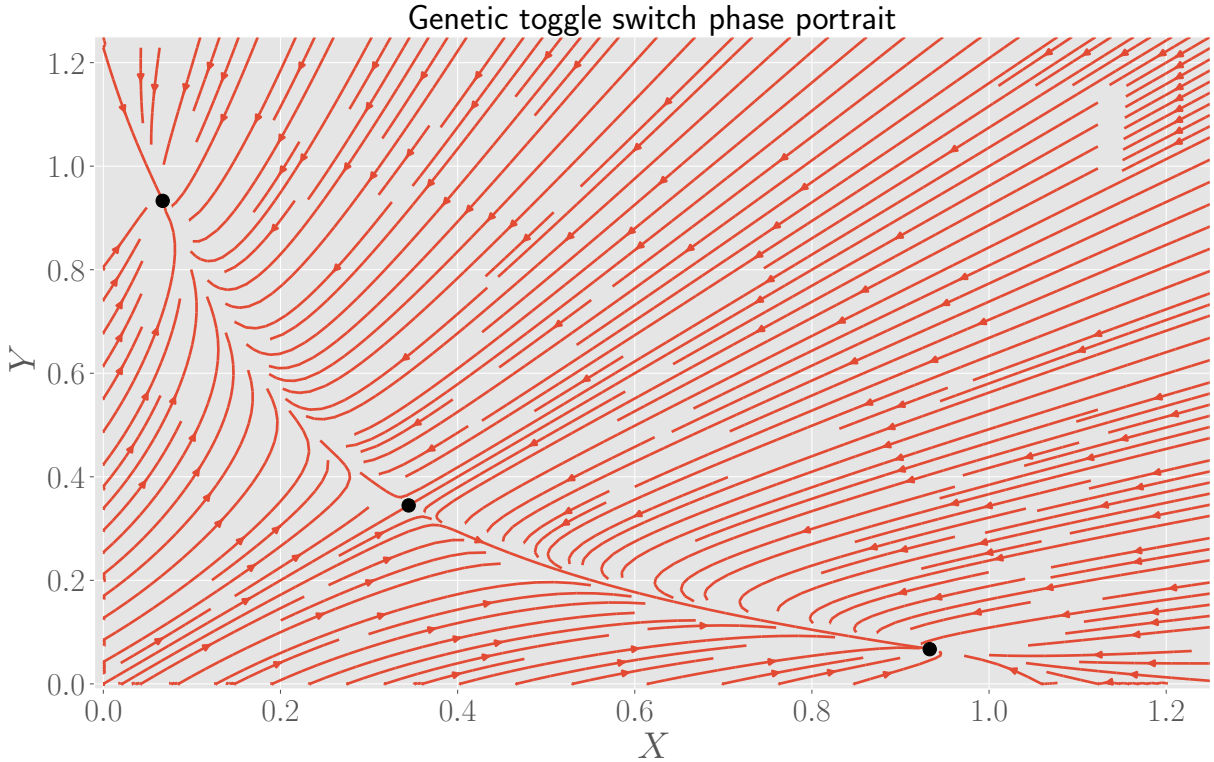


Figure 4.3.1: Phase portrait of the system for $n = 2$ and parameters $\alpha = 1 = \beta$ and $K = 0.25$. The black dots denote the fixed points.

5 Non-linear oscillators and limit cycles

5.1 The Goodwin model

The Goodwin model is one of the simplest models of biological oscillators. Below, we will focus mostly on the case of 3 components. Afterwards, we will sketch the generalization of the Goodwin model to N component systems.

5.1.1 Three components

The Goodwin model for a three component system is described by the following three differential equations (in non-dimensionalized form)

$$\frac{dx}{dt} = \frac{1}{1+z^p} - bx \quad (5.1.1)$$

$$\frac{dy}{dt} = b(x-y) \quad (5.1.2)$$

$$\frac{dz}{dt} = b(y-z), \quad (5.1.3)$$

where $b > 0$. We limit ourselves to $x, y, z > 0$, because we can imagine that x , y and z represent the concentration of mRNA, protein and end product, respectively (if we start from differential equations with correct dimensions, see for example [6]). Therefore, we can interpret b as the rate of transcription, translation, catalysis and degradation of the three species. Note that a more general version of the Goodwin model can be constructed by having a different rate b in each of the above equations, but this assumption of equal rates simplifies the analysis. There is only one non-linear term in the model describing repression of the variable z on x . Furthermore, we see that x is an activator for y , and y is an activator for z such that this network represents a negative feedback loop. Define F_1, F_2, F_3 to be the right hand sides of the above equations (i.e. $F_1(x, y, z) = \dot{x}$ et cetera). Below, we will use the lecture and the YouTube video by professor Carlon [2] as inspiration.

The above equations have a unique fixed point. From the second and third equation, we infer that a fixed point (x^*, y^*, z^*) of the system satisfies $x^* = y^* = z^* \equiv \xi$. From the first equation, we find that ξ has to be a solution of

$$1 - b\xi - b\xi^{p+1} = 0, \quad (5.1.4)$$

and we have to show there is only one solution to this equation. Let $f(x)$ denote the function at the left hand side of equation (5.1.4). Then

$$f'(x) = -b - b(p+1)x^p. \quad (5.1.5)$$

Since $f'(x) < 0$ for all $x > 0$ and all values of p , $f(x)$ is a strictly decreasing function in x . Since $f(0) = 1$, the graph of f will cross the x -axis a single time, such that $f(x)$ indeed has one zero in the half plane $x > 0$. Therefore, there is a unique fixed point $\Xi = (\xi, \xi, \xi)$. Note that ξ satisfies

$$b\xi = \frac{1}{1 + \xi^p}, \quad (5.1.6)$$

from which we can derive the equation

$$\xi^p = \frac{1}{b\xi} - 1. \quad (5.1.7)$$

We now claim that the model fixed point undergoes a Hopf bifurcation for $p > 8$, while there is no Hopf bifurcation for $p < 8$. For this, we will investigate the Jacobian matrix evaluated at the unique fixed point. The only non-trivial entry in the Jacobian matrix will be the non-linear term. For this, define

$$\Phi \equiv -\frac{\partial F_1(x, z)}{\partial z} \Big|_{\Xi} = \frac{p\xi^{p-1}}{(1 + \xi^p)^2}. \quad (5.1.8)$$

Using both equations (5.1.6) and (5.1.7), this can be written as

$$\Phi = \frac{p}{\xi} \xi^p b^2 \xi^2 = \frac{p}{\xi} \left(\frac{1}{b\xi} - 1 \right) b^2 \xi^2 = \frac{p}{\xi} \left(\frac{1 - b\xi}{b\xi} \right) b^2 \xi^2 = pb(1 - b\xi). \quad (5.1.9)$$

The other entries of the Jacobian can be easily read off from the above differential equations. We find

$$J(\Xi) = \begin{pmatrix} -b & 0 & -\Phi \\ b & -b & 0 \\ 0 & b & -b \end{pmatrix}. \quad (5.1.10)$$

To find the eigenvalues of this Jacobian matrix, we start by writing down the characteristic polynomial $G(\lambda) \equiv \det(J(\Xi) - \lambda)$, which becomes

$$G(\lambda) = -(b + \lambda)^3 - b^2\Phi, \quad (5.1.11)$$

such that eigenvalues are solutions of

$$\lambda^3 + 3b\lambda^2 + 3b^2\lambda + b^3 + b^2\Phi \equiv \lambda^3 + A\lambda^2 + B\lambda + C = 0. \quad (5.1.12)$$

In the lectures, we saw that for a characteristic polynomial of this form, we have a Hopf bifurcation at $AB = C$, which, using equation (5.1.9) becomes

$$9b^3 = b^3 + pb^3(1 - b\xi). \quad (5.1.13)$$

This condition can be further simplified to

$$b\xi = 1 - \frac{8}{p}. \quad (5.1.14)$$

Since $b > 0$ and $\xi > 0$ by assumption, we see that this condition can never be satisfied if $p < 8$, since in that case the right hand side is a negative number. However, if $p > 8$, then there is a Hopf bifurcation. By the Routh-Hurwitz theorem [6], if $b\xi > 1 - \frac{8}{p}$, the fixed point is stable, while if $b\xi < 1 - \frac{8}{p}$, the fixed point is unstable.

The condition $p > 8$ means the system must have an unrealistically high value for the cooperativity parameter p , and the degradation rates must be (nearly) equal to each other for the above analysis to hold: if this is not the case, the threshold value for p will be even larger [6]. Therefore, the Goodwin model is not easily realised in nature. A modified version of the Goodwin model which fixes these issues is the model by Bliss, Painter and Marr, which is discussed in [6]. We will not delve deeper into this model in this exercise.

Finally, we would like to remark that instead of exploiting the condition $AB = C$, we could also directly find the roots of $G(\lambda)$, which are

$$\lambda_1 = -b - \sqrt[3]{p(1 - b\xi)} < 0, \quad (5.1.15)$$

$$\lambda_{2,3} = -b + \sqrt[3]{p(1 - b\xi)} \left[\cos\left(\frac{\pi}{3}\right) \pm i \sin\left(\frac{\pi}{3}\right) \right]. \quad (5.1.16)$$

The fixed point becomes unstable if $\text{Re}(\lambda_{2,3}) > 0$, and some algebraic manipulations will then give the same condition as above. It is this second method that we will generalize to the case of multi-component systems in the next subsection.

We will now integrate the above differential equations of the Goodwin model, with parameter values $b = 1/4$ and $p = 12$. For this choice of parameters, the fixed point is unstable, as can easily be verified graphically by plotting the right hand side of dx/dt . For this, we plot the two terms of this function separately, defining $F_1(x) = F_+(x) - F_-(x)$ (we will substitute x for z since we are interested in the fixed point, which is symmetric). The fixed point lies at the intersection of these two curves. Since $F_-(x) = bx$, the plot allows us to quickly verify that the fixed point is unstable by comparing the y -coordinate of the fixed point (which is $b\xi$) with $1 - 8/p$, shown as a grey dashed line in Figure 5.1.1 below. Since $b\xi < 1 - 8/p$, the fixed point is indeed unstable.

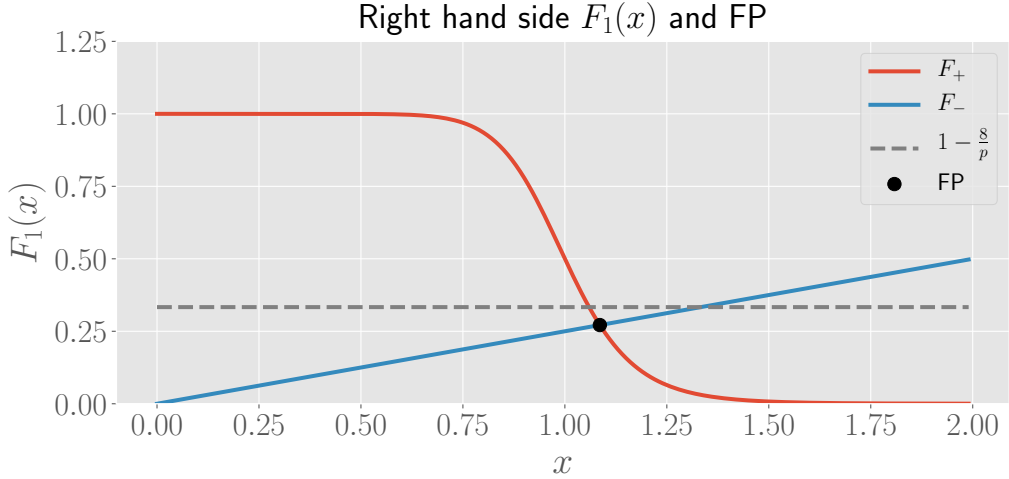


Figure 5.1.1: Plot of the two terms in $F_1(x)$, for $b = 1/4$ and $p = 12$, such that $\xi \approx 1.0858$. The fixed point lies at the intersection of the two curves, and is unstable for this choice of parameters.

Now we will plot the trajectories of the solutions of the Goodwin model for various initial conditions (which can be found in the Jupyter Notebook) in the xy , yz and xz planes. The result is shown in Figure 5.1.2 below. The figure shows that the solutions tend towards a limit cycle. This limit cycle appears more clearly if we restrict the plots to the second half of the datapoints of the numerically obtained solutions shown in Figure 5.1.2, which is shown in Figure 5.1.3. The limit cycle lies somewhere in the thin region between the two disconnected regions where the solutions lie. Indeed, in the outer part, the solutions spiral inwards towards the limit cycle, while in the inner part, the solutions will spiral outwards tending towards the limit cycle. Since the solutions tend towards the limit cycle from both sides (inside and outside), we can conclude the limit cycle is stable.

We remark that we can rigorously motivate the existence of the limit cycle by invoking the Poincaré-Bendixson theorem [5, p.203]. Indeed, if we look at each of the three projections, and take a large enough region R surrounding the fixed point, but not containing an arbitrarily small neighbourhood of the fixed point, then the plots show various possible trajectories that are confined in R . The Poincaré-Bendixson theorem then shows that there exists a closed orbit inside R . Since the plots show that the closed orbit is an isolated one, this shows there exists a limit cycle.

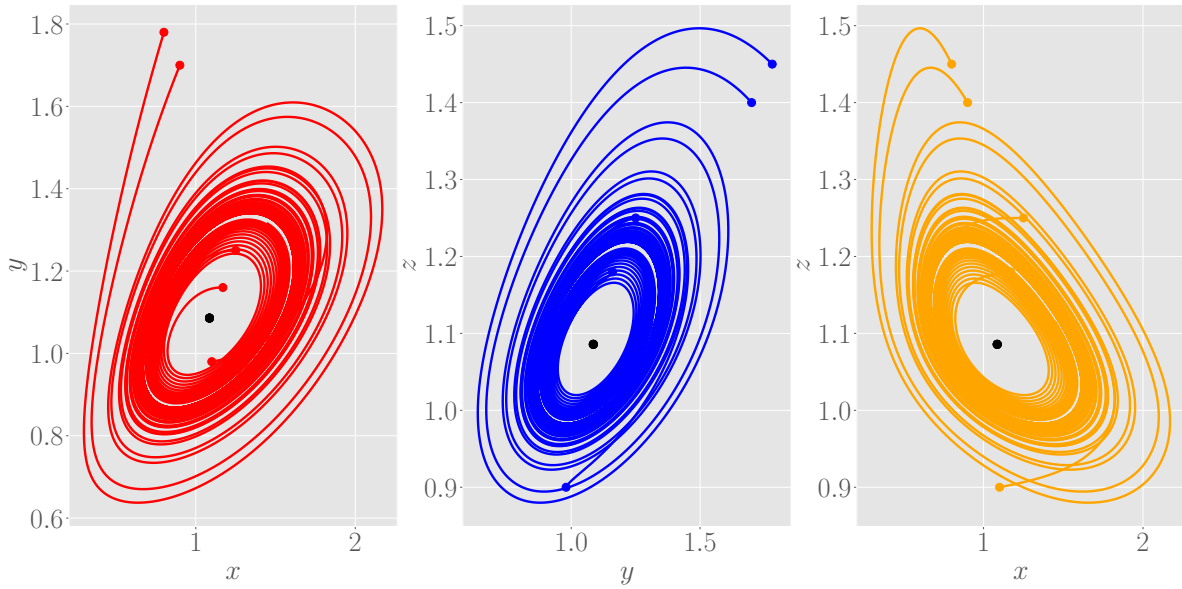


Figure 5.1.2: Solutions of the Goodwin model for various initial conditions (denoted as coloured dots), for parameters $b = 1/4$, $p = 12$, such that $\xi \approx 1.0858$ and the fixed point (black dot) is unstable. The solutions tend towards a limit cycle.

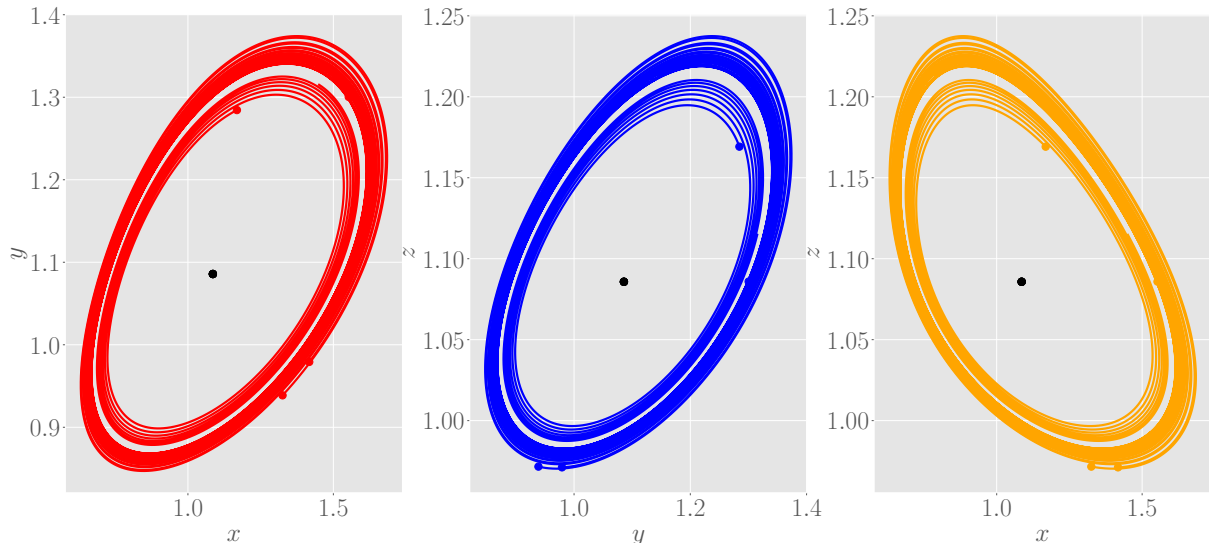


Figure 5.1.3: Second half of the solutions plotted in Figure 5.1.2, which makes it easier to spot the limit cycle. Note that the coloured dots now denote the starting location, after we have discarded the first half of the solutions.

5.1.2 Generalization to N components

We consider now a generalized Goodwin model with N components.

$$\frac{dx_1}{dt} = \frac{1}{1 + x_N^p} - bx_1 \quad (5.1.17)$$

$$\frac{dx_2}{dt} = b(x_1 - x_2) \quad (5.1.18)$$

$$\frac{dx_3}{dt} = b(x_2 - x_3) \quad (5.1.19)$$

...

$$\frac{dx_N}{dt} = b(x_{N-1} - x_N). \quad (5.1.20)$$

In this case, too, there is a unique fixed point. As before, fixed points should satisfy $x_1 = x_2 = \dots = x_N = \xi$. Requiring that \dot{x}_1 equals zero then gives the same equation as in the three component case as condition on ξ . As shown there, there is one solution to this equation, such that the fixed point is unique and given by $\Xi = (\xi, \xi, \dots, \xi)$ as before. The Jacobian of this system, evaluated at the fixed point, is

$$J(\Xi) = \begin{pmatrix} -b & 0 & 0 & \dots & -\Phi \\ b & -b & 0 & \dots & 0 \\ \vdots & \ddots & \ddots & \ddots & \vdots \\ 0 & \dots & b & -b & 0 \\ 0 & \dots & \dots & b & -b \end{pmatrix}, \quad (5.1.21)$$

where Φ is identical to Φ for the three component system, since Φ only depends on the coefficients in the \dot{x}_1 equation, which is independent of N . To find the eigenvalues of the above matrix, we need to find the zeroes of the characteristic polynomial. Therefore, the eigenvalues are solutions of

$$G(\lambda) = (b + \lambda)^N + pb^N(1 - b\xi) = 0, \quad (5.1.22)$$

where we again made use of equation (5.1.9) to rewrite the factor Φ . Taking the N -th root then gives N different complex eigenvalues

$$\lambda_n = -b + bp^{1/N}(1 - b\xi)^{1/N} e^{i\frac{\pi}{N}(2n+1)} \quad n = 0, 1, \dots, N-1. \quad (5.1.23)$$

Note that minus sign is taken inside the exponential factor. To find the Hopf-bifurcation point, we have to require that the complex eigenvalues with the largest real part satisfy $\operatorname{Re}(\lambda) = 0$. Indeed, if all eigenvalues have negative real part, the fixed point is stable, whereas if there are eigenvalues with positive real part, the fixed point becomes unstable. The real part of an eigenvalue is

$$\operatorname{Re}(\lambda_n) = -b + bp^{1/N}(1 - b\xi)^{1/N} \cos\left(\frac{\pi}{N}(2n+1)\right). \quad (5.1.24)$$

This is largest for $n = 0$ (so also for $n = N - 1$). We now determine when this eigenvalue crosses the imaginary axis, so

$$-b + bp^{1/N}(1 - b\xi)^{1/N} \cos\left(\frac{\pi}{N}\right) = 0. \quad (5.1.25)$$

Using some straightforward algebraic manipulations, we can derive

$$b\xi = 1 - \frac{1}{p \cos^N\left(\frac{\pi}{N}\right)}, \quad (5.1.26)$$

which is the generalization of the condition that we found earlier. We can check the above equation for $N = 3$, and since $\cos^3\left(\frac{\pi}{3}\right) = 1/8$, this indeed agrees with the result that we obtained in the previous subsection.

As was the case for the three component system, the above equation implies a constraint on p in order to have Hopf-bifurcation. As before, since $b\xi > 0$, p should be large enough such that the right hand side is positive as well, and this gives the requirement

$$p > \frac{1}{\cos^N\left(\frac{\pi}{N}\right)} \equiv p_{\min}^N. \quad (5.1.27)$$

In Figure 5.1.4 below, we plot p_{\min}^N as a function of N . We see that for increasing N , the threshold value of p decreases. Therefore, if we have a larger number of components, we can use lower values of the cooperativity parameter (if we want to have Hopf bifurcation), which allows for a more realistic situation compared to the three component system.

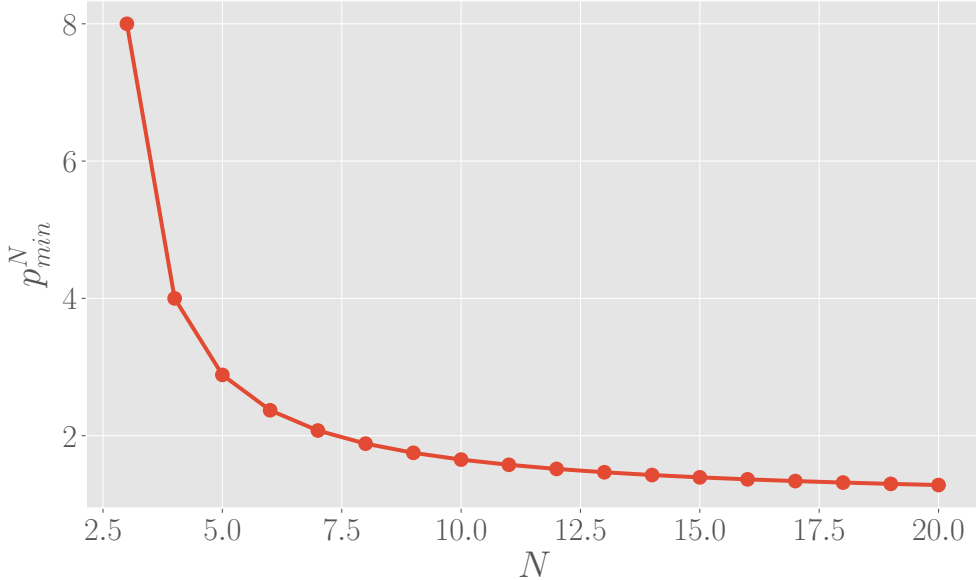


Figure 5.1.4: Plot of p_{\min}^N as a function of N (for $N \geq 3$), showing that the threshold value for p decreases for an increasing number of components in the system.

6 Chaos

6.1 The Lorenz system

The equations governing the Lorenz system with parameters σ , r and b are

$$\dot{x} = \sigma(y - x) \quad (6.1.1)$$

$$\dot{y} = rx - y - xz \quad (6.1.2)$$

$$\dot{z} = xy - bz. \quad (6.1.3)$$

Below, we will work with $b = 8/3$ and $\sigma = 10$, which are the values that Lorenz used originally, and vary the parameter r .

6.1.1 From waterwheel to Lorenz

In the lectures, it was claimed that the Lorenz equations are equivalent to the waterwheel equations [5, p.309]

$$\dot{a}_1 = \omega b_1 - K a_1 \quad (6.1.4)$$

$$\dot{b}_1 = -\omega a_1 + q_1 - K b_1 \quad (6.1.5)$$

$$\dot{\omega} = \frac{\pi gr}{I} a_1 - \frac{\nu}{I} \omega. \quad (6.1.6)$$

We will show this explicitly by considering a change of variables for the waterwheel equations which will lead to the Lorenz equations. For this, consider the following change of variables

$$a_1 = \frac{K\nu}{\pi gr} y \quad (6.1.7)$$

$$b_1 = -\frac{K\nu}{\pi gr} z + \frac{q_1}{K} \quad (6.1.8)$$

$$\omega = Kx \quad (6.1.9)$$

$$t = \frac{\tau}{K}. \quad (6.1.10)$$

For example, we can derive that (letting primes denote derivatives with respect to τ)

$$y' = \frac{dt}{d\tau} \frac{dy}{dt} = \frac{1}{K} \frac{\pi gr}{K\nu} \dot{a}_1, \quad (6.1.11)$$

and if we fill in the above change of variables, this gives

$$y' = \frac{\pi gr}{K^2\nu} \left[Kx \left(-\frac{K\nu}{\pi gr} z + \frac{q_1}{K} \right) - \frac{K^2\nu}{\pi gr} y \right] = \frac{\pi gr q_1}{K^2\nu} x - y - xz, \quad (6.1.12)$$

which is indeed similar to the differential equation for y in the Lorenz system, with Rayleigh number r (not to be confused with the parameter r from the waterwheel equations) equal to $\pi grq_1/K^2\nu$. Similarly, we have

$$x' = \frac{1}{K}\dot{x} = \frac{1}{K^2}\dot{\omega}, \quad (6.1.13)$$

and by using the above change of variables, we find

$$x' = \frac{1}{K^2} \left(\frac{\pi gr}{I} \frac{K\nu}{\pi gr} y - \frac{\nu}{I} Kx \right) = \frac{\nu}{KI} (y - x), \quad (6.1.14)$$

which is similar to \dot{x} from the Lorenz equations, if we set the Prandtl number σ equal to ν/KI . Finally, since

$$z = \frac{\pi gr}{K\nu} \left(\frac{q_1}{K} - b_1 \right), \quad (6.1.15)$$

we have that

$$z' = -\frac{\pi gr}{K^2\nu} \dot{b}_1 = -\frac{\pi gr}{K^2\nu} (-\omega a_1 + q_1 - Kb_1). \quad (6.1.16)$$

Substituting the change of variables again, this results in

$$z' = -\frac{\pi gr}{K^2\nu} \left[-Kx \frac{K\nu}{\pi gr} y + q_1 - K \left(-\frac{K\nu}{\pi gr} z + \frac{q_1}{K} \right) \right] = xy - z. \quad (6.1.17)$$

Surprisingly, using this transformation, the parameter b from the Lorenz equations is equal to one and hence independent of the parameters of the waterwheel equations. This is mentioned in exercise 9.1.3 in Strogatz [5], where he also states that the waterwheel equations are not quite as general as the Lorenz equations. However, we can still conclude that the waterwheel equations can be transformed into the Lorenz equations, as was to be shown.

6.1.2 Fixed points of the Lorenz equations

Let us determine the fixed points of the Lorenz system. A fixed point of the system is a solution of the equations

$$\begin{cases} x - y &= 0 \\ rx - y - xz &= 0 \\ xy - bz &= 0 \end{cases}. \quad (6.1.18)$$

Fixed points satisfy $x = y$, such that the two other equations become

$$\begin{cases} (r - 1)x - xz &= 0 \\ x^2 - bz &= 0 \end{cases}. \quad (6.1.19)$$

The origin is a fixed point for all values of the parameters. We find two other fixed points

$$C_{\pm} \equiv \left(\pm \sqrt{b(r - 1)}, \pm \sqrt{b(r - 1)}, r - 1 \right). \quad (6.1.20)$$

However, the fixed points C_{\pm} only exist for $r > 1$.

We now determine the stability of the fixed points. The Jacobian matrix of the Lorenz system is

$$J(x, y, z) = \begin{pmatrix} -\sigma & \sigma & 0 \\ r - z & -1 & -x \\ y & x & -b \end{pmatrix}. \quad (6.1.21)$$

Evaluating the Jacobian at the origin, we see that the z -component is decoupled. Indeed, the Jacobian matrix is decomposed into a 2×2 and 1×1 block form. Therefore, $\lambda_1 = -b$ is an eigenvalue with corresponding eigenvector $\mathbf{v} = (0, 0, 1)$ so that solutions die out exponentially fast along the z direction for all values of the parameters. Hence it is sufficient to determine the behaviour in the (x, y) -plane and consider the matrix

$$\begin{pmatrix} -\sigma & \sigma \\ r & -1 \end{pmatrix} \quad (6.1.22)$$

for this two component system. This matrix has trace $-\sigma - 1$ and determinant $\sigma(1 - r)$. It is immediately clear that the origin becomes a saddle node if $r > 1$, because then the determinant is negative. For $r < 1$, the fixed point is stable, since $(\sigma - 1)^2 + 4\sigma r$ is greater than zero. At $r = 1$, there is a bifurcation which creates the C_{\pm} fixed points.

Let $r > 1$ such that the fixed points C_{\pm} exist. Evaluating the Jacobian at these fixed points, we find

$$J(C_{\pm}) = \begin{pmatrix} -\sigma & \sigma & 0 \\ 1 & -1 & \mp\Phi \\ \pm\Phi & \pm\Phi & -b \end{pmatrix}. \quad (6.1.23)$$

where we have defined $\Phi = \sqrt{b(r - 1)}$. To find the eigenvalues, we compute the characteristic equation $\det(J(C_{\pm}) - \lambda) = 0$. This gives

$$\lambda^3 + (\sigma + b + 1)\lambda^2 + b(\sigma + r)\lambda + 2b\sigma(r - 1) = 0 \quad (6.1.24)$$

Note that the characteristic equation is identical for C_{\pm} and hence the eigenvalues and -vectors are identical for the two fixed points. This is due to the fact that the operation $(x, y) \rightarrow (-x, -y)$ is a symmetry of the Lorenz equations. Since the characteristic equation for C_{\pm} is harder to solve analytically, we solve it numerically using Sympy (with $b = 8/3$ and $\sigma = 10$ as mentioned before). Figure 6.1.1 below shows the roots of the characteristic equation for the range $1.4 \leq r \leq 27$. We see that there is one real eigenvalue, which is always negative for all values of r , and there is a pair of complex conjugated eigenvalues. For most values of r in the above range, the pair has a negative real part, but close to $r = 27$, the eigenvalues cross the imaginary axis. Hence we conclude that there exists a value of r (denoted as r_H) such that for $1 < r < r_H$, the fixed points C_{\pm} are stable, while they become unstable for $r > r_H$. In other words, there is a Hopf bifurcation at $r = r_H$.

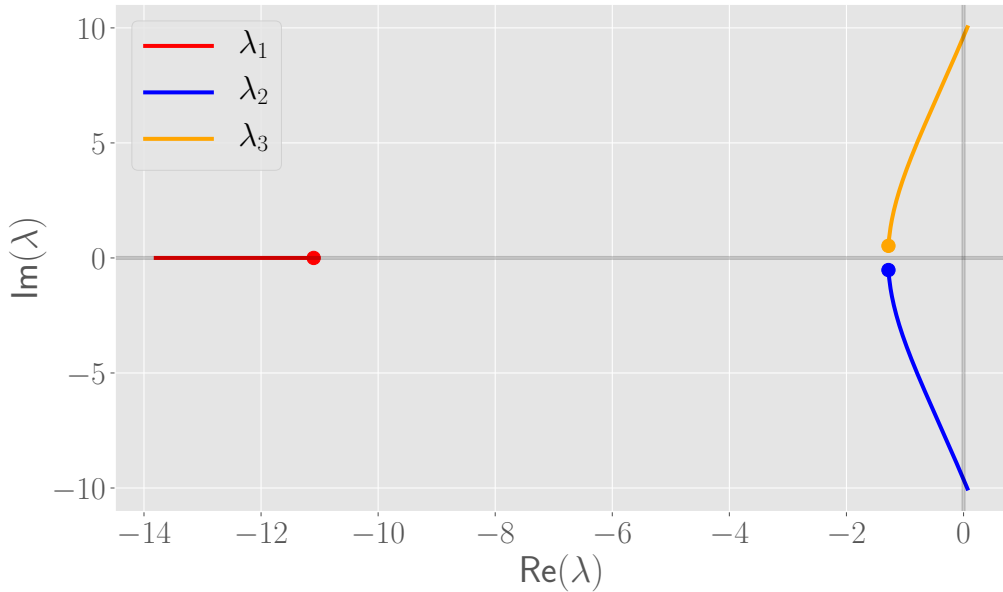


Figure 6.1.1: Complex eigenvalues of the Jacobian matrix evaluated at the fixed points C_{\pm} , for $1.4 \leq r \leq 27$. The coloured dots denote the eigenvalues for the lowest value of r .

6.1.3 Hopf bifurcation

Now we want to determine the value of r_H analytically, for general parameters b and σ . Recall that a Hopf bifurcation occurs when a pair of eigenvalues crosses the imaginary axis. Therefore, these eigenvalues should be of the form $\lambda = i\omega$ with $\omega \in \mathbb{R}$. We substitute this in the characteristic equation, and find

$$-\omega^3 - (\sigma + b + 1)\omega^2 + b(\sigma + r)i\omega + 2b\sigma(r - 1) = 0. \quad (6.1.25)$$

Now separate this into a real and an imaginary part, and require that both are equal to zero. This gives

$$\begin{cases} -(\sigma + b + 1)\omega^2 + 2b\sigma(r - 1) = 0 \\ b(\sigma + r)\omega - \omega^3 = 0 \end{cases}. \quad (6.1.26)$$

Since $\omega \neq 0$, we can divide by ω in the second equation. If we combine both equations, we find

$$-b(\sigma + b + 1)(\sigma + r) + 2b\sigma(r - 1) = 0. \quad (6.1.27)$$

We solve this equation for r , which gives

$$r_H = \frac{\sigma(\sigma + b + 3)}{\sigma - b - 1}. \quad (6.1.28)$$

Note that we have to require that $\sigma > b + 1$ such that $r_H > 0$. For the choice of parameters used in Figure 6.1.1 above, we find $r_H \approx 24.7368$. This agrees with the observations made from Figure 6.1.1.

6.2 The Rössler system

The Rössler system, with parameters a, b and c , is given by

$$\dot{x} = -y - z \quad (6.2.1)$$

$$\dot{y} = x + ay \quad (6.2.2)$$

$$\dot{z} = b + z(x - c). \quad (6.2.3)$$

This system has only one non-linear term, whereas the Lorenz equations have two non-linearities. Below, we will fix $a = b = 0.2$ and vary the parameter c .

6.2.1 Numerical exploration and orbit diagram

We start by numerically exploring the dynamics of the Rössler system. It will turn out that the Rössler system has interesting dynamics for $3.8 \leq c \leq 6$, so we will focus on this range for c .

In Figure 6.2.1 below, we plot projections in the (x, y) -plane of solutions to the Rössler system for a few values of c in this range. At low values of c , the system has periodic solutions, of which the period seems to double for increasing values of c . Around $c = 4.3$ until $c = 5.2$, the system seems to behave as a chaotic attractor, although it is difficult to conclude whether the system is indeed chaotic or is still periodic with a very large period. For $c = 5.5$, the system tends to periodic behaviour again, but the convergence to the attractor is very slow compared to the first two values of c . This is likely because the system is close to a bifurcation. Indeed, at $c = 5.7$, the solution seems to tend to a chaotic attractor again. For $c = 6$, the solutions are again periodic.

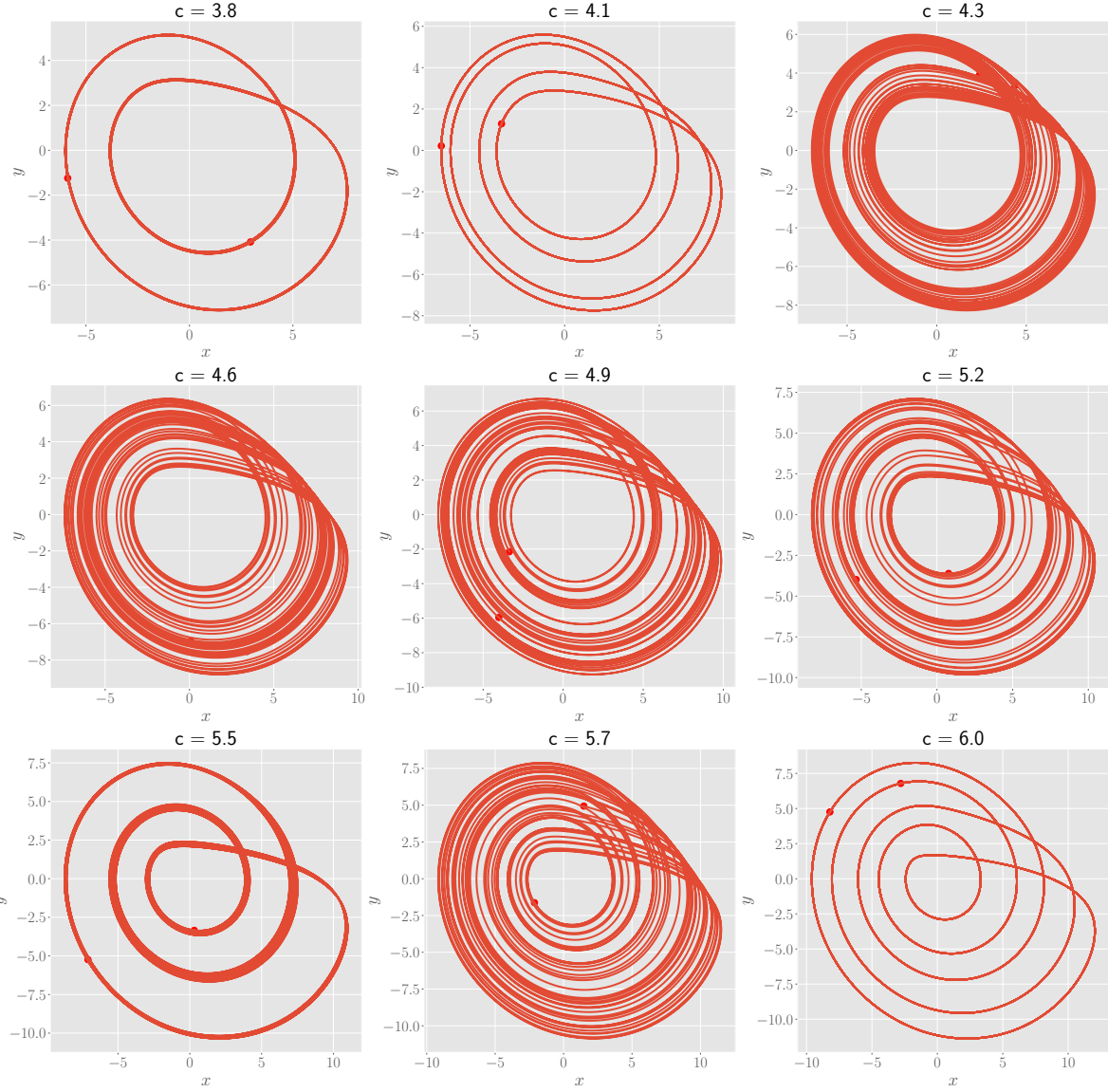


Figure 6.2.1: Projections on the (x, y) -plane of solutions to the Rössler system, after a transient phase. Dots denote the start and end points of a solution.

The above considerations are verified by looking at a time series. In particular, we look at the sequence of maxima of x in the time series. This is shown in Figure 6.2.2 below, and agrees with the discussion of the previous figure.

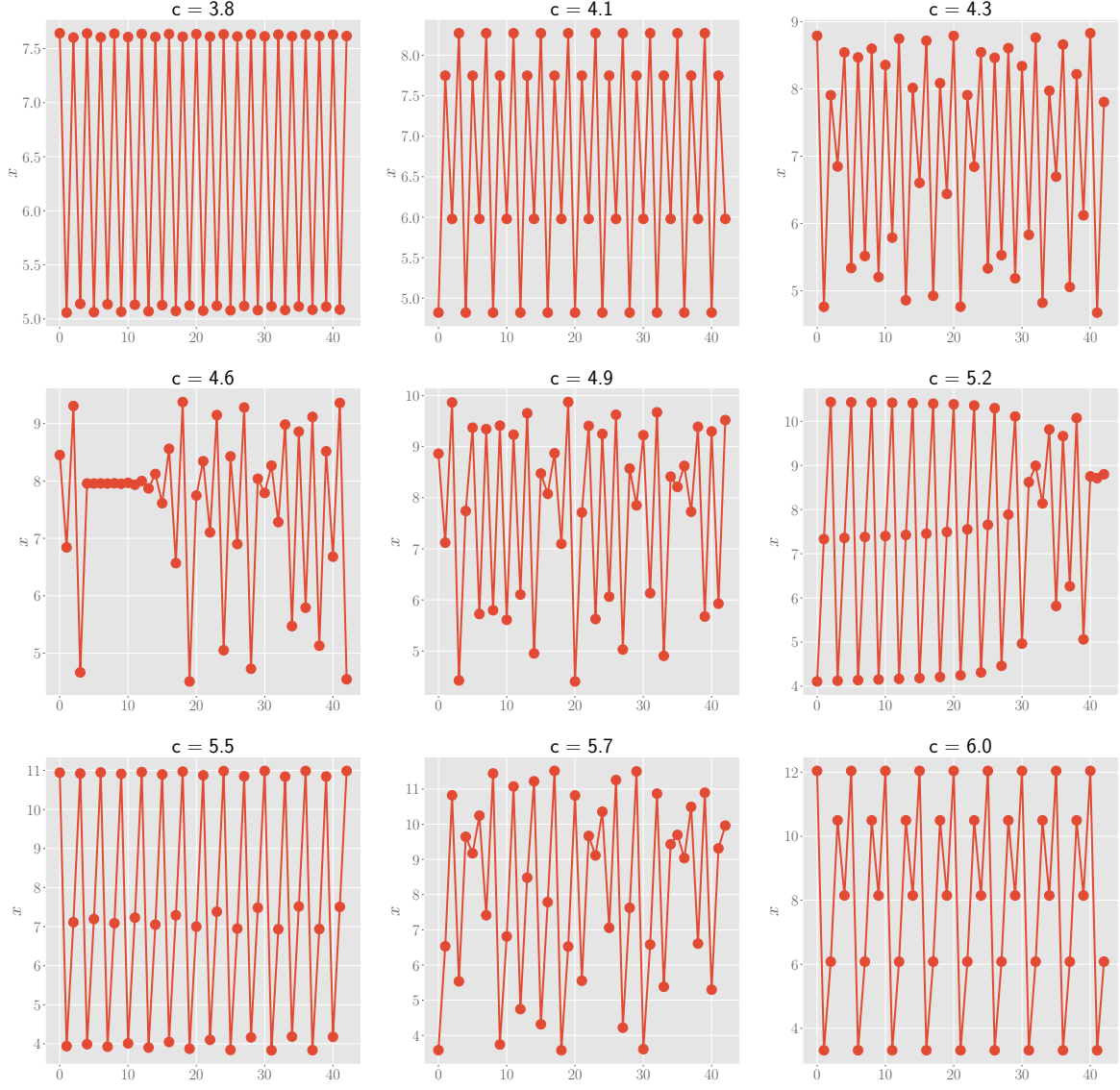


Figure 6.2.2: Maxima of x of solutions shown in Figure 6.2.1.

Finally, we plot the orbit diagram for the Rössler system in Figure 6.2.3 below. The orbit diagram offers a way to summarise the behaviour of a system as a function of a parameter in a single plot. From the figure, we see that the system indeed undergoes a period-doubling cascade to chaos, after which it becomes periodic again before a new sequence of bifurcations occur. The orbit diagram shown below is in fact very similar to the orbit diagrams of the logistic and sine maps, given in the next sections.

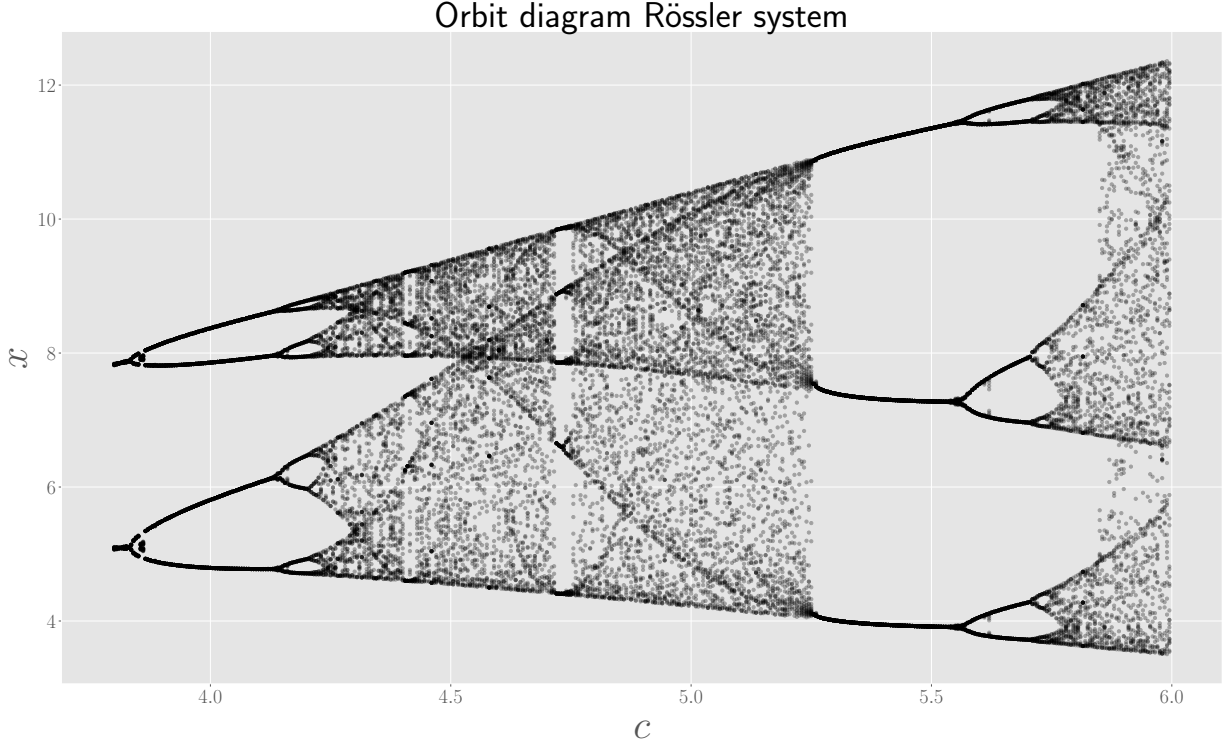


Figure 6.2.3: Orbit diagram of the Rössler system for $3.8 \leq c \leq 6$.

6.2.2 Fixed points and stability

We look for the fixed points of the Rössler system, which are solutions of the equations

$$\begin{cases} y + z &= 0 \\ x + ay &= 0 \\ b + z(x - c) &= 0. \end{cases} \quad (6.2.4)$$

From the first two equations, we find $y = -z$ and $x = -ay = az$, such that z has to be a solution of

$$az^2 - cz + b = 0. \quad (6.2.5)$$

There are two fixed points, given by

$$C_+ = \left(\frac{c + \sqrt{c^2 - 4ab}}{2}, -\frac{c + \sqrt{c^2 - 4ab}}{2a}, \frac{c + \sqrt{c^2 - 4ab}}{2a} \right) \quad (6.2.6)$$

$$C_- = \left(\frac{c - \sqrt{c^2 - 4ab}}{2}, -\frac{c - \sqrt{c^2 - 4ab}}{2a}, \frac{c - \sqrt{c^2 - 4ab}}{2a} \right). \quad (6.2.7)$$

Note that the fixed points exist only if $c^2 > 4ab$. The Jacobian matrix of the Rössler system is

$$J(x, y, z) = \begin{pmatrix} 0 & -1 & -1 \\ 1 & a & 0 \\ z & 0 & x - c \end{pmatrix}, \quad (6.2.8)$$

such that the characteristic equation $\det(J - \lambda) = 0$ becomes

$$-\lambda^3 + (x - c + a)\lambda^2 + (-ax - z - 1 + ac)\lambda + az + x - c = 0. \quad (6.2.9)$$

Note that, contrary to the Lorenz system, the characteristic equation will be different for the two fixed points. We will again solve this equation numerically using Sympy for $a = 0.2 = b$ and $0.5 \leq c \leq 6$.

For the fixed point C_+ , the solutions to the characteristic equation are shown in Figure 6.2.4 below. If we zoom in on the complex conjugated pair of eigenvalues, we see that they have a negative real part for all values of c considered. Since there is one eigenvalue with positive real part, the fixed point C_+ is unstable.

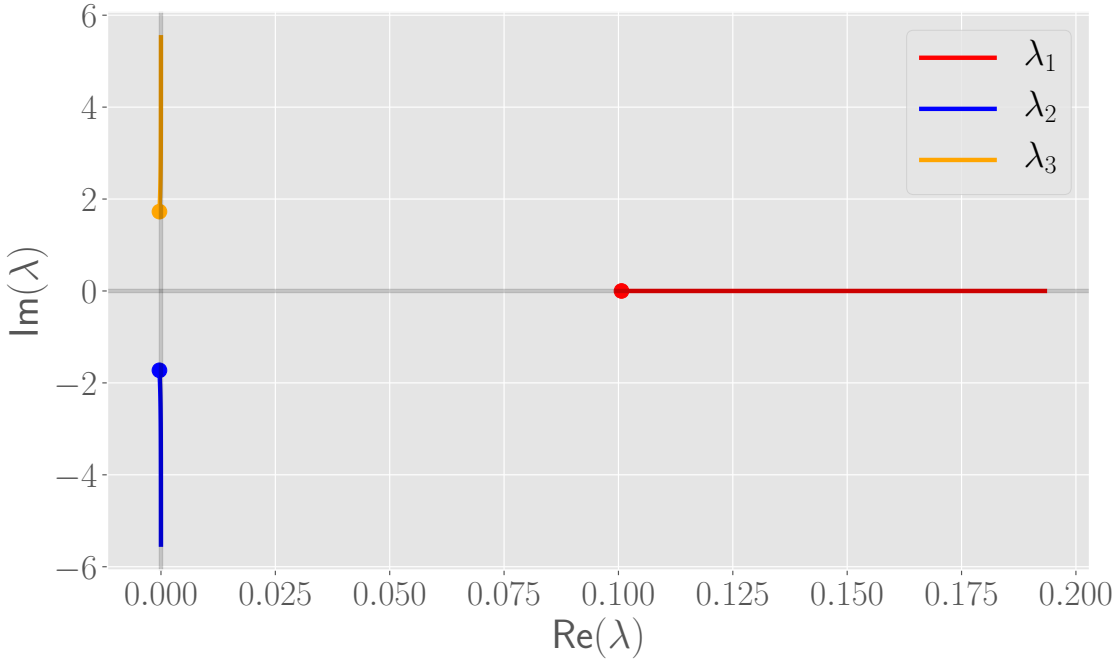


Figure 6.2.4: Solutions of characteristic equation for C_+ in the complex plane. The dots denote the first value of c considered.

For the fixed point C_- , the solutions to the characteristic equation are shown in Figure 6.2.5 below. If we zoom in on the complex conjugated pair, we see that they have positive real part for all values of c considered. Hence the fixed point C_- is unstable as well.

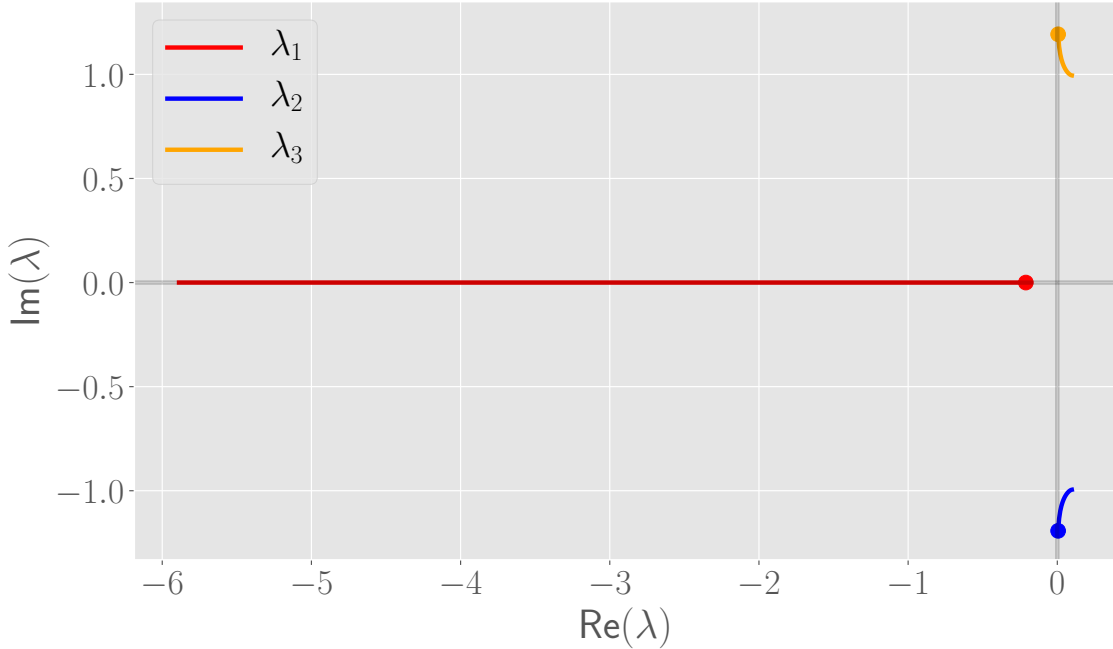


Figure 6.2.5: Solutions of characteristic equation for C_- in the complex plane. The dots denote the first value of c considered.

6.2.3 1D map for the Rössler system

To understand chaos in the Lorenz system, it was useful to plot z_{n+1} (the $(n+1)$ -th maximum in z) as a function of z_n . We do something similar for the Rössler map, where we plot the maxima of x instead of z . This is shown in Figure 6.2.6 below. The curve is thin, as was the case for the Lorenz map, and also seems to be unimodal, which will be defined in the next section. In fact, it is very similar to the logistic map. As discussed later, if the right conditions are fulfilled, unimodality of a 1D map leads to the period-doubling cascade to chaos observed in the numerical explorations and orbit diagram above. Hence we conclude that the Rössler and Lorenz systems both exhibit a similar route to chaos, and in both cases, this can be understood from their discrete 1D maps.

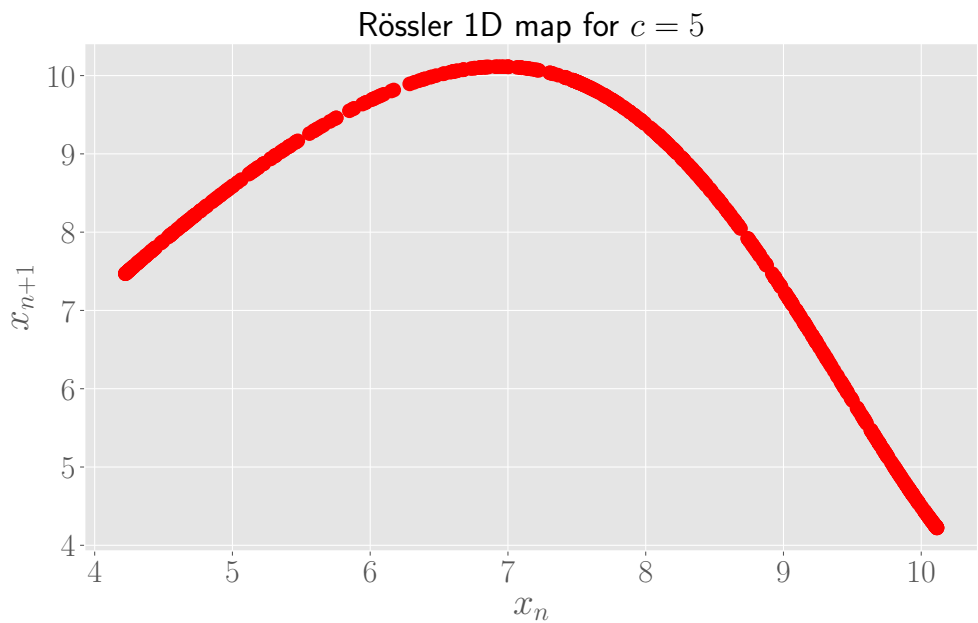


Figure 6.2.6: The curve corresponding to the 1D map related to the Rössler system with $c = 5$. The curve is very thin, as was the case for the Lorenz map, and is unimodal.

6.3 The logistic map

The previous section and our study of the Lorenz system showed that 1D maps are a useful tool to understand chaotic dynamics. Therefore, we will now study a well-known example of such a 1D map, namely the logistic map, given by

$$x_{n+1} = rx_n(1 - x_n) \equiv f_r(x_n), \quad (6.3.1)$$

where we take $x_0 \in [0, 1]$ such that $x_n \in [0, 1]$ for all n , and restrict the parameter r to $0 \leq r \leq 4$. We start by determining the fixed points of the map, which satisfy $f_r(x^*) = x^*$. These are solutions of the equation

$$x = rx(1 - x). \quad (6.3.2)$$

The first solution is the origin, which is a fixed point for all values of r . A second solution is

$$x^* \equiv 1 - \frac{1}{r}, \quad (6.3.3)$$

but since we restrict the domain to the unit interval, this fixed point is only present if $r \geq 1$. The stability of fixed points of discrete maps is determined by the multiplier $\lambda \equiv f'(x^*)$: a fixed point is stable if $|\lambda| < 1$ and unstable if $|\lambda| > 1$, with $|\lambda| = 1$ corresponding to a marginal case for which cobweb diagrams must be used to determine the stability. We have

$$f'_r(x) = r - 2rx. \quad (6.3.4)$$

The origin is stable if $r < 1$ but becomes unstable for $r > 1$. The non-zero fixed point (appearing if $r \geq 1$) has multiplier

$$f'_r(x^*) = r - 2r \left(1 - \frac{1}{r}\right) = 2 - r. \quad (6.3.5)$$

Hence x^* is stable for $-1 < 2 - r < 1$, so for $1 < r < 3$, but becomes unstable if $r > 3$. We conclude that at $r = 1$, there is a bifurcation where the origin passes its stability on to the fixed point x^* .

6.3.1 Behaviour of the dynamics as a function of r

For different values of r , the behaviour of the logistic map changes dramatically, ranging from periodic solutions to chaos. The stable fixed points and 2-cycles, appearing at lower values of r , can be determined analytically³. For cycles with a larger period and the cascade into chaos, we study the logistic map numerically.

³These analytic calculations are inspired by Chapter 10 of Strogatz [5].

Stable fixed points and 2-cycles: analytic calculation Because of our earlier considerations, we know that for $r < 3$, the solutions will tend towards a stable steady state (which is the origin for $r < 1$ and the point x^* for $r > 1$). We verify this numerically as follows. We sweep the values of r between 1 and 3 (with a separation of 0.01 between successive values of r), and for each value of r generate a time series of length 600, starting from a certain set of initial conditions (excluding 0 and 1 since they both map to 0 and remain there). After the iterations are done, we check if the separation between the last value of the iteration and the stable fixed point is greater than a certain threshold ϵ , in the code taken to be 10^{-4} . If this is indeed the case, then we print this observation. If we run the code, there is no output, meaning that all time series eventually approach the fixed points. Note that if the precision is increased to $\epsilon = 10^{-5}$, then the output prints that there is no convergence towards the fixed point for $r = 0.99, 1.01$ and $r = 2.99$. Hence if we are closer to the boundary values of r for which the fixed points are stable, the convergence is slower, as we expect.

However, the stability analysis using the multiplier of a map is inconclusive for $r = 1$ and we have to rely on a numerical computation. Figure 6.3.1 below shows the cobweb diagrams for a few initial conditions. The origin is still a stable fixed point, but the convergence towards the origin is slow if $x \approx 0$.

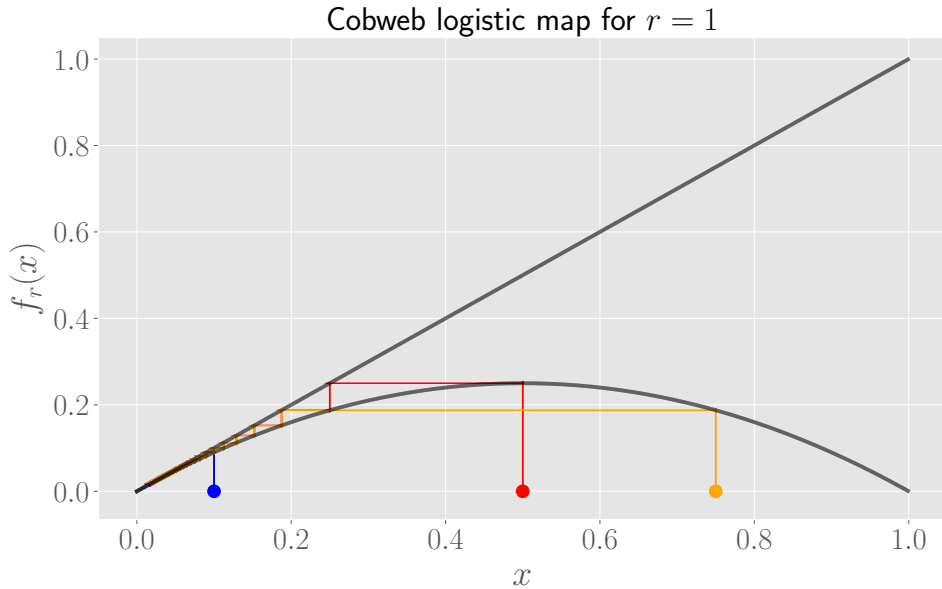


Figure 6.3.1: Cobweb diagrams for the logistic map with $r = 1$, for a few initial conditions. The origin is stable for $r = 1$, but the convergence is slow if x is small.

If r is slightly larger than 3, stable 2-cycles appear, as we now prove analytically. A stable 2-cycle means that there exist two points p and q such that $f(p) = q$ and $f(q) = p$. Therefore, we have $f(f(p)) = p$ and $f(f(q)) = q$, or equivalently, p and q are fixed points of

the second-iterate map f^2 . From the definition of the logistic map, we find

$$f_r^2(x) = r(rx(1-x))(1-rx(1-x)). \quad (6.3.6)$$

If we look for the fixed points of this map, then these have to be solutions of the equation $f_r^2(x) = x$, which can be rewritten as

$$x(-r^3x^3 + 2r^3x^2 - (r^3 + r^2)x + r^2 - 1) = 0. \quad (6.3.7)$$

This fourth order polynomial will have four different solutions. Two solutions will be the fixed points of the logistic map. Indeed, since they satisfy $f_r(x) = x$, they will also satisfy $f_r^2(x) = x$. It is already clear that $x = 0$ is a solution of the above equation. We use the other fixed point $x^* = 1 - 1/r$ to factorise the polynomial, and we find the equivalent equation

$$x \left[x - \left(1 - \frac{1}{r} \right) \right] \left[x^2 - \left(1 + \frac{1}{r} \right) x + \frac{1}{r} \left(1 + \frac{1}{r} \right) \right] = 0. \quad (6.3.8)$$

The solutions of the remaining quadratic equation will yield the points p and q mentioned earlier. After some straightforward algebraic manipulations, we find that these solutions are

$$p, q = \frac{1}{2} \left[\left(1 + \frac{1}{r} \right) \pm \frac{1}{r} \sqrt{(r-3)(r-1)} \right]. \quad (6.3.9)$$

Since these solutions have to be real numbers, we have to require that $r > 3$. At $r = 3$, the two roots coincide and are equal to $x^* = 1 - 1/r = 2/3$. So at $r = 3$, the fixed point x^* bifurcates into a 2-cycle.

To determine if the two-cycle is stable, we compute the multiplier of the second-iterate map f_r^2 . If we compute this for the fixed point p , we find

$$\lambda = \frac{d}{dx} f_r(f_r(p)) = f'_r(f_r(p))f'_r(p) = f'_r(q)f'_r(p), \quad (6.3.10)$$

where we used that $f_r(p) = q$ by definition of the 2-cycle. We obtain the same result if we compute the multiplier for q . Using the explicit expressions for p and q , we compute

$$\begin{aligned} \lambda &= r(1-2q)r(1-2p) \\ &= r^2(1-2(p+q)+4pq) \\ &= 4+2r-r^2. \end{aligned} \quad (6.3.11)$$

The 2-cycles are stable if $|4+2r-r^2| < 1$ and $r > 3$, which gives the range $3 < r < 1 + \sqrt{6}$.

We verify this numerically by plotting a cobweb diagram, shown in Figure 6.3.2, and a time series, shown in Figure 6.3.3, for a value of r in this range, say $r = 3.25$. The initial condition of the plots is $x_0 = 0.4$ (from now on, all numerical solutions have this as initial condition).

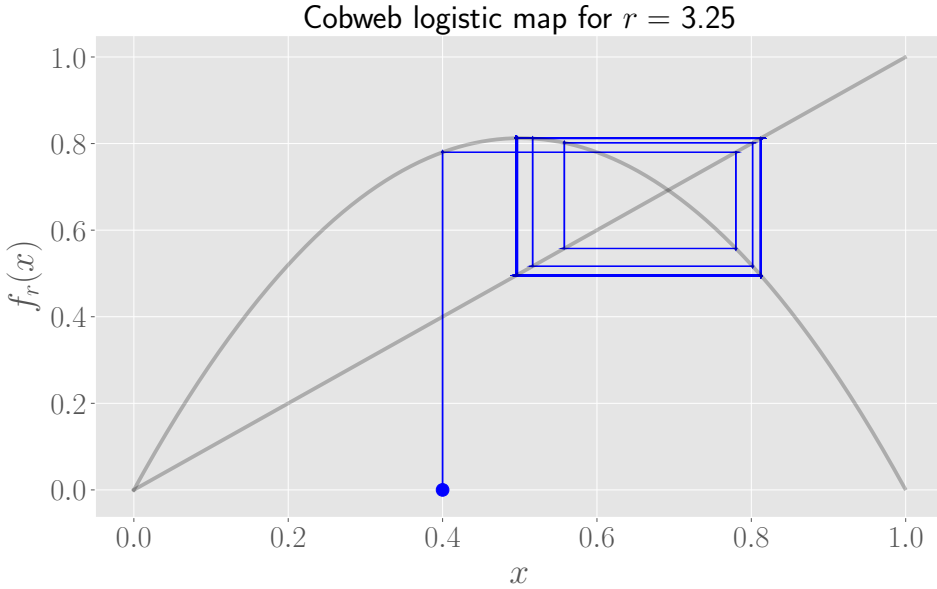


Figure 6.3.2: Cobweb diagram of logistic map for $r = 3.25$, showing a stable 2-cycle.

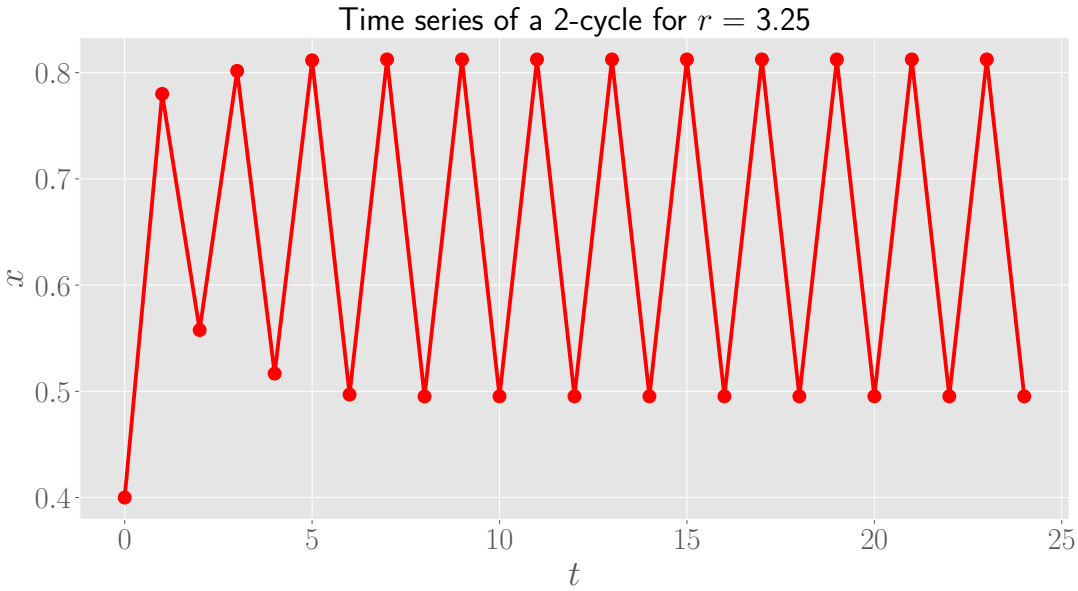


Figure 6.3.3: Cobweb diagram of logistic map for $r = 3.25$, showing a stable 2-cycle.

Period-doublings: numerical study In the previous subsection, we were able to determine analytically the appearance and stability of fixed points (for $r < 3$) and stable 2-cycles (for $3 < r < 1 + \sqrt{6}$). The calculations can be extended towards cycles with a larger period. However, it is immediately clear that the calculations become quite complicated, which is why we will only numerically study the dynamics for $r > 1 + \sqrt{6}$. As mentioned in

Strogatz [5, p.355], we have further period-doublings to cycles of period 4, 8, 16, ... Let r_n denote the value of r where the 2^n -cycle appears. Then numerical studies (for example, by looking at the orbit diagram, which we will discuss later on) reveal that

$$\begin{aligned} r_1 &= 3 \\ r_2 &= 3.449\dots \\ r_3 &= 3.54409\dots \\ r_4 &= 3.5644\dots \\ r_5 &= 3.568759\dots \\ &\vdots \\ r_\infty &= 3.569946\dots, \end{aligned}$$

where r_∞ is the limit value of r_n . The *Feigenbaum constant* is defined by

$$\delta = \lim_{n \rightarrow +\infty} \frac{r_n - r_{n-1}}{r_{n+1} - r_n} = 4.669\dots \quad (6.3.12)$$

We numerically verify the above statements via cobweb diagrams and time series. In Figure 6.3.4 below, we plot cobweb diagrams for values of r after which an additional period doubling has occurred. To make the plots easier to interpret, we discard the first half of the numerically obtained solutions, such that a transient phase has passed and the solutions are close to the attractor. The period of the cycle is found by counting the number of times the cobweb crosses the $y = x$ curve. For each solution shown in 6.3.4, we show a piece of the corresponding time series in Figure 6.3.5, from which we can also deduce the period.

Period doubling in cobweb diagrams

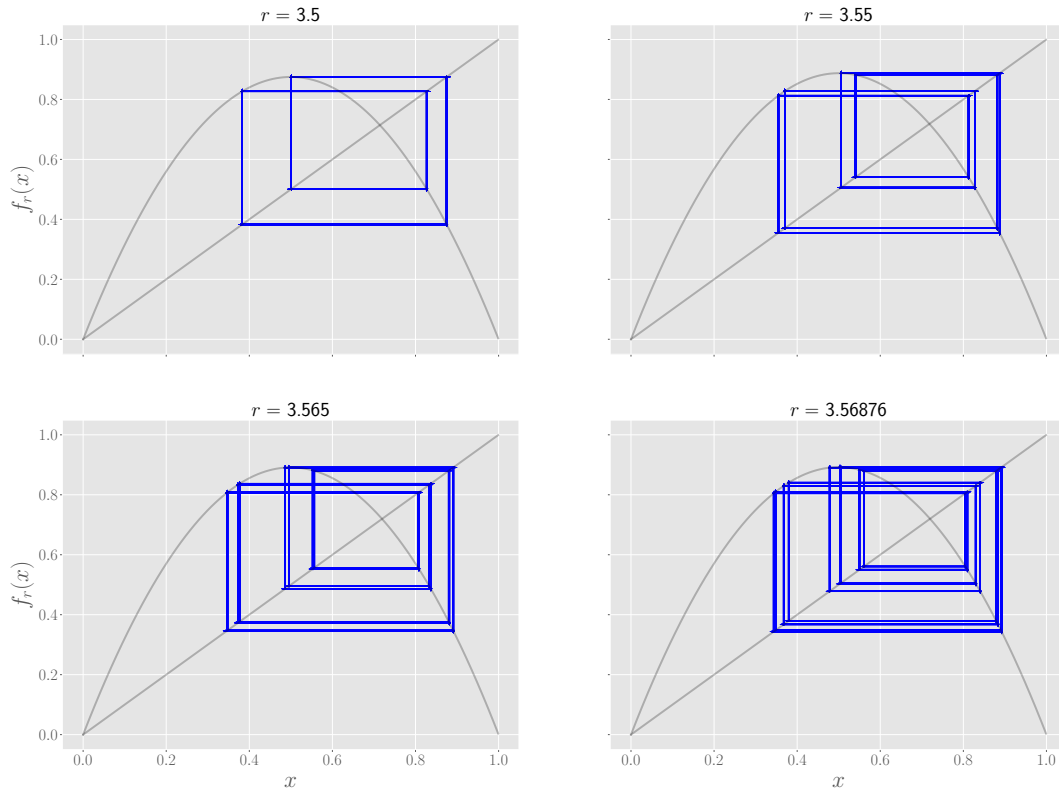


Figure 6.3.4: Cobweb diagrams showing the period-doubling of the logistic map. The solutions shown are after a transient phase has passed.

Period doubling in time series

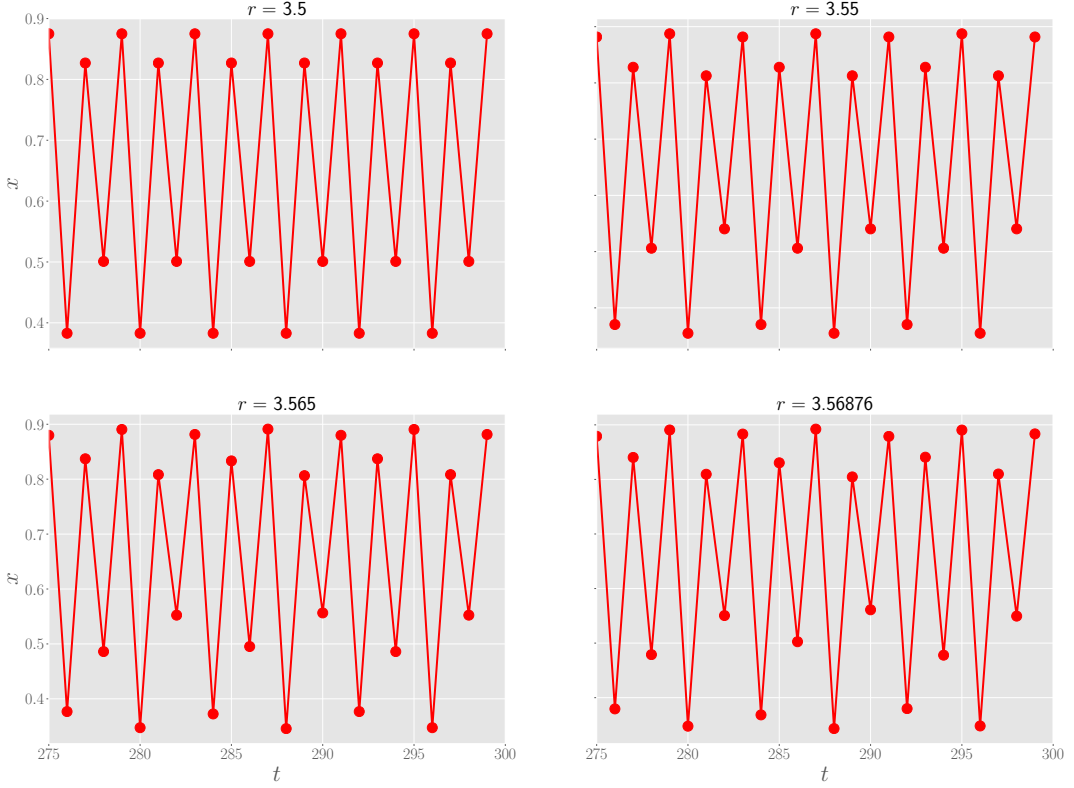


Figure 6.3.5: A part of the time series corresponding to the solutions shown in Figure 6.3.4.

Chaos What happens above the value r_∞ ? The dynamics become chaotic, but there do exist ‘windows’ of periodic behaviour (see the orbit diagram later on). We will check this for the particular value $r = 3.9$.

Recall the definition of chaos as given by Strogatz: *chaos is aperiodic long-time behaviour in a deterministic system that exhibits sensitive dependence on initial conditions*. While it is not a rigorous argument, we verify that the long-time behaviour is aperiodic by looking at the cobweb diagram or the time series. These are given in Figure 6.3.6 and Figure 6.3.7, respectively.

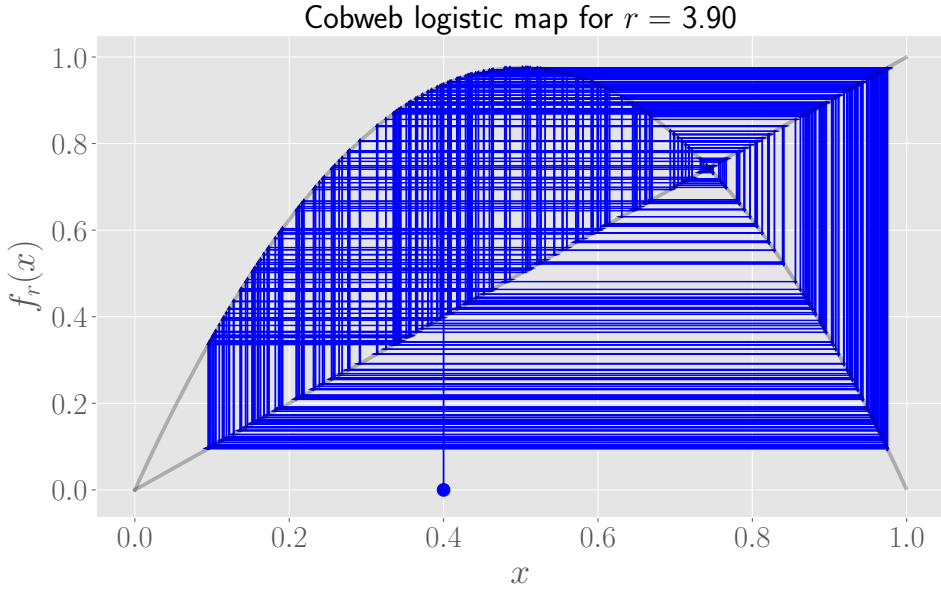


Figure 6.3.6: Cobweb diagram of logistic map for $r = 3.9$, showing aperiodic long-time behaviour.

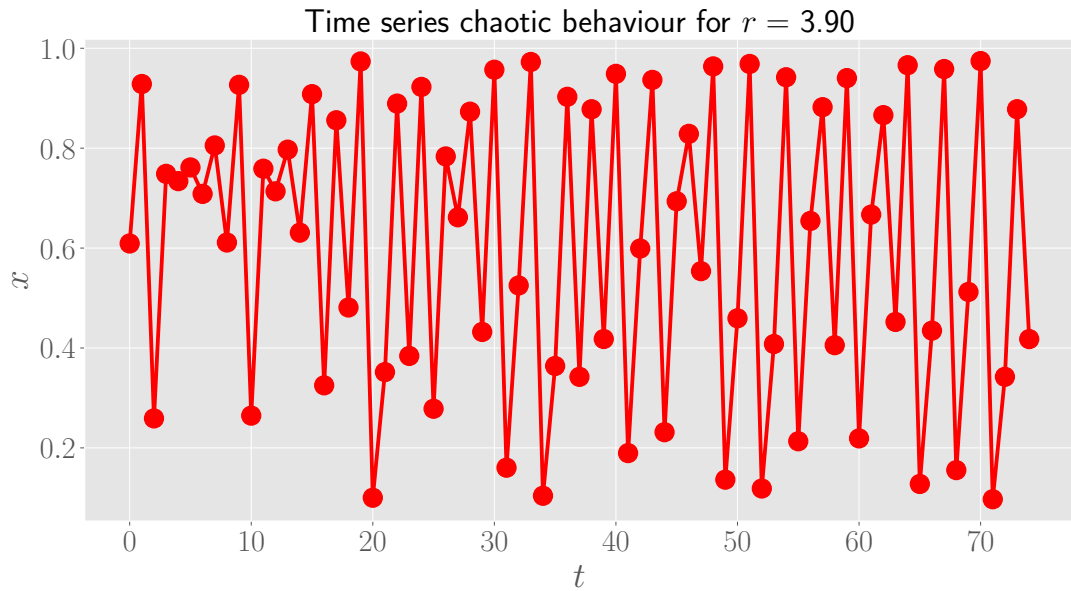


Figure 6.3.7: A part of the time series corresponding to the solution shown in Figure 6.3.6.

To determine if the system has sensitive dependence on initial conditions, we check if the Lyapunov exponent is positive for $r = 3.9$. Strogatz derives the following expression for the

Lyapunov exponent⁴ μ of a 1D map f

$$\mu = \lim_{n \rightarrow +\infty} \left(\frac{1}{n} \sum_{i=0}^{n-1} \ln |f'(x_i)| \right). \quad (6.3.13)$$

We estimate this numerically by truncating the series at a large value for n . In Figure 6.3.8 below, we plot the Lyapunov exponent for $r \geq 3.5$. As expected, the Lyapunov exponent becomes positive for r values in this range. However, the Lyapunov exponent occasionally goes down in a dip and becomes negative again. These correspond for instance to the periodic windows, which we will discuss next. Finally, note that μ is positive for $r = 3.9$, so the logistic map is indeed sensitive to initial conditions. We conclude the logistic map is chaotic for this value of r .

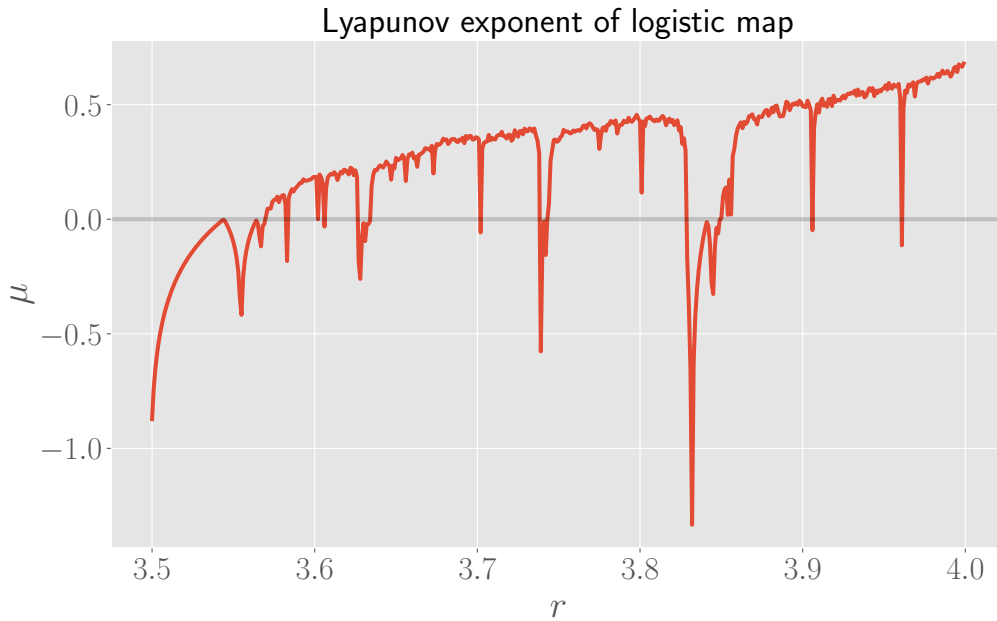


Figure 6.3.8: Lyapunov exponent of the logistic map for the range $r \geq 3.5$, where we expect to see chaotic behaviour (positive Lyapunov exponent).

6.3.2 Orbit diagram

Finally, we plot the orbit diagram of the logistic map. For this, we sweep a range of values for the parameter r with a given separation⁵ Δr (which acts as a kind of ‘resolution’) between

⁴Strogatz denotes the Lyapunov exponent by λ , but since this symbol is also used for the multiplier of a map, we will use μ instead.

⁵We can produce more beautiful orbit diagrams with a much better resolution in the notebook. Unfortunately, we can not give them in this report. The reason is that if the size of the plots becomes too large, this can apparently cause memory errors and crashes in a L^AT_EX-editor, as we discovered the hard way.

adjacent r -values. For each r , we plot points obtained by the iteration after a transient phase has passed, such that the solution lies on the attractor. We restrict our attention to $r > 1 + \sqrt{6}$, since the dynamics becomes interesting at this point and we have analytic results for $r < 1 + \sqrt{6}$. The orbit diagram is shown in Figure 6.3.9 and summarises the above discussion in one figure. The orbit diagram can also be used to estimate the values r_n , and hence the Feigenbaum constant. In fact, this is precisely what we will do with the orbit diagram of the sine map in the next section.

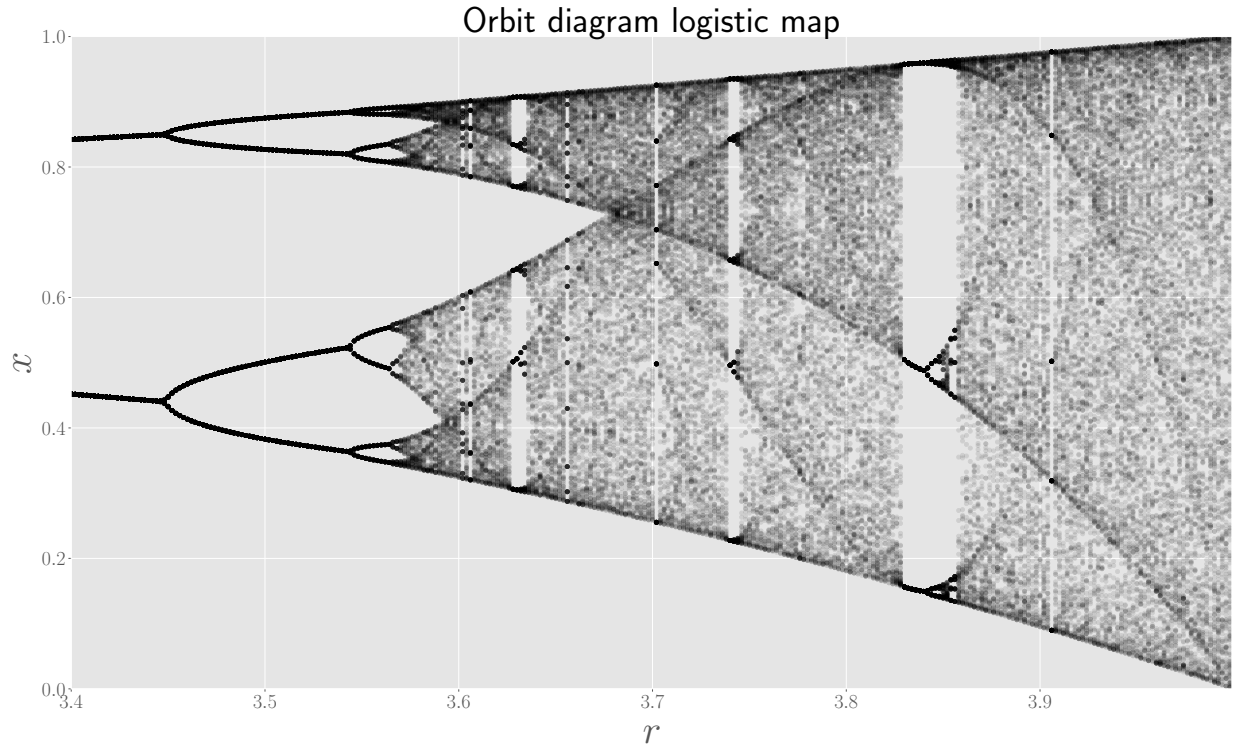


Figure 6.3.9: Orbit diagram of the logistic map.

6.4 The sine and tent map

In this section, we will study two other one-dimensional maps and compare it with the logistic map, which was extensively studied above. First, we will consider the sine map, given by

$$x_{n+1} = r \sin(\pi x_n), \quad (6.4.1)$$

with r between 0 and 1 and $x_n \in [0, 1]$. Next, we consider the tent map, given by

$$x_{n+1} = \begin{cases} rx_n & \text{for } x_n \in [0, \frac{1}{2}] \\ r(1 - x_n) & \text{for } x_n \in [\frac{1}{2}, 1] \end{cases}, \quad (6.4.2)$$

with r between 0 and 2.

6.4.1 Orbit diagrams

In the previous section, we saw that the orbit diagram of a 1D map is a convenient way to summarise the behaviour of the dynamics for various values of the parameter r in a single figure. Therefore, we will construct the orbit diagrams for the sine and tent map as well. We first plot the orbit diagrams with a large Δr , to get an idea of where the maps have interesting dynamics. Next, we reconstruct the orbit diagram for a smaller range of the parameter r , and a higher resolution (smaller Δr).

In Figure 6.4.1 below, the first orbit diagram of the sine map is shown. A first bifurcation, where a stable fixed point bifurcates into a stable 2-cycle, is seen around $r \approx 0.7$. The interesting dynamics start to happen around $r \approx 0.82$. In Figure 6.4.2, we show the orbit diagram in higher resolution for the range $0.82 \leq r \leq 1$.

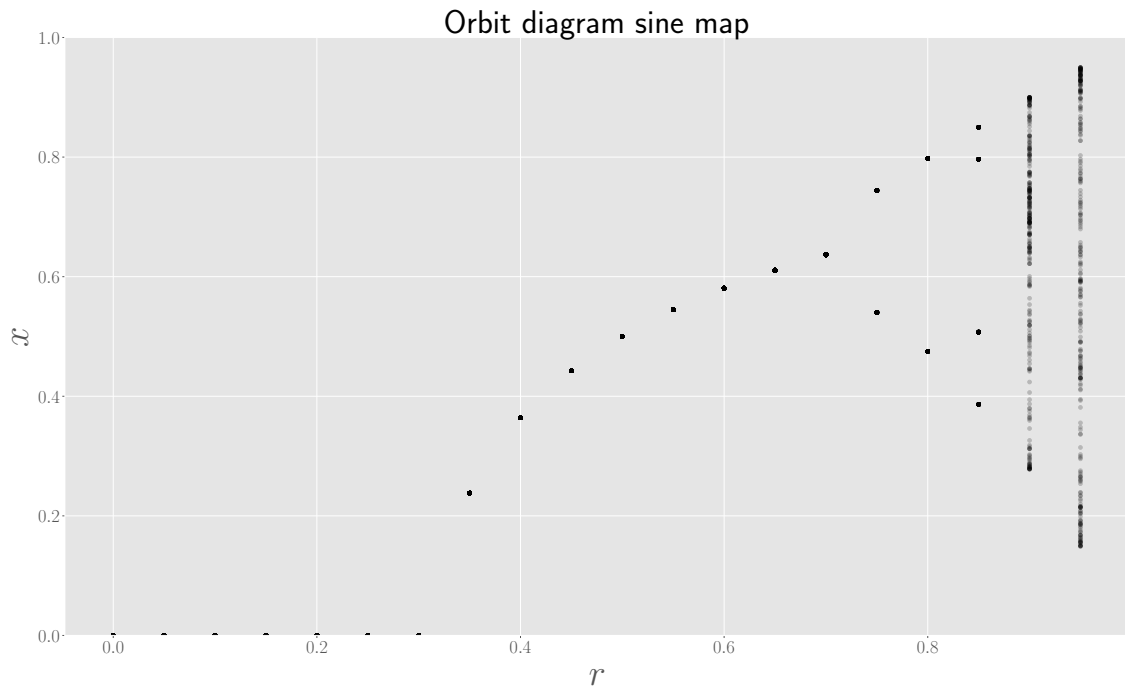


Figure 6.4.1: First orbit diagram for the sine map.

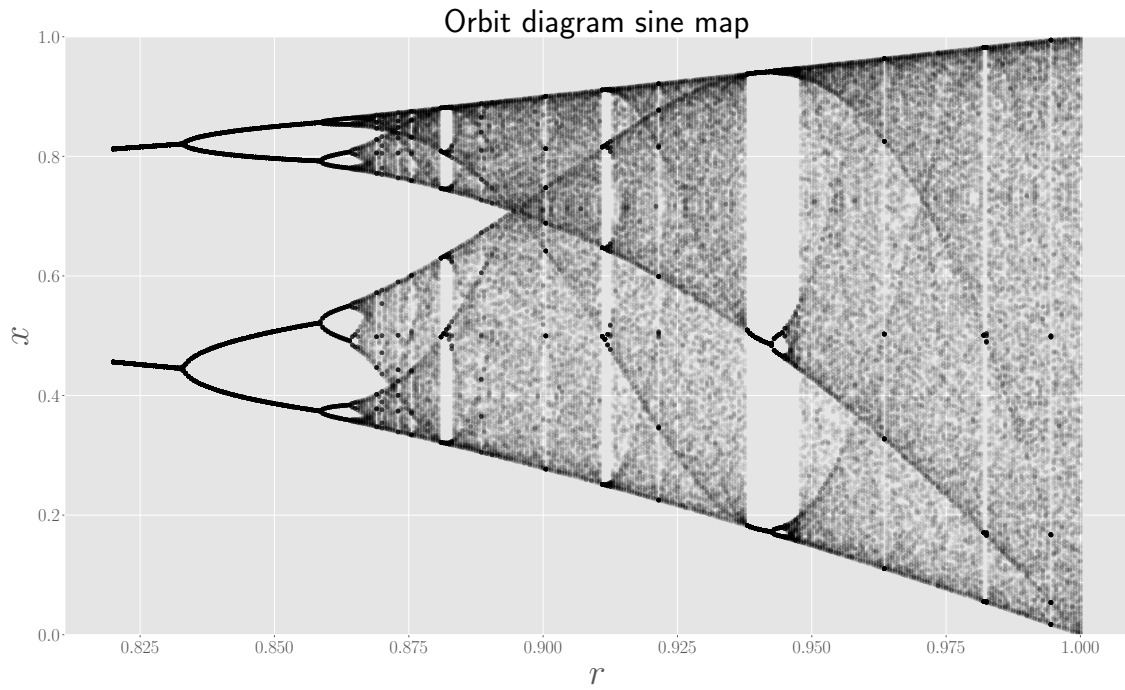


Figure 6.4.2: Second orbit diagram for the sine map.

The dynamics of the sine map become chaotic after $r \approx 0.82$. Indeed, the orbit diagrams show the solutions become aperiodic in their long-time behaviour. Figure 6.4.3 below also verifies that the Lyapunov exponent becomes positive. However, periodic windows cause dips in the Lyapunov spectrum.

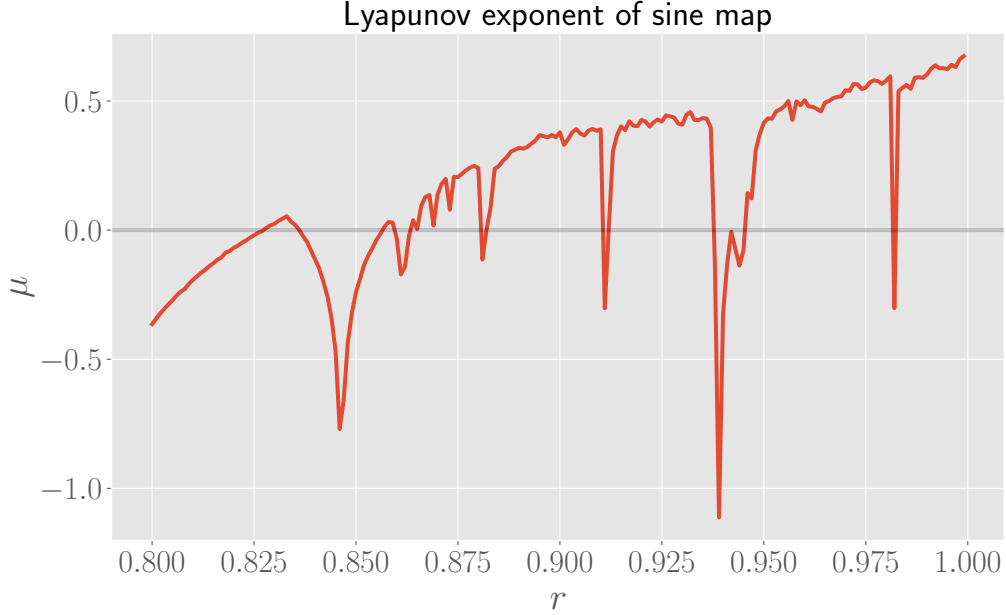


Figure 6.4.3: Lyapunov exponent of the sine map in the range of r -values for which we expect to see chaotic behaviour.

In Figure 6.4.4 below, the first orbit diagram of the tent map is shown. We see that the interesting dynamics start to happen at $r = 1$. In Figure 6.4.5, we show a more detailed orbit diagram in the range $1 \leq r \leq 2$. The tent map is aperiodic in this range, and even chaotic. Indeed, the Lyapunov exponent is easily computed analytically for this map, as done in example 10.5.2 in Strogatz, and results in $\mu = \ln r$, such that $\mu > 0$ for $r > 1$. There are no periodic windows, and the Lyapunov exponent remains positive throughout this range.

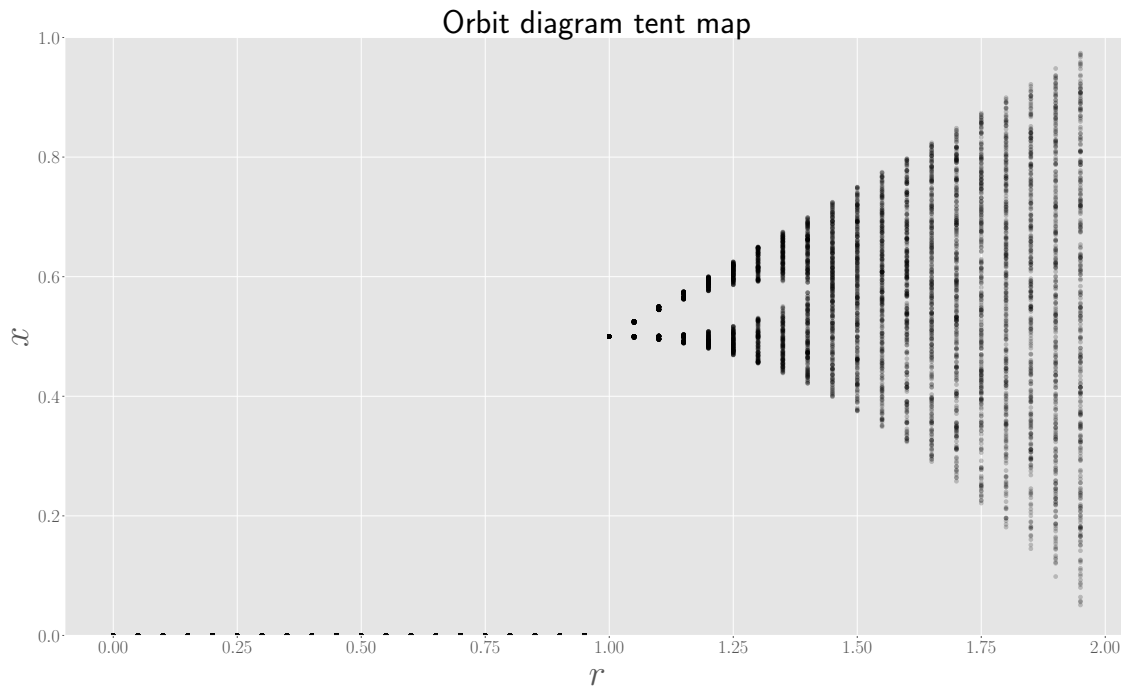


Figure 6.4.4: First orbit diagram for the tent map.

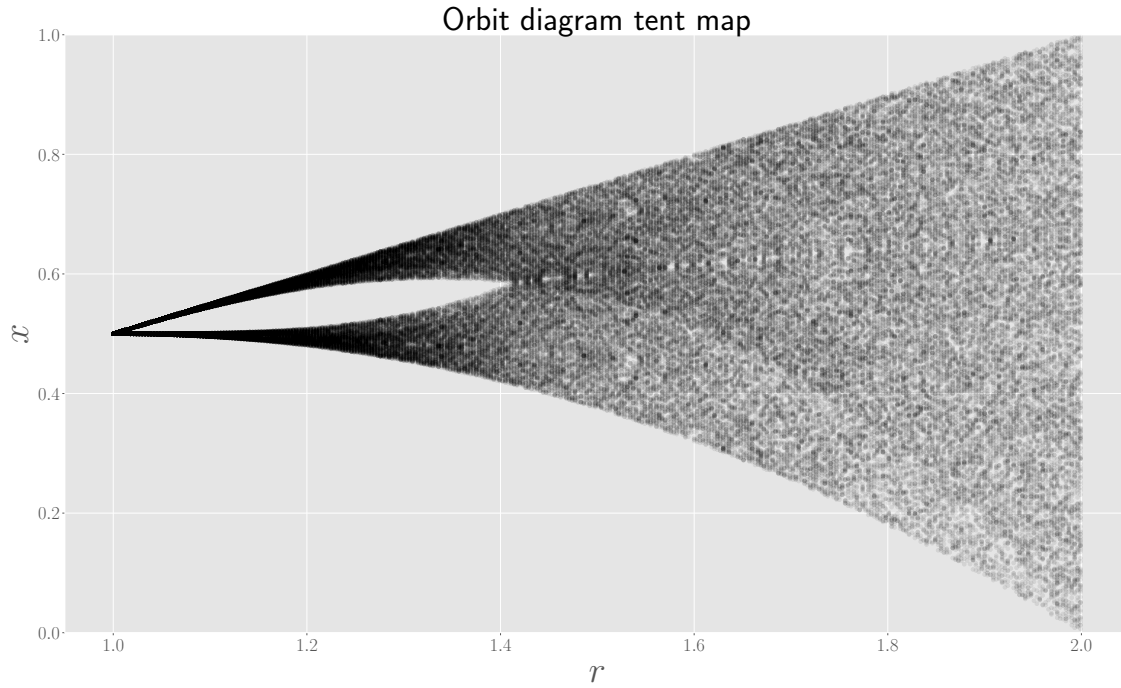


Figure 6.4.5: Second orbit diagram for the tent map.

6.4.2 Comparison with the logistic map

If we compare the above orbit diagrams with the orbit diagram of the logistic map, given in Figure 6.3.9, we see that the global shapes of the orbit diagrams of the sine and logistic map are nearly identical. Indeed, both display a period-doubling cascade to chaos, and after chaotic behaviour has been reached, both have periodic windows. On the contrary, the orbit diagram of the tent map looks very different. For instance, there is no period-doubling cascade to chaos and there are no periodic windows.

The fact that the sine and logistic map have very similar behaviour is called *universality*. We estimate the Feigenbaum constant for the sine map. For this, we estimate the r_n -values (values of r where the period doubles). These are $r = 0.72, 0.8333, 0.8586, 0.8641, 0.8653$. Hence we find $\delta \approx 4.5833$, which is fairly close to the exact value of the Feigenbaum constant given in the previous section. We conclude that the Feigenbaum constant is universal.

Why are the sine and the logistic map so similar, but is the tent map different from them? This is explained in a paper by Metropolis *et al.* (1973) [3]. The paper gives a number of conditions on a 1D map of the form $rf(x)$ defined on the unit interval which, if they are fulfilled, imply that the U-sequence (which determines the overall shape of the orbit diagram) is uniquely determined. Both the logistic and sine map satisfy these conditions. Such functions are called *unimodal*, since they are smooth, concave down and have a unique maximum, as seen in Figure 6.4.6. The tent map does not fulfill all of these conditions, such that it does not automatically⁶ have the same orbit diagram, as we observed above. Indeed, condition A.3 in [3] reads that at any x such that $f(x) = f_{\max}$, the derivative should exist and must be equal to zero. This is not satisfied for the tent map, since the derivative is not defined at $x = 1/2$.

⁶The phrasing is a bit weird since the conditions of Metropolis *et al.* are sufficient but not necessary, such that, based on this theorem, it is in principle possible that the tent diagram has the same U-sequence. The theorem shows the logistic and sine map have the same U-sequence, but we still have to verify explicitly that the tent map does share this U-sequence.

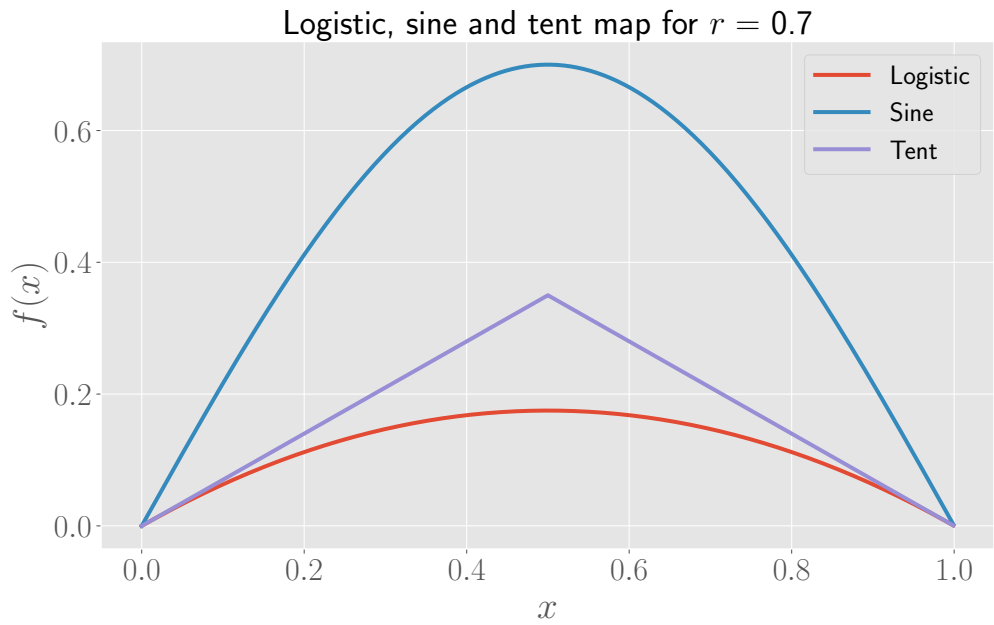


Figure 6.4.6: Plots of the logistic, sine and tent maps for $r = 0.7$. The logistic and sine maps are typical examples of unimodal functions.

7 Synchronization

7.1 The period of a non-uniform oscillator

The Adler equation is

$$\dot{\theta} = \omega - a \sin \theta, \quad (7.1.1)$$

where $\omega > a > 0$. The period of the oscillations of the Adler system is then given by the integral

$$T = \int dt = \int_0^{2\pi} \frac{dt}{d\theta} d\theta = \int_{-\pi}^{\pi} \frac{d\theta}{\omega - a \sin \theta}, \quad (7.1.2)$$

The goal of this exercise is to evaluate this integral and find an expression for the period. First, we make the change of variables $u = \tan \frac{\theta}{2}$. Then $\theta = 2 \arctan(u)$ and the lower, upper integration bound becomes $-\infty, +\infty$ respectively. We have that

$$du = \frac{1}{2 \cos^2 \left(\frac{\theta}{2} \right)} d\theta, \quad (7.1.3)$$

and therefore $d\theta = 2 \cos^2(\theta/2) du$. Recall that

$$\cos(\arctan(x)) = \frac{1}{\sqrt{x^2 + 1}}, \quad (7.1.4)$$

and therefore, we find

$$d\theta = \frac{2}{u^2 + 1} du. \quad (7.1.5)$$

Now we have to rewrite $\sin \theta$ in terms of u . Note that

$$\begin{aligned} \sin \theta &= 2 \sin \left(\frac{\theta}{2} \right) \cos \left(\frac{\theta}{2} \right) \\ &= 2 \frac{u}{u^2 + 1}, \end{aligned} \quad (7.1.6)$$

where in the second equality, we made use of equation (7.1.4) along with

$$\sin(\arctan(x)) = \frac{x}{\sqrt{x^2 + 1}}. \quad (7.1.7)$$

Putting everything together, the above integral becomes

$$\begin{aligned} T &= \int_{-\infty}^{+\infty} \frac{2}{u^2 + 1} \frac{1}{\omega - a \frac{2u}{u^2 + 1}} du \\ &= \int_{-\infty}^{+\infty} \frac{1}{\frac{\omega}{2} u^2 - au + \frac{\omega}{2}} du. \end{aligned} \quad (7.1.8)$$

The denominator can be written as

$$\left(\sqrt{\frac{\omega}{2}}u - \frac{a}{\sqrt{2\omega}} \right)^2 + \frac{\omega}{2} - \frac{a^2}{2\omega}, \quad (7.1.9)$$

which is of the form $r + x^2$, with

$$x = \sqrt{\frac{\omega}{2}}u - \frac{a}{\sqrt{2\omega}}, \quad r = \frac{\omega}{2} - \frac{a^2}{2\omega} = \frac{\omega^2 - a^2}{2\omega}. \quad (7.1.10)$$

Note that this change of variables will not affect the integration bounds. Hence we have to evaluate the integral

$$T = \sqrt{\frac{2}{\omega}} \int_{-\infty}^{+\infty} \frac{dx}{r + x^2}. \quad (7.1.11)$$

We make the change of variables $x = \sqrt{r} \tan \alpha$, such that $dx = (\sqrt{r}/\cos^2(\alpha)) d\alpha$, and the integral becomes

$$\sqrt{\frac{2}{\omega}} \int_{-\pi/2}^{\pi/2} \frac{1}{r(1 + \tan^2 \alpha)} \frac{\sqrt{r}}{\cos^2 \alpha} d\alpha. \quad (7.1.12)$$

Using the identity $1 + \tan^2 \alpha = 1/\cos^2 \alpha$, the cosines cancel each other and we end up with

$$\sqrt{\frac{2}{\omega}} \frac{1}{\sqrt{r}} \int_{-\pi/2}^{\pi/2} d\alpha = \sqrt{\frac{2}{\omega}} \frac{\pi}{\sqrt{r}}. \quad (7.1.13)$$

After substituting r and some algebraic manipulations, we find

$$T = \frac{2\pi}{\sqrt{\omega^2 - a^2}}. \quad (7.1.14)$$

If $a = 0$, this is indeed the period of an ordinary oscillator. If $a \rightarrow \omega$, the period starts to diverge, which is the ‘‘bottleneck behaviour’’ of the system as discussed during the lecture on synchronization.

7.2 Triangle wave in firefly model

In the lecture on synchronization, we studied the oscillating flashes of fireflies, where $\theta(t)$ denoted the phase of the firefly’s flashing rhythm, with $\theta = 0$ corresponding to the instant when a flash is emitted. In the absence of stimuli, we have $\dot{\theta} = \omega$, with ω the frequency of the flashing. Now we apply a periodic stimulus with phase Φ determined by $\dot{\Phi} = \Omega$ (again, $\Phi = 0$ is the instant the stimulus emits a flash). When using the Adler equation to model the behaviour of fireflies, the sinusoidal form of the firefly’s response function

was chosen somewhat arbitrarily. In this section, we consider an alternative model, taking $\dot{\theta} = \omega + Af(\Phi - \theta)$, where $f(\phi)$ is now a triangle wave

$$f(\phi) = \begin{cases} \phi & \text{for } -\pi/2 \leq \phi \leq \pi/2 \\ \pi - \phi & \text{for } \pi/2 \leq \phi \leq 3\pi/2 \end{cases}, \quad (7.2.1)$$

and this extended periodically to the whole real line. The parameter A is called the *resetting strength* and effectively measures the strength with which the firefly modifies its instantaneous frequency. The triangle wave $f(\phi)$ is shown in Figure 7.2.1 below. We are interested in the behaviour of the system with this response function. For our calculations below, we let us inspire by section 4.5 in Strogatz [5].

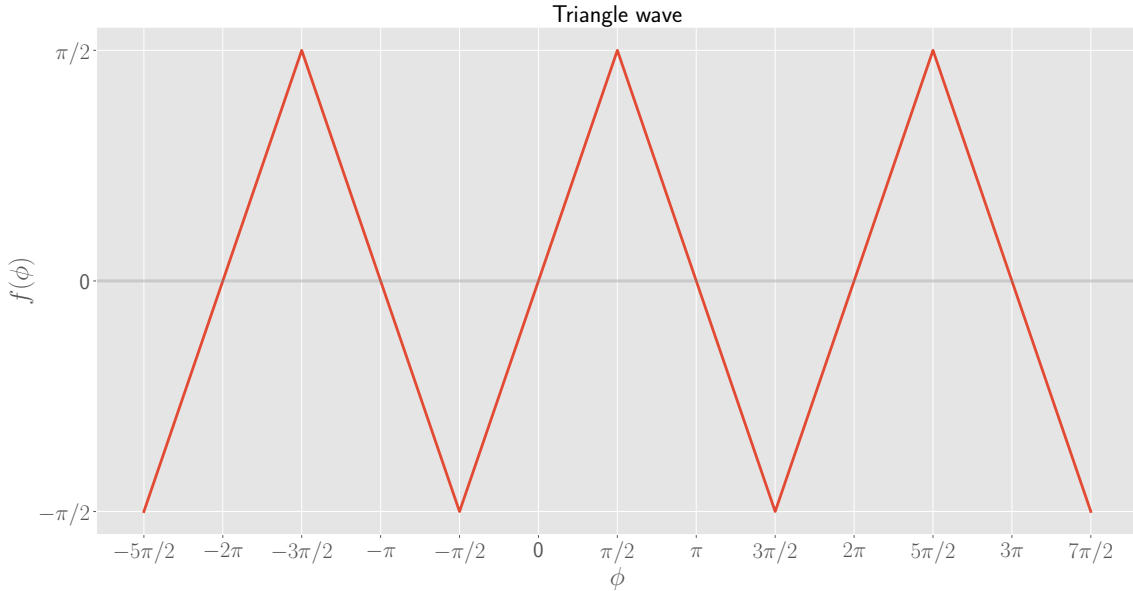


Figure 7.2.1: Plot of three periods of the triangle wave $f(\phi)$, given by equation (7.2.1).

The response of the firefly is best described by considering the phase difference $\phi \equiv \Phi - \theta$. From the differential equations defined earlier, we derive

$$\dot{\phi} = \dot{\Phi} - \dot{\theta} = \Omega - \omega - Af(\phi). \quad (7.2.2)$$

It is convenient to study this equation by non-dimensionalizing it. To this end, introduce

$$\mu = \frac{\Omega - \omega}{A}, \quad \tau = At. \quad (7.2.3)$$

First of all, we have that

$$\dot{\phi} = A(\mu - f(\phi)). \quad (7.2.4)$$

Furthermore, we find (letting primes denote derivatives with respect to τ)

$$\dot{\phi} = \frac{d\tau}{dt} \frac{d\phi}{d\tau} = A\phi' , \quad (7.2.5)$$

such that we end up with

$$\phi' = \mu - f(\phi) . \quad (7.2.6)$$

This differential equation allows us to study the behaviour of the phase difference ϕ between the stimulus and the firefly as a function of a single parameter μ , which can easily be done graphically. In Figure 7.2.2 below, we plot the right hand side of the differential equation for three different values for a positive parameter μ . We can easily see that for $0 < \mu < \pi/2$, the above equation has two fixed points ϕ^* , which can be determined graphically or analytically by solving $\phi' = 0$. This gives $f(\phi^*) = \mu$, with stability determined by the sign of $-f'(\phi^*)$. So there exists a stable fixed point at $\phi = \mu$, and an unstable fixed point at $\phi = \pi - \mu$. As μ increases and reaches $\mu = \pi/2$, these fixed points come together in a saddle-node bifurcation.

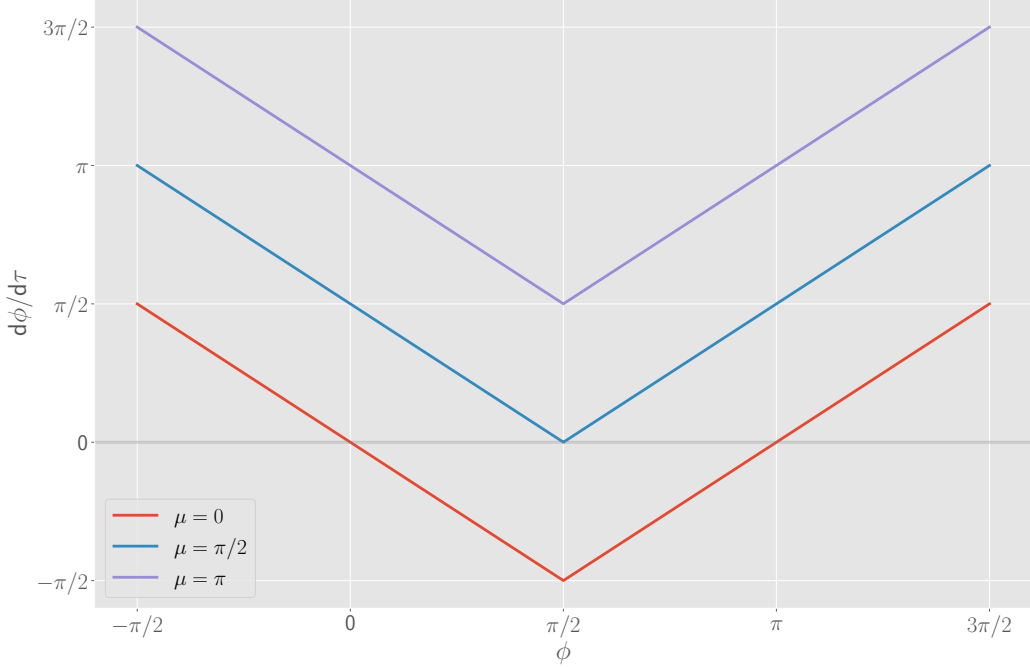


Figure 7.2.2: Plot of the differential equation (7.2.6) for $\mu = 0, \pi/2$ and π , showing the stable and unstable fixed points come together in a saddle-node bifurcation at $\mu = \pi/2$.

The important aspect is that the *range of entrainment* in the triangle wave model is $0 < \mu < \pi/2$, with phase difference during *phase locking* given by

$$\phi^* = \mu = \frac{\Omega - \omega}{A} . \quad (7.2.7)$$

Note that $\mu > 0$ means that $\Omega > \omega$, and we intuitively understand why $\phi^* > 0$. This means that the stimulus flashes ahead of the firefly, but both have the same frequency.

The above considerations and plot were for a positive μ , but we can equally well do the same analysis for negative μ . The expressions for the fixed points still hold in this regime, and due to the symmetry of the right hand side of the differential equation (7.2.6), we see that the range of entrainment for negative μ is $-\pi/2 < \mu < 0$. Hence we conclude that the full range of entrainment is $-\pi/2 < \mu < \pi/2$. This implies that the entrainment range for the stimulus frequency is

$$\omega - \frac{\pi}{2}A < \Omega < \omega + \frac{\pi}{2}A. \quad (7.2.8)$$

For μ (or Ω) outside the range of entrainment, the right hand side of equation (7.2.6) is always strictly positive (as is also clear from the example in Figure 7.2.2), such that the phase difference increases indefinitely, and the solution is a *phase drift*. To find the period T for these drifting solutions, we proceed as in the first section, and compute

$$T = \int dt = \int_0^{2\pi} \frac{dt}{d\phi} d\phi = \int_0^{2\pi} \frac{1}{\Omega - \omega - Af(\phi)} d\phi. \quad (7.2.9)$$

Since the integrand is periodic with period 2π , we can equally well integrate in the range $-\pi/2 \leq \phi \leq 3\pi/2$ to get the same result. Using the definition of $f(\phi)$, we find

$$T = \int_{-\pi/2}^{\pi/2} \frac{1}{\Omega - \omega - A\phi} d\phi + \int_{\pi/2}^{3\pi/2} \frac{1}{\Omega - \omega - A(\pi - \phi)} d\phi. \quad (7.2.10)$$

We can easily compute the above integrals, and we find, after some straightforward algebraic manipulations, that the period is given by

$$T = \frac{2}{A} \ln \left| \frac{\Omega - (\omega - A\frac{\pi}{2})}{\Omega - (\omega + A\frac{\pi}{2})} \right|. \quad (7.2.11)$$

We verify this expression by numerically integrating equation (7.2.2) for the specific values⁷ $A = 1$, $\omega = 1.6$ and $\Omega = 3.3$, such that $\Omega > \omega + A\pi/2$ and there are drifting solutions. Equation (7.2.11) predicts that $T \approx 6.4628$. In Figure 7.2.3 below, we plot the solution with initial condition $\phi(0) = 0$. The sudden jump in the graph is since we take into account that ϕ is a periodic variable with period 2π . Therefore, at the jump, $\phi(t)$ reaches 2π and the system returns to its initial configuration, from which we then deduce the period. This example agrees with the analytic calculation above. Note that the system spends the majority of its time getting through a bottleneck (which is the ‘plateau’ we see in the graph). As expected, this plateau (and hence the period) becomes larger if we let $\Omega \rightarrow \omega - A\pi/2$ or

⁷All parameters have dimensions of a frequency, but we will not use a specific unit in what follows, since we only want to briefly check via a numerical computation if the analytic calculation makes sense.

$\Omega \rightarrow \omega + A\pi/2$ (i.e., approach the bounds of the entrainment range). This is also predicted by equation (7.2.11).

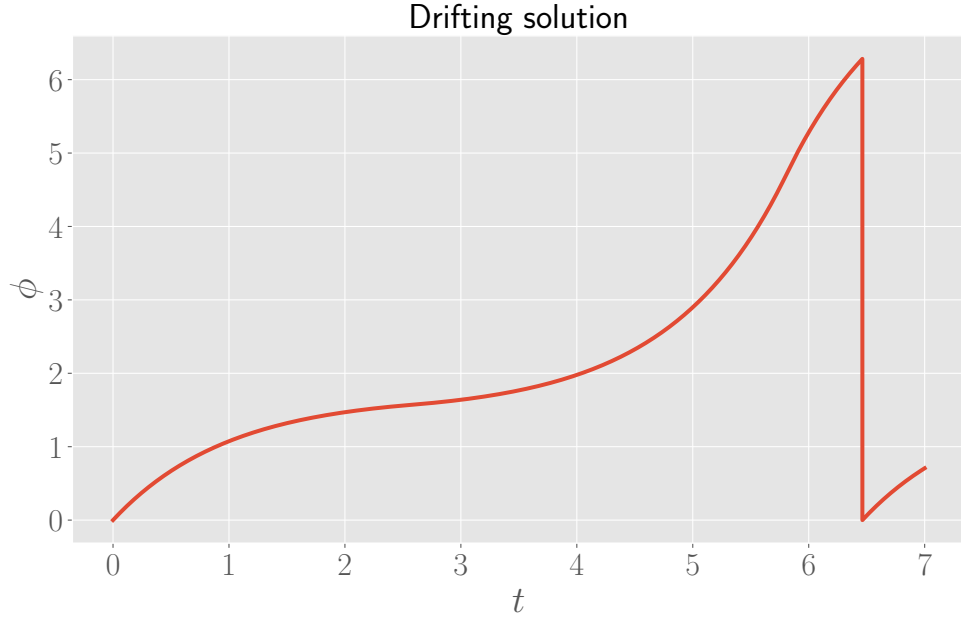


Figure 7.2.3: Drifting solution for $A = 1$, $\omega = 1.6$ and $\Omega = 3.3$, with period $T \approx 6.4628$.

7.2.1 Comparison between firefly models

We will now briefly compare the triangle wave model, which used $f(\phi)$ as defined above, with the model that was studied during the lecture (or section 4.5 in Strogatz) which used $f(\phi) = \sin \phi$. In the latter, the range of entrainment was $\omega - A \leq \Omega \leq \omega + A$, so the triangle wave model has a larger range of entrainment. However, both ranges are symmetric around ω . In Figure 7.2.4, we compare the behaviour of the period T of drifting solutions as a function of Ω for both models. Both models have a similar dependence on Ω for the period, especially for larger values of Ω . We conclude that the qualitative behaviour of the system is identical in both models.

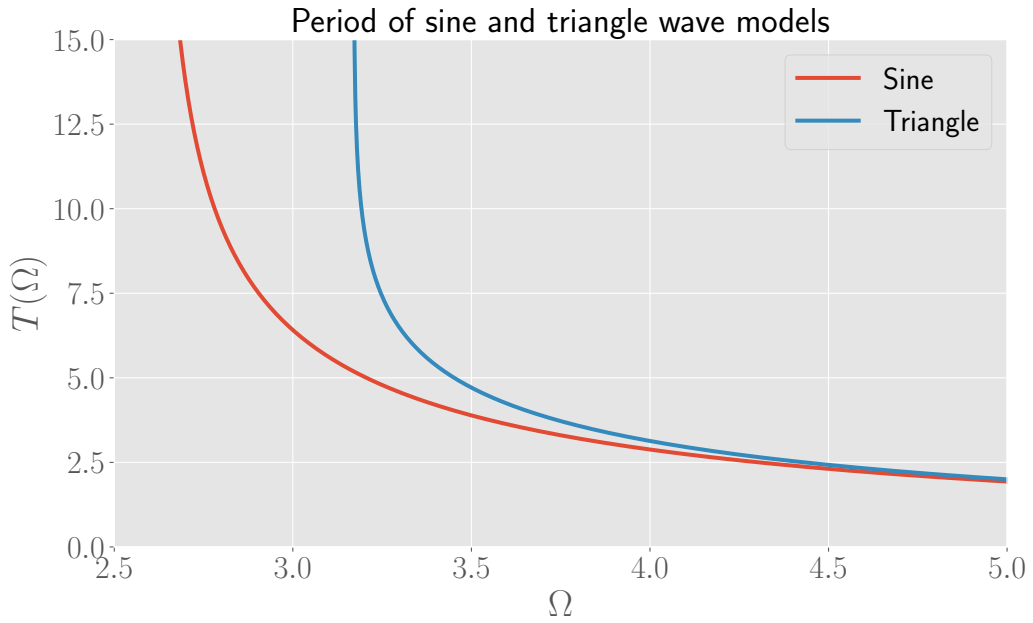


Figure 7.2.4: Period of drifting solutions for the sine and triangle wave models as a function of the stimulus frequency Ω , taking $A = 1$ and $\omega = 1.6$ for both graphs. Note that the range of entrainment is smaller for the sine model, which explains why the divergence of this curve occurs earlier than the triangle model.

8 Travelling wave solutions of reaction diffusion models

8.1 Fisher-Kolmogorov equation

In the lecture, we discussed the Fisher-Kolmogorov equation

$$\frac{\partial u}{\partial t} = \frac{\partial^2 u}{\partial x^2} + u(1-u), \quad (8.1.1)$$

and considered travelling wave solutions of this equation, i.e. solutions of the type $u(x, t) = f(x - ct) \equiv f(z)$, with boundary conditions $\lim_{z \rightarrow -\infty} f(z) = 1$ and $\lim_{z \rightarrow +\infty} f(z) = 0$.

8.1.1 Minimal speed and the phase portrait method

We will show, using the phase portrait method, that wavelike solutions to the Fisher-Kolmogorov equation must have a minimal speed c_{\min} . Therefore, we are interested in the following differential equation in the variable z (with primes denoting derivatives with respect to z)

$$u'' + cu' + u(1-u) = 0, \quad (8.1.2)$$

which is now an ordinary second-order differential equation instead of a partial differential equation. To proceed, we apply a well-known trick to transform this into a set of two first-order ODE's by defining $v = u'$, such that the above equation is equivalent to the system

$$\begin{cases} u' = v \\ v' = -cv - u(1-u) \end{cases}. \quad (8.1.3)$$

This is now a two-component system, for which we can apply the usual techniques. The fixed points of the above system are $(0, 0)$ and $(1, 0)$. The Jacobian matrix of the above system is

$$J(u, v) = \begin{pmatrix} 0 & 1 \\ -1 + 2u & -c \end{pmatrix}. \quad (8.1.4)$$

Evaluating the Jacobian at $(1, 0)$ gives

$$J(1, 0) = \begin{pmatrix} 0 & 1 \\ 1 & -c \end{pmatrix}. \quad (8.1.5)$$

Since $\det J(1, 0) = -1 < 0$, this fixed point is guaranteed to be a saddle node, for all values of c . Evaluating the Jacobian at the origin, we find

$$J(0, 0) = \begin{pmatrix} 0 & 1 \\ -1 & -c \end{pmatrix}. \quad (8.1.6)$$

The characteristic equation of this matrix is

$$\lambda^2 + c\lambda + 1 = 0, \quad (8.1.7)$$

which gives the eigenvalues

$$\lambda_{\pm} = \frac{-c \pm \sqrt{c^2 - 4}}{2}. \quad (8.1.8)$$

The nature of the origin as fixed point depends on the value of c . Indeed, if $c < 2$, the square root above is an imaginary number and λ_{\pm} is a pair of complex conjugated eigenvalues. In this case, the fixed point will be a stable spiral. However, if $c > 2$, both λ_{\pm} will be real and negative eigenvalues, such that the fixed point is a stable node. Recall that we are looking for wavelike solutions that connect the two fixed points. If $c < 2$, the origin is a stable spiral, and if we start from the fixed point⁸ $(1, 0)$ and approach the origin, the solution will start to spiral around the origin. This causes the solution to go in the half-plane $u < 0$. However, this is not physical or biological, since we would like u to represent populations or concentrations for instance, in which we impose that $u \geq 0$ at all times. Therefore, we need to exclude these spiraling trajectories from our solutions, which gives the condition $c > 2$, such that the minimal speed is $c_{\min} = 2$.

8.1.2 Numerical integration

Consider now the interval $[-20, 20]$ for x and an initial condition

$$u_{\epsilon}(x, 0) = \frac{e^{-x^2}}{2}. \quad (8.1.9)$$

By discretizing space and time, we numerically integrate the Fisher-Kolmogorov equation with the above initial condition. The discretization is done as follows. An interval $[a, b]$ is divided into N parts (always chosen to be equidistant in our code). Let $u_n(t)$ be the value at the n -th point in this partition of the interval. Then we can numerically integrate the equations

$$\frac{du_1}{dt} = \frac{1}{\Delta x^2}(u_2(t) - u_1(t)) + f(u_1(t)) \quad (8.1.10)$$

$$\frac{du_n}{dt} = \frac{1}{\Delta x^2}(u_{n+1}(t) - 2u_n(t) + u_{n-1}(t)) + f(u_n(t)) \quad n = 2, 3, \dots, N-1 \quad (8.1.11)$$

$$\frac{du_N}{dt} = \frac{1}{\Delta x^2}(u_{N-1}(t) - u_N(t)) + f(u_N(t)) \quad (8.1.12)$$

in time (similar to how we integrated ODE's in previous assignments). Here, $f(u)$ denotes the reaction function, which is the logistic function $f(u) = u(1 - u)$ for the Fisher-Kolmogorov equation.

⁸What we really mean is “if we start from an initial condition that is arbitrarily close to the fixed point $(1, 0)$ ”. In the following sections, where we again look for orbits between fixed points, we will keep on abusing this terminology.

To see if the numerical integration scheme works, we can apply it in a test case, where we ‘turn off’ the reaction part of the Fisher-Kolmogorov equation and only keep the diffusion part. Therefore, the exercise is to solve a diffusion equation, for which we easily find an analytic expression which can then be compared with a numerical integration.

As seen in the lecture on the diffusion equation by professor Carlon, if we have an initial condition $g(x)$ (which is given by equation (8.1.9) for this exercise), then the solution at time t of the diffusion equation is given by (note that we set $D = 1$)

$$u(x, t) = \int g(x_0) \frac{1}{\sqrt{4\pi t}} e^{-(x-x_0)^2/4t} dx_0. \quad (8.1.13)$$

Substituting our initial condition, we find

$$u(x, t) = \frac{1}{2\sqrt{4\pi t}} e^{-x^2/4t} \int \exp \left[-\frac{4t+1}{4t} x_0^2 + \frac{x}{2t} x_0 \right] dx_0. \quad (8.1.14)$$

The remaining integral is a generalization of the Gaussian integral, for which we can use the result

$$\int \exp(-ax^2 + bx + c) dx = \sqrt{\frac{\pi}{a}} \exp\left(\frac{b^2}{4a} + c\right), \quad (8.1.15)$$

such that the solution, after some straightforward algebraic manipulations, is

$$u(x, t) = \frac{1}{2\sqrt{4t+1}} \exp\left(-\frac{x^2}{4t+1}\right). \quad (8.1.16)$$

In Figure 8.1.1 below, we plot this exact solution at time $t = 20$, along with the numerically obtained solution for a particular discretization of space and time. Both agree very well, although small deviations are visible at the endpoints of the interval. For lower values of t , the two graphs match even better, while for higher t , the deviations become large and we have to be cautious and need to improve the discretization. However, it turns out that in the following exercises we will not need solutions with $t > 20$, such that we can conclude our numerical scheme to be adequate to obtain solutions for this assignment.

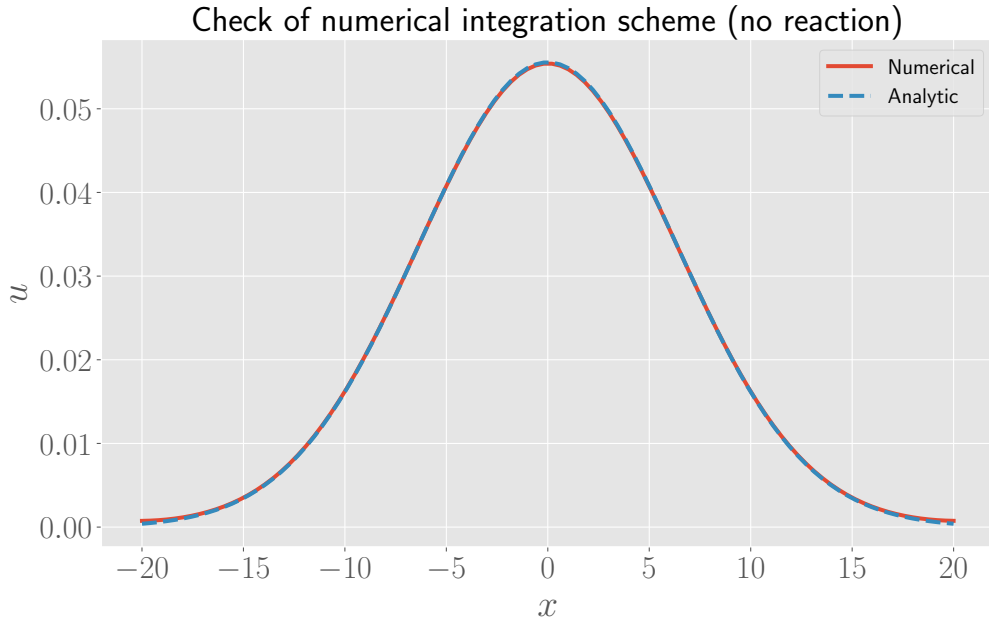


Figure 8.1.1: Test of the numerical scheme, without including the reaction part, by comparing the numerical result with the analytic calculation for the diffusion equation. Both solutions are evaluated at $t = 20$ (more details in the Python notebook).

Now that we are fairly confident that our numerical scheme works, we use it to obtain the solution to the Fisher-Kolmogorov equation with the initial condition given in equation (8.1.9). The result for different values of t is shown in Figure 8.1.2 below. The perturbation at the origin grows in size, and the solution has two travelling waves: one going in the positive x direction, while the other goes in the negative x direction. The solution tends to grow towards 1. However, due to the logistic growth in the Fisher-Kolmogorov equation, as soon as $u(x, t) \approx 1$ at a certain position x , the solution stops growing. This is in agreement with our earlier observation that $u = 1$ is a stable steady state. Hence we conclude that the solution is indeed a travelling wave, going from the unstable steady state $u = 0$ towards the stable steady state $u = 1$. Note that at early times, the curve is not very smooth around the origin, possibly because at early times, the solution is still strongly varying. We could improve the discretization of space by either increasing N , or choosing for a partition which does not give equidistant values for x , but takes more samples where the initial condition varies strongly. However, since we are mainly interested in later times (because the wave has to converge to the minimal speed) and want to reduce the computation time, we will not delve deeper into this minor issue.

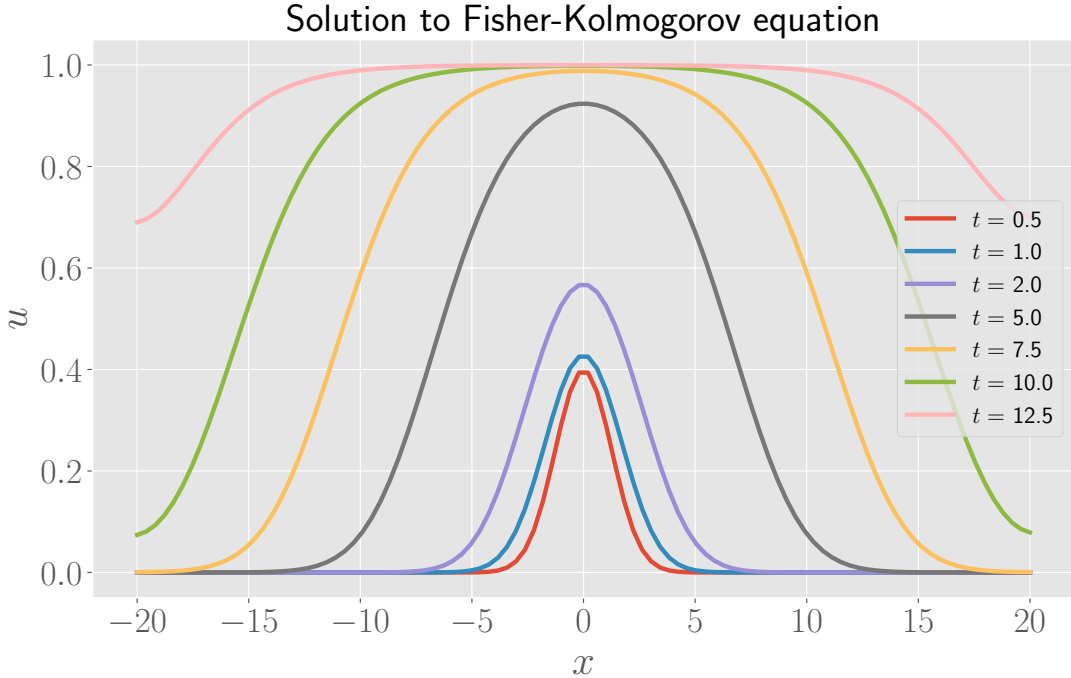


Figure 8.1.2: Solution to the Fisher-Kolmogorov equation for various values of t (shown in the legend). The solution is a travelling wave with one wave propagating in the positive x direction, and another in the negative x direction.

To estimate the speed of the wave, we let us inspire by the lecture. There, the idea to determine the speed of a travelling wave was to plot a straight line at $u = A$, with A some arbitrary number. We then determine at various times t the location $x_A(t)$ such that $u(x_A(t), t) = A$. This method is applied and shown in Figure 8.1.3 below, taking t values between 1.5 and 6.5, with a separation of $\Delta t = 1$ between each plot. Since $\Delta t = 1$ between successive plots, we estimate the speed by estimating the difference $\Delta x_A(t) = x_A(t_{n+1}) - x_A(t_n)$, which gives a speed $c^* \approx 1.8$ of the wave.

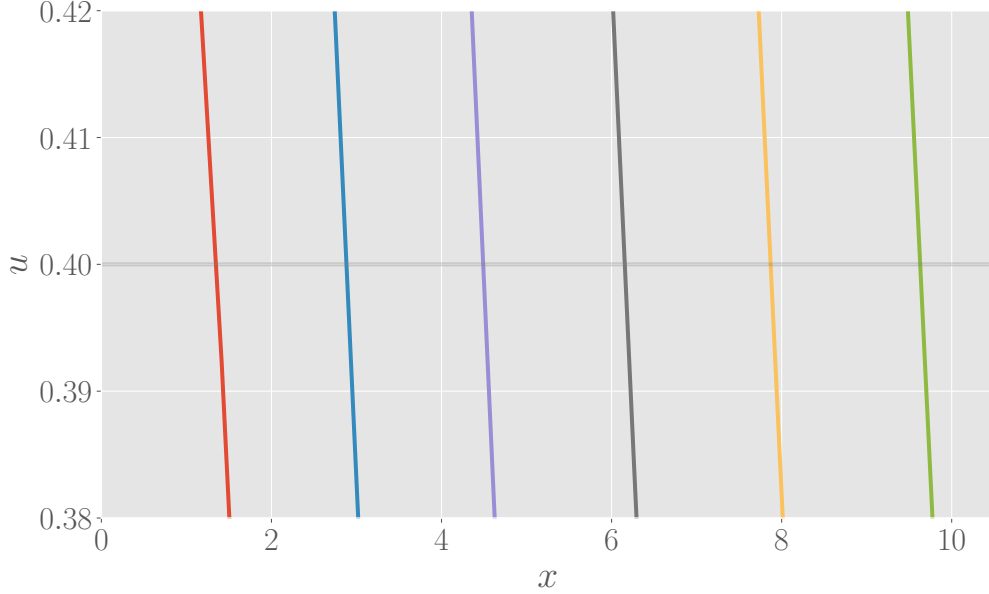


Figure 8.1.3: Close-up around $u = A = 0.4$ of solutions for various values of t with separation $\Delta t = 1$ between successive plots to estimate the speed of the wave.

This method to determine the speed is also implemented in a Python function. To get a reliable estimate numerically, we should have a finer partition of the interval and therefore increase the value of N . We find that $c^* \approx 1.8247$. However, for higher values of N , the discretization of time must be improved as well, so one should be careful when applying this function and check the numerical scheme once the discretization is changed.

We conclude that the speed of the wave is equal to the minimal speed $c_{\min} = 2$: the convergence to the minimal velocity is known to be very slow, as mentioned in the assignment, such that the value we determine is around 10% lower.

8.1.3 Approximate solution

We now find an approximate solution of the Fisher-Kolmogorov equation, which can be found by considering the change of variables $\xi = z/c$. Defining $g(\xi) = u(z)$, the Fisher-Kolmogorov equation can be rewritten if we use equation (8.1.2), along with the fact that

$$\frac{du}{dz} = \frac{d\xi}{dz} \frac{dg}{d\xi} = \frac{1}{c} g' , \quad (8.1.17)$$

such that we find the equivalent equation

$$\frac{1}{c^2} g''(\xi) + g'(\xi) + g(\xi)(1 - g(\xi)) = 0 . \quad (8.1.18)$$

Since the minimal velocity is 2, we assume we can neglect the first term, and therefore find

$$\frac{dg}{d\xi} = -g(1-g). \quad (8.1.19)$$

We can solve the above equation by separation of variables, such that

$$\int \frac{dg}{g(1-g)} = - \int d\xi. \quad (8.1.20)$$

The integral on the left hand side is computed by using partial fractions, noting that

$$\frac{1}{g(1-g)} = \frac{1}{g} + \frac{1}{1-g}, \quad (8.1.21)$$

and hence we find

$$\ln \frac{g}{1-g} = -\xi, \quad (8.1.22)$$

from which we then find the solution

$$g = \frac{e^{-\xi}}{1+e^{-\xi}} = \frac{1}{1+e^{\xi}}. \quad (8.1.23)$$

Written down in the original variables, this becomes

$$u(z) = \frac{1}{1+e^{z/c}}. \quad (8.1.24)$$

This solution satisfies the boundary conditions specified in the first exercise, namely, that $u \rightarrow 1$ for $x \rightarrow -\infty$, and $u \rightarrow 0$ for $x \rightarrow +\infty$.

In Figure 8.1.4 below, we compare the approximate solution (with $c = c_{\min} = 2$) with the solution obtained from the numerical integration found earlier. At early times, the approximate solution is significantly larger than the numerical integration for $x \leq 10$. This is because the initial conditions of both solutions are quite different, as seen from Figure 8.1.5. The initial condition for the numerical integration goes to zero much faster in this range than the approximate solution. Therefore, the approximate solution has a ‘head start’ relative to the numerically integrated solution. For later times, both solutions have a similar shape (see for example the curves at $t = 10$). It appears that the wave of the approximate solution is faster than the numerical integration, but this is explained by the slow convergence to the minimal velocity, as mentioned earlier.

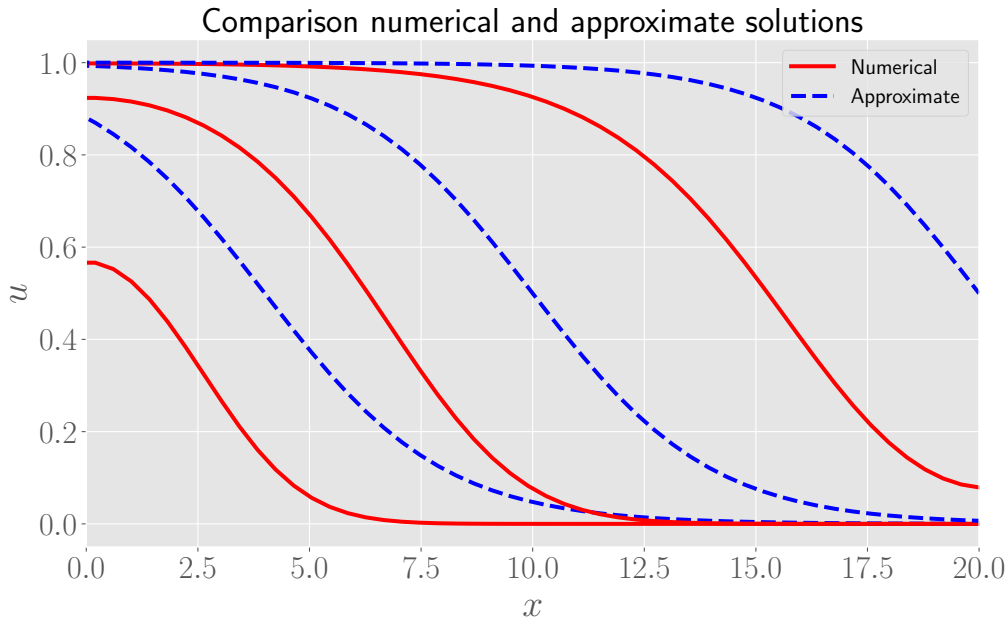


Figure 8.1.4: Comparison between the approximate solution and the numerical integration of the Fisher-Kolmogorov equation. Times shown are (from left to right) $t = 2, 5$ and 10 .

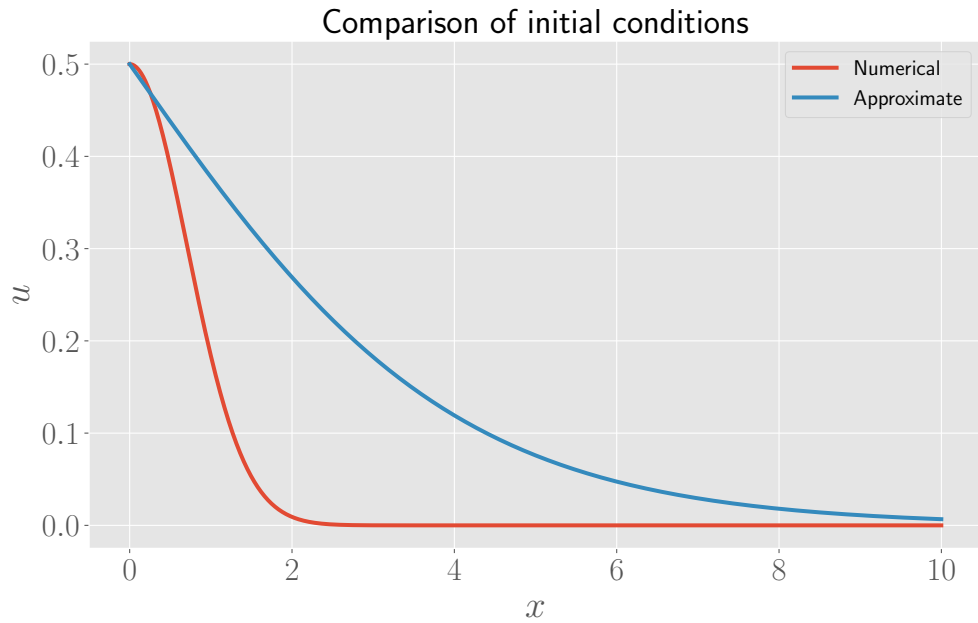


Figure 8.1.5: Comparison of initial conditions of the approximate solution and the numerical integration.

8.2 Travelling waves in bistable systems

In the Fisher-Kolmogorov model from the previous section, the homogeneous steady state solutions were unstable ($u = 0$) or stable ($u = 1$). In this section, we consider the alternative model

$$\frac{\partial u}{\partial t} = \frac{\partial^2 u}{\partial x^2} + u(u - a)(1 - u), \quad (8.2.1)$$

with $0 < a < 1$. In this case, there are two homogeneous stable steady state solutions, namely $u = 0$ and $u = 1$, and an unstable one, $u = a$. We again look for solutions of the form $u(x, t) = f(x - ct) = f(z)$, with boundary conditions $\lim_{z \rightarrow -\infty} f(z) = 1$ and $\lim_{z \rightarrow +\infty} f(z) = 0$. Below, we fix $a = 1/4$.

8.2.1 Spatial dynamical system and fixed points

First, note that we can rewrite the above differential equation as

$$u'' + cu' + u(u - a)(1 - u) = 0, \quad (8.2.2)$$

where primes denote derivatives with respect to z . Proceeding as in the previous section, we define $v = u'$, such that the above equation becomes a two-component dynamical system

$$\begin{cases} u' = v \\ v' = -cv - u(u - a)(1 - u) \end{cases}. \quad (8.2.3)$$

This system has three fixed points: $(0, 0)$, $(1, 0)$ and $(a, 0)$. We want to show that there exists a unique velocity c^* for a wavelike solution. To determine the value of c^* numerically, we look for a trajectory in the (u, v) plane connecting the two saddle nodes $(1, 0)$ and $(0, 0)$ (i.e., a *heteroclinic orbit*), starting from $(1, 0)$. The Jacobian associated to the above system of differential equations is

$$J(u, v) = \begin{pmatrix} 0 & 1 \\ 3u^2 - 2(1+a)u + a & -c \end{pmatrix}. \quad (8.2.4)$$

At the origin, the $J_{12}(0, 0)$ component is a , so $\det J(0, 0) = -a < 0$ and the origin is a saddle node. At the fixed point $(a, 0)$, the $J_{12}(a, 0)$ component is $a(a - 1)$ such that $\det J(a, 0) = -a(a - 1) > 0$. Since $\text{tr } J(a, 0) = -c < 0$, this implies that the fixed point $(a, 0)$ is a stable node or stable spiral. Finally, evaluating the Jacobian at the fixed point $(1, 0)$, we have

$$J(1, 0) = \begin{pmatrix} 0 & 1 \\ 1-a & -c \end{pmatrix}, \quad (8.2.5)$$

and therefore $\det J(1, 0) = a - 1 < 0$, so this is a saddle node as well. The characteristic equation for this matrix is

$$\lambda^2 + c\lambda + a - 1 = 0, \quad (8.2.6)$$

which has solutions

$$\lambda_{\pm} = \frac{-c \pm \sqrt{c^2 - 4(a-1)}}{2}, \quad (8.2.7)$$

with corresponding eigenvectors

$$\mathbf{v}_+ = \begin{pmatrix} 1 \\ \lambda_+ \end{pmatrix}, \quad \mathbf{v}_- = \begin{pmatrix} 1 \\ \lambda_- \end{pmatrix}. \quad (8.2.8)$$

8.2.2 Heteroclinic orbit and wavelike solution

To find a trajectory in the (u, v) -plane connecting the saddle nodes $(1, 0)$ and $(0, 0)$, starting from $(1, 0)$, we use an initial point (u_0, v_0) close to $(1, 0)$ and which lies along the direction of the repulsive eigenvector \mathbf{v}_+ , for some parameter value of c . If we let this point flow along the phase portrait of the dynamical system (8.2.3), the solution will (i) cross the u -axis before the origin is reached, (ii) flow to infinity or (iii) reach the origin (i.e. the trajectory is a heteroclinic orbit), depending on the value of c . After some trial and error runs, it turns out that for c between 0.35 and 0.355, a heteroclinic orbit is reached. To determine the optimal value of c , we solve the differential equation for various values of c in this range. The code checks if the solutions are closer than a distance ϵ (taken to be 10^{-3} in the notebook) away from the origin, and saves the corresponding values of c . We then take c^* as the mean of these values, resulting in $c^* = 0.35365$. In Figure 8.2.1, we show the heteroclinic orbit for this value of c^* .

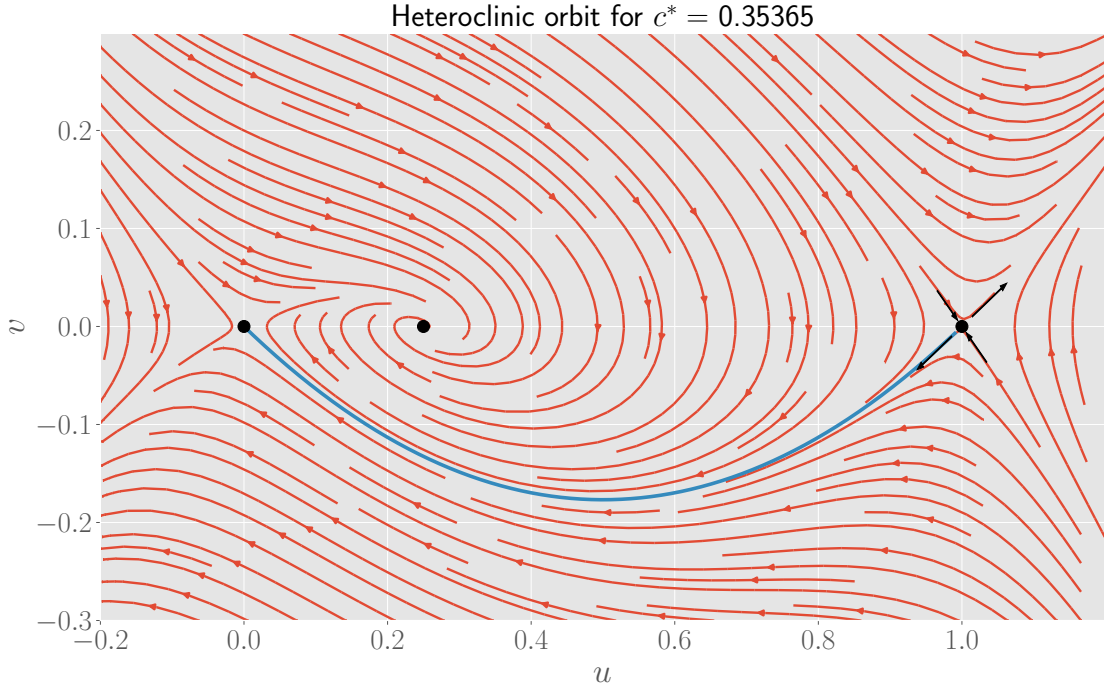


Figure 8.2.1: A heteroclinic orbit (blue curve) is generated from (u_0, v_0) if $c^* = 0.35365$. The fixed points are shown as black dots. The arrows denote the direction of repulsion or attraction of the saddle node $(1, 0)$.

Using as initial condition

$$u_\epsilon(x, 0) = \frac{1}{1 + e^x}, \quad (8.2.9)$$

we find that the solution $u(x, t)$ of the above differential equation is a wave with speed c^* . To verify this, we proceed as in the first section. Choosing an arbitrary A , we plot the numerically obtained solution for a few values of t and determine the position $x_A(t)$ such that $u(x_A(t), t) = A$. We take as separation in time $\Delta t = 1/c^* \approx 2.83$, such that the location of $x_A(t)$ should increase by 1 in successive plots. In Figure 8.2.2, the solutions are plotted, and we can verify that this is indeed the case by considering the close-up in Figure 8.2.3. So we conclude that the above initial condition leads to a wavelike solution with speed c^* .

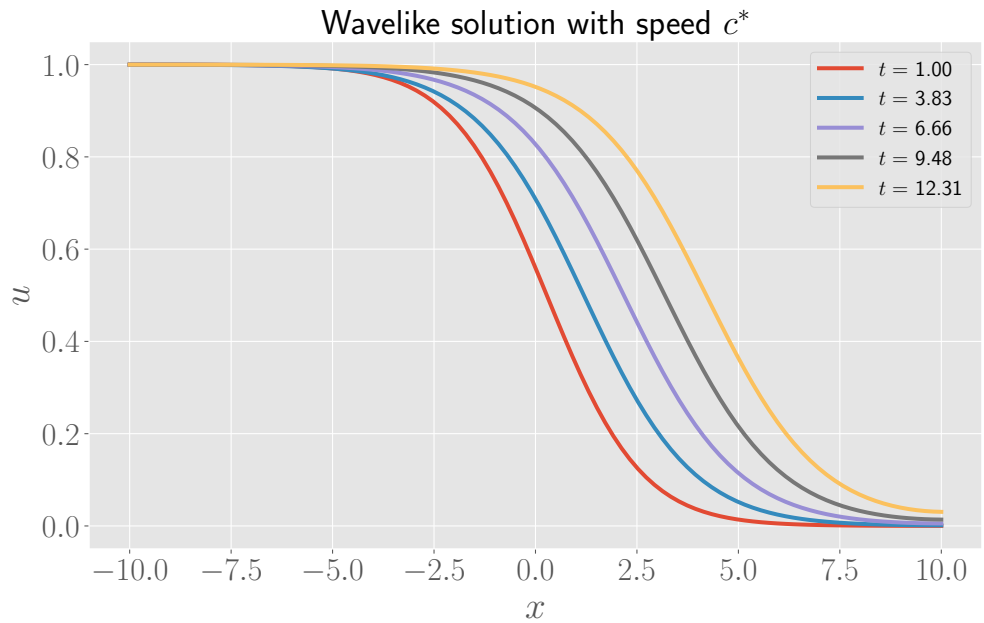


Figure 8.2.2: Plot of the solution for various values of t , shown in the legend, with separation $\Delta t = 1/c^* \approx 2.83$.

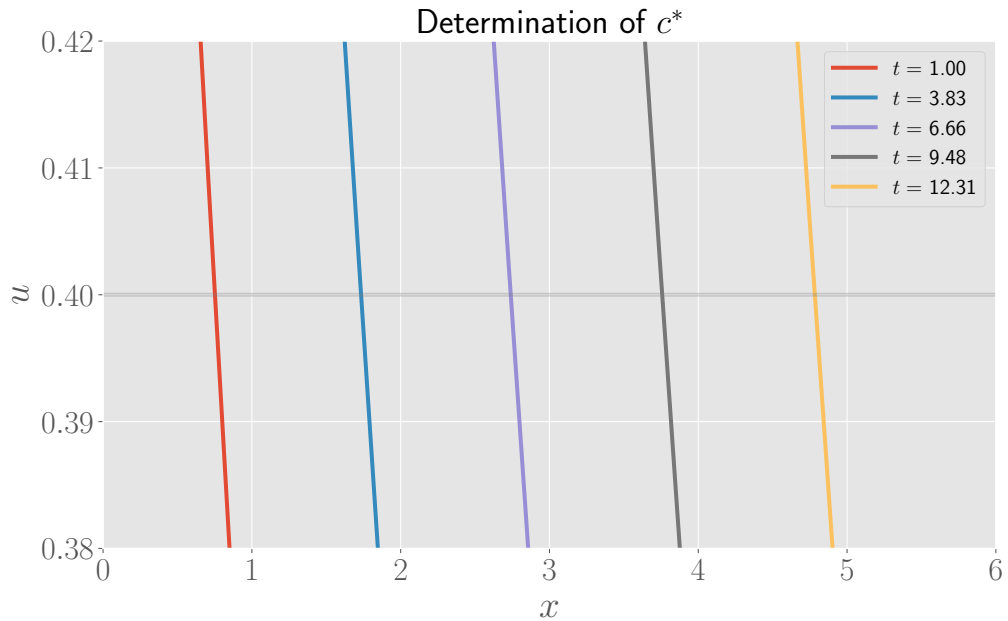


Figure 8.2.3: Close-up of the solutions shown in Figure 8.2.2 around $u = A = 0.4$ to determine the speed of the wave.

8.3 Special solution of the Fisher-Kolmogorov equation

Recall that the Fisher-Kolmogorov equation is

$$\frac{\partial u}{\partial t} = \frac{\partial^2 u}{\partial x^2} + u(1 - u). \quad (8.3.1)$$

We now show that

$$u(z) = \frac{1}{(1 + Ae^{z/\sqrt{6}})^2} \quad (8.3.2)$$

where A is an arbitrary constant and $z = x - ct$, is a travelling wave solution of the Fisher-Kolmogorov equation with wave velocity equal to $c = 5/\sqrt{6}$. We will refer to this solution as the ‘special solution’.

We first compute each term in the Fisher-Kolmogorov equation. For the left hand side, we find

$$\text{LHS} = \frac{\partial u}{\partial t} = \frac{2c}{\sqrt{6}} \frac{Ae^{z/\sqrt{6}}}{(1 + Ae^{(x-ct)/\sqrt{6}})^3}. \quad (8.3.3)$$

For the right hand side, the spatial derivative term is

$$\begin{aligned} \frac{\partial^2 u}{\partial x^2} &= \frac{\partial}{\partial x} \left(-\frac{2A}{\sqrt{6}} \frac{e^{(x-ct)/\sqrt{6}}}{(1 + Ae^{(x-ct)/\sqrt{6}})^3} \right) \\ &= -\frac{2A}{\sqrt{6}} \frac{1}{\sqrt{6}} e^{(x-ct)/\sqrt{6}} \left(\frac{1 + Ae^{(x-ct)/\sqrt{6}} - 3Ae^{(x-ct)/\sqrt{6}}}{(1 + Ae^{(x-ct)/\sqrt{6}})^4} \right) \\ &= \frac{Ae^{(x-ct)/\sqrt{6}}}{(1 + Ae^{(x-ct)/\sqrt{6}})^4} \left(-\frac{1}{3} + \frac{2}{3} Ae^{(x-ct)/\sqrt{6}} \right). \end{aligned} \quad (8.3.4)$$

The second term in the right hand side can be written as

$$u(1 - u) = \frac{Ae^{(x-ct)/\sqrt{6}}}{(1 + Ae^{(x-ct)/\sqrt{6}})^4} \left(2 + Ae^{(x-ct)/\sqrt{6}} \right). \quad (8.3.5)$$

Summing both together, the full right hand side is given by

$$\text{RHS} = \frac{5}{3} \frac{Ae^{(x-ct)/\sqrt{6}}}{(1 + Ae^{(x-ct)/\sqrt{6}})^4} \left(1 + Ae^{(x-ct)/\sqrt{6}} \right) = \frac{5}{3} \frac{Ae^{(x-ct)/\sqrt{6}}}{(1 + Ae^{(x-ct)/\sqrt{6}})^3}. \quad (8.3.6)$$

Comparing with the left hand side in equation (8.3.3), we conclude that $u(z)$ is indeed a solution if we require

$$\frac{2c}{\sqrt{6}} = \frac{5}{3}, \quad (8.3.7)$$

which indeed gives a speed $c = 5/\sqrt{6}$ for this wavelike solution.

Figure 8.3.1 below shows a plot of the special solution in the (u, v) -plane, with $v = u'$, along with the phase portrait of the dynamical system from equation (8.1.3) for $c = 5/\sqrt{6}$. The special solution is a heteroclinic orbit, connecting the two saddle nodes $(1, 0)$ and $(0, 0)$.

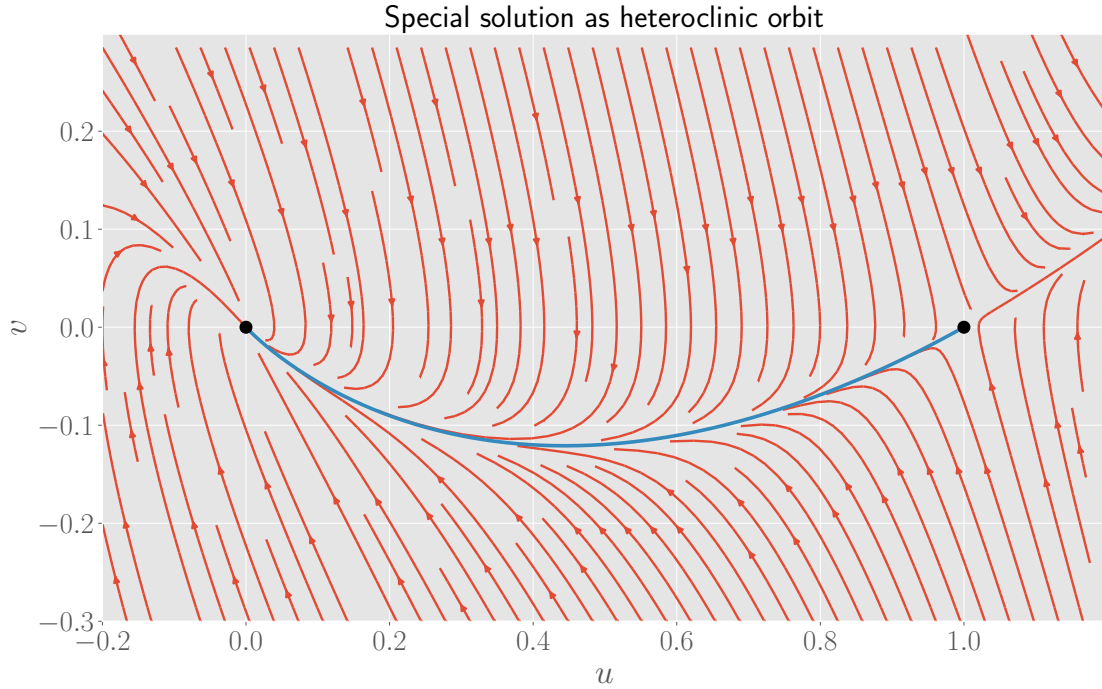


Figure 8.3.1: Plot of the special solution, shown in blue, in phase space along with the phase portrait. The solution is a heteroclinic orbit, connecting the fixed points $(1, 0)$ and $(0, 0)$ (black dots).

We compare this wave with the solution we obtained numerically in the first section in Figure 8.3.2 below. As expected, the special solution is slightly faster than the numerically integrated solution. In fact, the shape of the wave of this special solution resembles the shape of the approximate solution from the first exercise, and hence our discussion from that exercise can be repeated here. Indeed, Figure 8.3.3 compares these two solutions, and we see the approximate solution is a good approximation to the special solution. The approximate solution consistently has larger values for u , but has the same shape as the special solution.

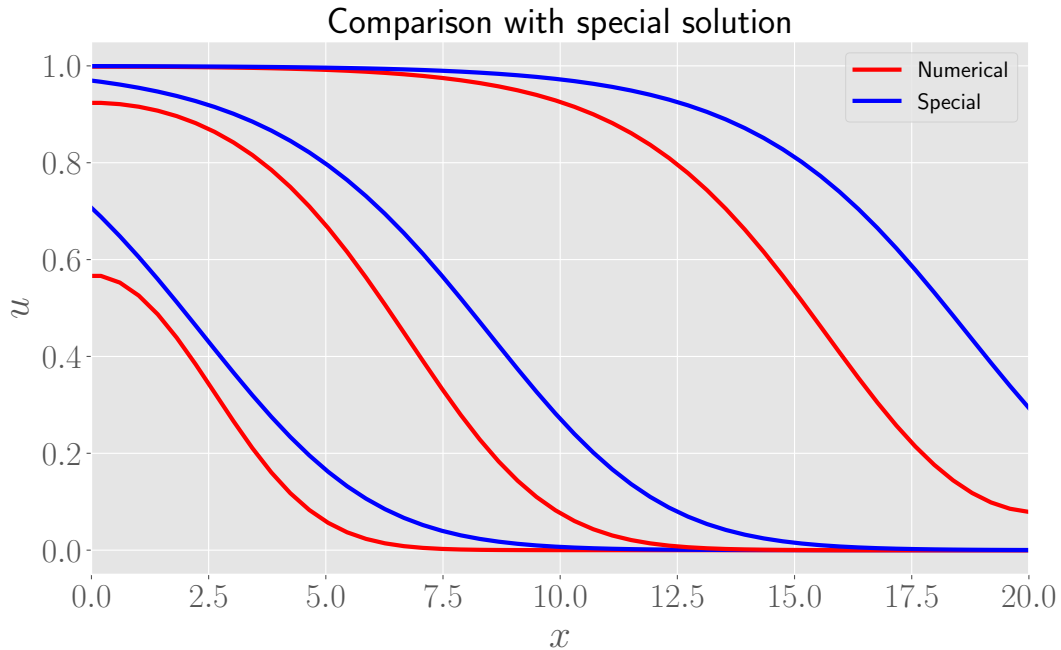


Figure 8.3.2: Comparison between special solution and numerical integration. Times shown are (from left to right) $t = 2, 5$ and 10 .

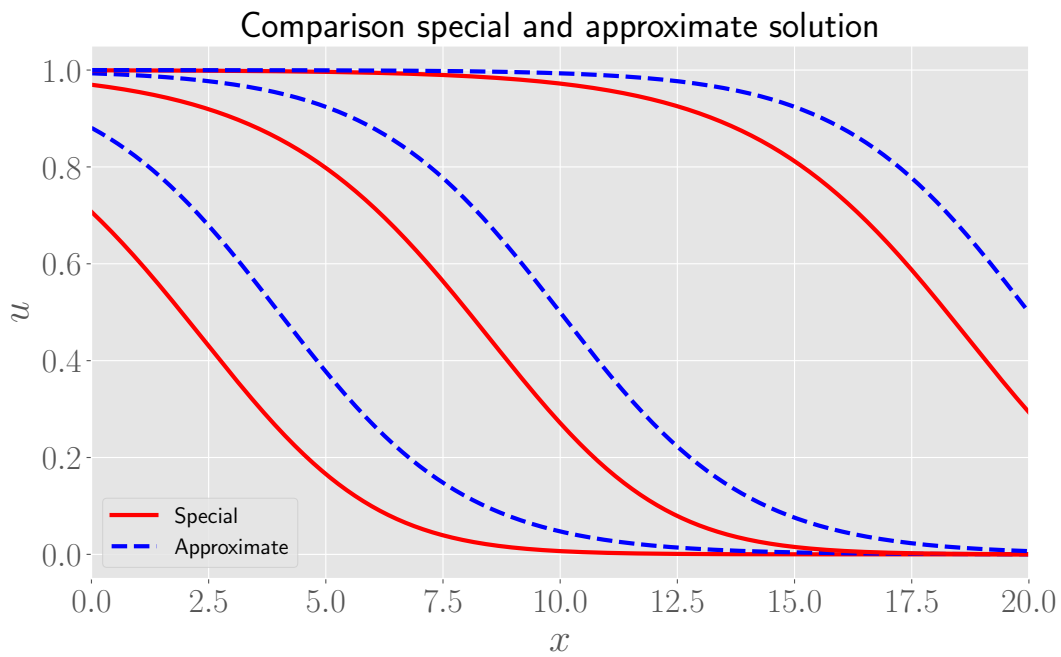


Figure 8.3.3: Comparison between special solution and approximate solution. Times shown are (from left to right) $t = 2, 5$ and 10 .

9 Pattern formation

In this exercise on pattern formation and Turing instabilities, we will consider the Brusselator model, a toy-model for the Belousov-Zhabotinsky reaction. The differential equations of the Brusselator are given by

$$\frac{\partial u}{\partial t} = a - (b + 1)u + u^2v + D_u \frac{\partial^2 u}{\partial x^2} \quad (9.0.1)$$

$$\frac{\partial v}{\partial t} = bu - u^2v + D_v \frac{\partial^2 v}{\partial x^2}, \quad (9.0.2)$$

and we set the parameters equal to $a = 1.5$, $D_u = 2.8$ and $D_v = 22.4$ below. We follow the general approach presented during the lecture (or in Chapter 2 of *Mathematical Biology* by Murray [4]) and non-dimensionalize the above equations. For this, we introduce a characteristic length-scale L for the problem, and set

$$\gamma \equiv \frac{L^2}{D_u}, \quad t^* \equiv \frac{1}{\gamma}t, \quad x^* = \frac{x}{L}, \quad d = \frac{D_v}{D_u}. \quad (9.0.3)$$

Note that for general systems, γ also contains a rate such that it has a dimension of time, but in our reactions, the rates are equal to one. The above equations become

$$\frac{\partial u}{\partial t^*} = \gamma(a - (b + 1)u + u^2v) + \frac{\partial^2 u}{\partial(x^*)^2} \equiv \gamma f(u, v) + \frac{\partial^2 u}{\partial(x^*)^2} \quad (9.0.4)$$

$$\frac{\partial v}{\partial t^*} = \gamma(bu - u^2v) + d \frac{\partial^2 v}{\partial(x^*)^2} \equiv \gamma g(u, v) + d \frac{\partial^2 v}{\partial(x^*)^2}. \quad (9.0.5)$$

Below, we will drop the asterisks in these equations for notational simplicity.

9.1 Homogeneous steady state solutions

We first calculate the homogeneous steady state (HSS) solutions, which means we set $D_u = 0 = D_v$, and set both equations above equal to zero. This gives the system of equations

$$\begin{cases} a - (b + 1)u + u^2v &= 0 \\ u(b - uv) &= 0. \end{cases} \quad (9.1.1)$$

If $u = 0$, then the first equation gives $a = 0$, which is not possible. Hence the second equation gives $uv = b$, and the first equation becomes

$$a - (b + 1)u + b = a - u = 0, \quad (9.1.2)$$

such that the homogeneous steady state solution is unique and given by

$$(u_0, v_0) = \left(a, \frac{b}{a} \right). \quad (9.1.3)$$

The Jacobian for the homogeneous system is

$$J(u, v) = \begin{pmatrix} -(b+1) + 2uv & u^2 \\ b - 2uv & -u^2 \end{pmatrix}, \quad (9.1.4)$$

such that the Jacobian evaluated at the HSS is

$$J \equiv J(u_0, v_0) = \begin{pmatrix} b-1 & a^2 \\ -b & -a^2 \end{pmatrix} \equiv \begin{pmatrix} f_u & f_v \\ g_u & g_v \end{pmatrix}, \quad (9.1.5)$$

where we have defined f_u to be the u -derivative of function f evaluated at the HSS et cetera. This implies we have to require

$$\text{tr } J(u_0, v_0) = b - 1 - a^2 < 0, \quad \det J(u_0, v_0) = a^2 > 0, \quad (9.1.6)$$

such that the HSS is stable, as required in the theory of pattern formation in reaction-diffusion systems. Note that the condition on the trace restricts b to $b < 1 + a^2$, while the determinant condition is certainly satisfied.

We can interpret u and v to represent the concentrations of two morphogens A and B . If we want to have pattern formation, we should have $J_{11} > 0$ and $J_{22} < 0$, which gives the additional constraint $b > 1$. Hence A is an activator and B a repressor, and B diffuses faster compared to A . The situation now resembles local activation and long range inhibition. From the lecture, we know that this type of system is able to produce patterns from diffusion-driven instabilities, which we will now explore.

9.2 Turing instability

As seen during the lecture, patterns can evolve from a diffusion driven instability (*Turing instability*) under certain conditions. This means that the HSS becomes unstable once we consider the full reaction diffusion system. Defining

$$\mathbf{w} = \begin{pmatrix} u - u_0 \\ v - v_0 \end{pmatrix}, \quad (9.2.1)$$

the linearisation is

$$\frac{\partial \mathbf{w}}{\partial t} = \gamma J \mathbf{w} + D \nabla^2 \mathbf{w}, \quad D = \begin{pmatrix} 1 & 0 \\ 0 & d \end{pmatrix}. \quad (9.2.2)$$

Now, let \mathbf{W} be the solution of the time-independent eigenvalue equation

$$\nabla^2 \mathbf{W} + k^2 \mathbf{W} = 0, \quad (9.2.3)$$

with eigenvalue k , and suppose the solution satisfies no-flux boundary conditions. This is chosen such that the system has no external input and the observed patterns are showing

self-organisation in the system. Since we are linearising around the HSS, the general solution is given by the sum

$$\mathbf{w} = \sum_k c_k e^{\sigma_k t} \mathbf{W}_k, \quad (9.2.4)$$

where σ_k is the *growth rate*. The growth rates are the eigenvalues of the matrix $\gamma J - k^2 D$, which is

$$\gamma J - k^2 D = \begin{pmatrix} \gamma f_u - k^2 & \gamma f_v \\ \gamma g_u & \gamma g_v - dk^2 \end{pmatrix}, \quad (9.2.5)$$

so the σ_k are roots of the characteristic polynomial

$$\det(\gamma J - k^2 D - \sigma_k) = 0. \quad (9.2.6)$$

The characteristic polynomial is

$$\sigma_k^2 + [k^2(1+d) - \gamma(f_u + g_v)] \sigma_k + h(k^2) = 0, \quad (9.2.7)$$

where $h(k^2)$ is the polynomial

$$h(k^2) = dk^4 - \gamma(df_u + g_v)k^2 + \gamma^2 \det J. \quad (9.2.8)$$

If we fill in the results that we obtained for the Brusselator model, this polynomial becomes

$$h(k^2) = dk^4 - \gamma(d(b-1) - a^2)k^2 + \gamma^2 a^2. \quad (9.2.9)$$

Since morphogenesis requires that the HSS becomes unstable if diffusion is taken into account, we require that equation (9.2.7) has at least one solution with positive real part. This is possible if (i) the coefficient in front of σ_k in the characteristic polynomial is negative for some $k \neq 0$, or (ii) if $h(k^2) < 0$ for some $k \neq 0$. However, (i) can never occur, since this coefficient is always positive (recall that $f_u + g_v < 0$ as we required that the HSS is stable if diffusion is neglected) and so (ii) must be fulfilled. Since $h(k^2)$ is a parabola, the function becomes negative first at the minimum of $h(k^2)$, which is

$$k_m^2 = \gamma \frac{df_u + g_v}{2d} = \gamma \frac{d(b-1) - a^2}{2d}. \quad (9.2.10)$$

Since this must be positive, we also deduce the requirement $df_u + g_v > 0$. Together with the constraint that $f_u + g_v < 0$ found earlier, the range of b is restricted to

$$1 + \frac{a^2}{d} < b < 1 + a^2. \quad (9.2.11)$$

The minimum of h is by definition equal to $h(k_m^2)$ and hence

$$h_{\min} = \gamma^2 \left[\det J - \frac{(df_u + g_v)^2}{4d} \right]. \quad (9.2.12)$$

At the bifurcation point, when $h_{\min} = 0$, this equation gives

$$\det J = \frac{(df_u + g_v)^2}{4d}, \quad (9.2.13)$$

and this allows us to determine the critical value b_c for the bifurcation parameter. For the Brusselator model, equation (9.2.13) becomes

$$a^2 = \frac{(d(b-1) - a^2)^2}{4d}, \quad (9.2.14)$$

which gives the following quadratic polynomial in b

$$d^2b^2 - 2d(d+a^2)b + (d-a^2)^2 = 0. \quad (9.2.15)$$

There are two solutions, namely

$$b_{\pm} = \frac{d+a^2 \pm \sqrt{(d+a^2)^2 - (d-a^2)^2}}{d} = \left(1 \pm \frac{a}{\sqrt{d}}\right)^2. \quad (9.2.16)$$

However, due to the restrictions on b , only one solution is kept. Indeed, expanding the square, we find

$$b_{\pm} = 1 + \frac{a^2}{d} \pm \frac{2a}{\sqrt{d}}, \quad (9.2.17)$$

such that b_- does not lie in the allowed range for b . We conclude that

$$b_c = \left(1 + \frac{a}{\sqrt{d}}\right)^2 \quad (9.2.18)$$

is the critical value for the bifurcation parameter. The critical wavelength is

$$k_c^2 \equiv k_m^2(b=b_c) = \gamma \frac{d \left[(\sqrt{d} + a)^2 - 1 \right] - a^2}{2d} \quad (9.2.19)$$

We can verify the numerical calculations graphically. Using the values of the parameters mentioned in the beginning, we get $b_c = 2.3419$ and b is restricted to the range $1.2813 \leq b \leq 3.25$. The critical wavelength squared depends on γ in our calculations above, and for $\gamma = 1$ (which is the value for γ we use in the two plots below) is equal to $k_c^2 = 0.5303$. For example, in Figure 9.2.1, we plot the functions $h(k^2)$. The figure clearly shows that the graph crosses the k^2 -axis at the critical value b_c , and has a zero at the critical wavelength squared. Figure 9.2.2 shows that at the bifurcation point, a range of wavelengths become unstable. This is indeed the predicted Turing instability from above.

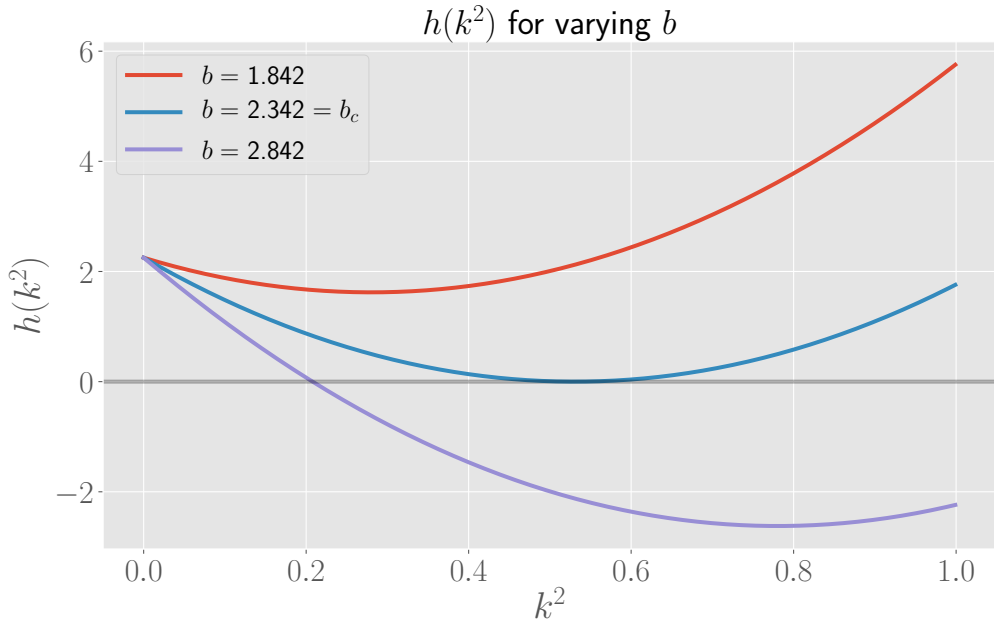


Figure 9.2.1: Plots of the functions $h(k^2)$, for varying values of b . Above the critical value b_c , the parabola becomes negative for a certain range.

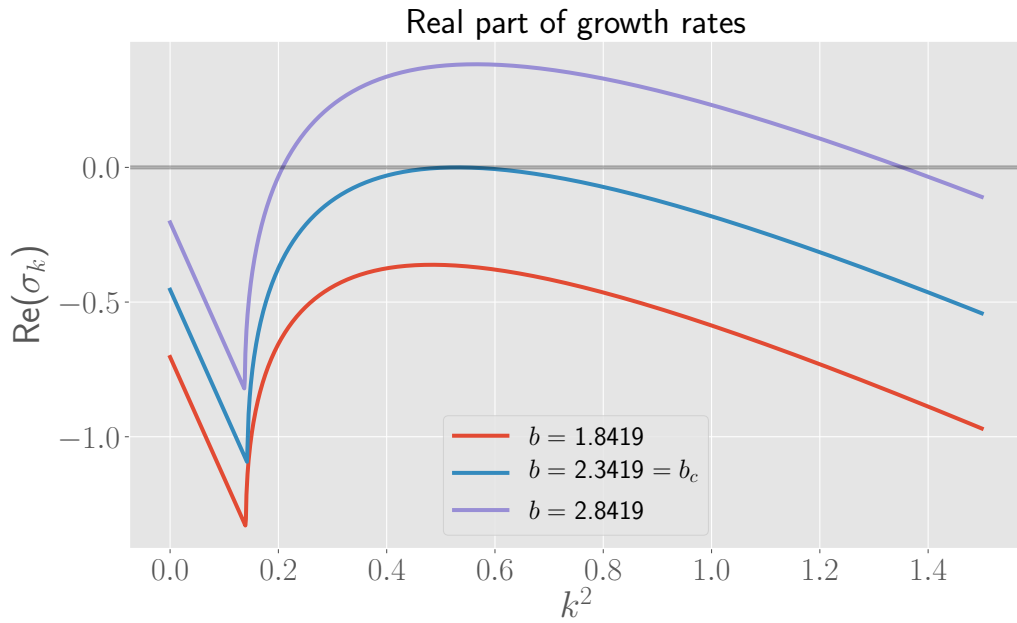


Figure 9.2.2: Real part of the growth rates σ_k . Above the bifurcation point $b = b_c$, a range of the wavelengths becomes unstable.

9.3 Spatiotemporal dynamics

We investigate the behaviour of the system while varying the bifurcation parameter b , the initial condition and the domain size L . We let the domain of x be of the form $[0, L]$ and work with no-flux boundary conditions. One initial condition we explore is the sine wave perturbation, where a wave-like perturbation is added on top of the HSS. Because of the boundary conditions, the wave should have the form

$$u_{\text{in}}(x) = a + A \cos\left(\frac{n\pi x}{L}\right), \quad n \in \mathbb{Z}, \quad (9.3.1)$$

where A gives the amplitude of the perturbation and is assumed to be small compared to the HSS. A similar initial condition holds for v , with a replaced by b/a . Another initial condition we explore is white noise. Here, one draws random numbers from a certain distribution and adds these as perturbation on top of the HSS. We choose for a Gaussian distribution with mean zero and standard deviation A (again characterizing the ‘strength’ of the perturbation and assumed to be small compared to the HSS).

To perform the numerical integration, we have chosen to adapt the code written for assignment 8 to be able to solve two component systems, such as the model currently considered. However, given that the discretization of space and time must be fine enough to reduce errors during the calculations, which also implies a larger computational cost, using a built-in solver of Python could make the calculations more precise and faster. Nevertheless, Figure 9.3.1 clearly shows that the system indeed exhibits pattern formation at late times (the figure uses $b = b_c + 0.1$ and $t = 5$) and so we conclude that our solver is adequate for the current problem.

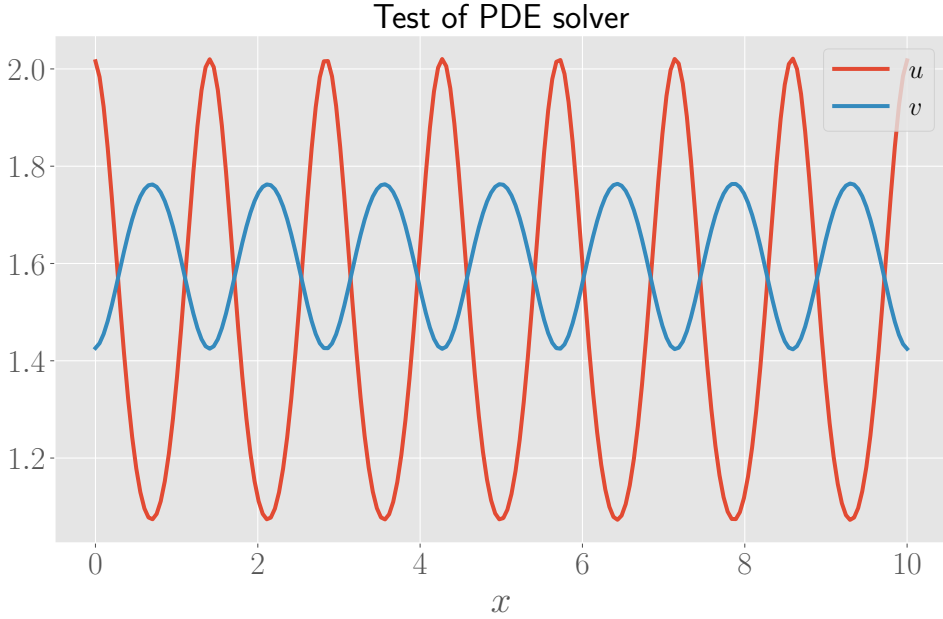


Figure 9.3.1: Test of the PDE solver written for this assignment, with $b = b_c + 0.1$. The system clearly self-organizes into a pattern formation.

Figure 9.3.1 also shows the type of pattern that the system develops. Maxima of u and minima of v are located at the same points and vice versa. This type of pattern is characteristic of a Jacobian (for the homogeneous system) with sign pattern

$$\begin{pmatrix} + & + \\ - & - \end{pmatrix}, \quad (9.3.2)$$

which is indeed the sign pattern of our Jacobian matrix. The other case, where the signs of the off-diagonal parts are swapped, has a pattern where the maxima (and minima) of u and v are aligned with each other [4, p.88].

The wavelength of the pattern can be estimated from the graph and gives $\omega \approx 1.4$. We can compute the critical wavelength, which is defined as $\omega_c = 2\pi/k_c$. For $b = b_c + 0.1$ and using $L = 10$ in the definition of γ , this gives $\omega_c \approx 1.3801$ which agrees with the above plot.

In the exploration of the dynamics below, the red curve will denote the concentration of u , and the blue curve the concentration of v , as in Figure 9.3.1. We will integrate the solutions until time $t = 5$ and by default set $L = 10$ and $b = b_c + 0.1$ and use the sine wave perturbation with $n = 1$ as initial condition. This initial condition can be seen as a disturbance due to a travelling wave inside the system which initiates the pattern formation, since the shape of this initial condition resembles a travelling wave, as seen in Figure 9.3.2. As the above example shows, $t = 5$ can be considered a ‘late time’ for this system, meaning that, if the conditions permit it, patterns are already formed at this timescale. Of course, these can change depending on which variation is performed.

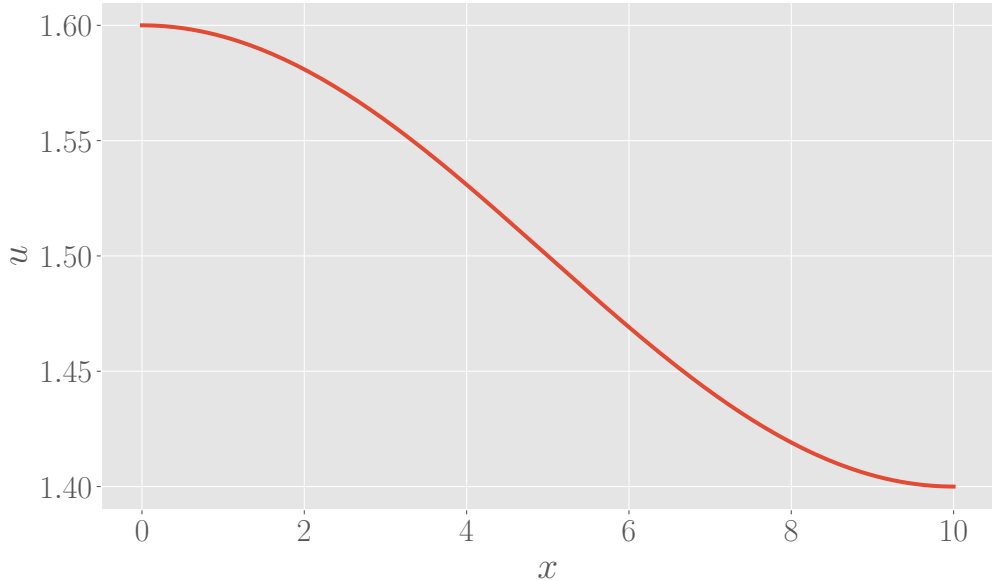


Figure 9.3.2: Sine wave perturbation for u (with HSS $u_0 = a = 1.5$) as initial condition, with $n = 1$. The shape resembles a travelling wave, which disturbs the system and initiates the pattern formation

9.3.1 Varying b

We vary the bifurcation parameter b , with values $b = 1.5, 2, 2.5$ and 3 : the first two values are below b_c , while the other two are above b_c . The result is shown in Figure 9.3.3. As expected, when b is below the critical value, all wavelengths are stable and perturbations die out over time and at late times, the solutions tend towards the HSS. When b is above the critical value, the perturbations evolve towards a pattern.

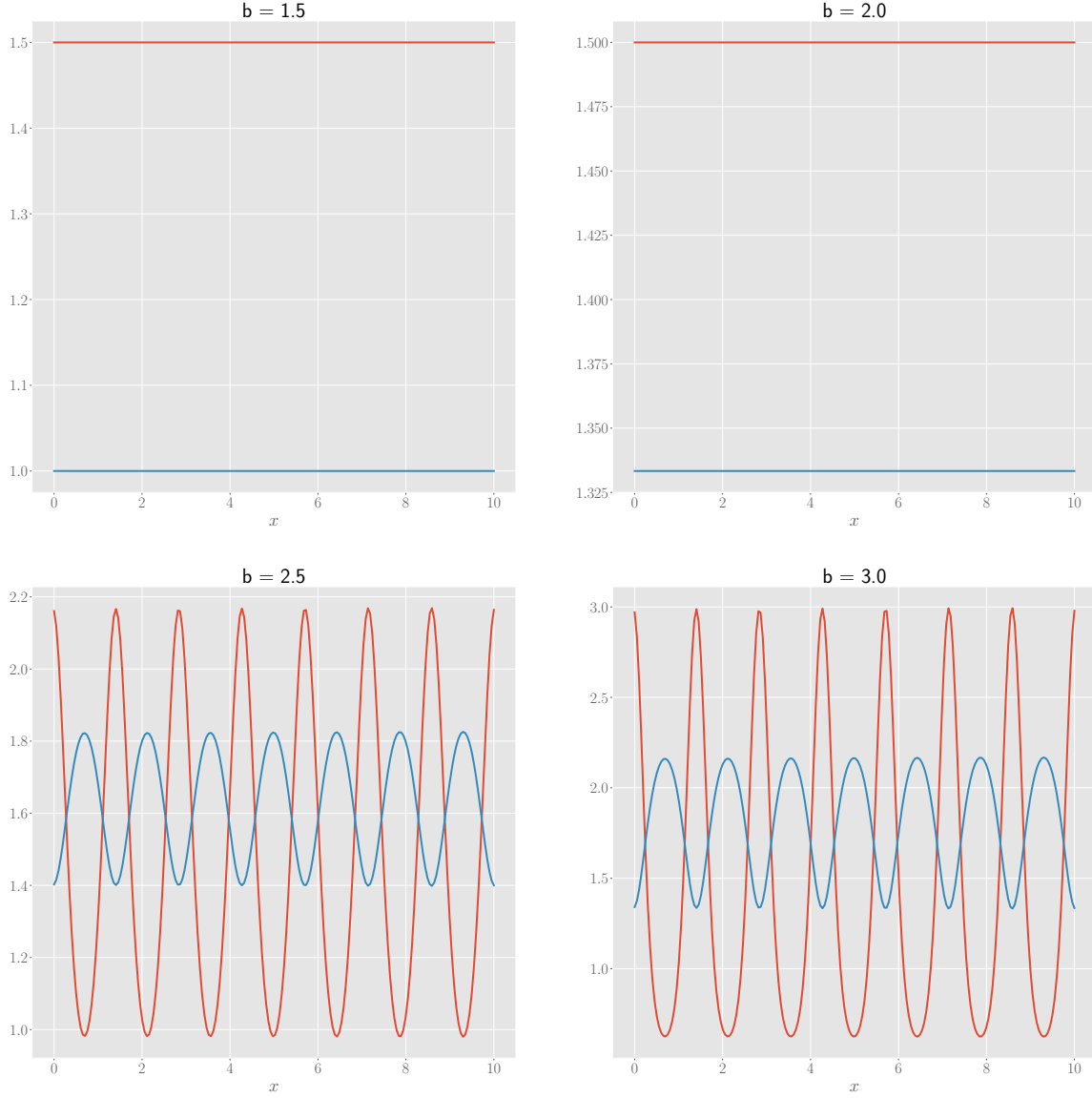


Figure 9.3.3: Varying the parameter b in the model.

9.3.2 Varying initial condition

We now look at the effect of varying the initial conditions. Above, we presented two possible initial conditions: sine waves and white noise. Both will be discussed and varied. For the sine waves, we can play around with the integer n from equation (9.3.1), which essentially determines the amount of wavelengths that fit in the domain. For the white noise perturbations, we will vary the amplitude of the perturbation A .

The variation of sine wave initial conditions is shown in Figure 9.3.4. Overall, it appears

as if this does not change the pattern much. The values at the boundaries can change (either a local maximum or local minimum), but the wavelength of the pattern does not change much. The amplitudes of the pattern do not change when n is varied. For $n = 25$, not all peaks of the pattern have an equal height, although it is difficult to know the cause behind this. It is likely that this is the result of computational errors and could be integrated out at later times. We conclude that the system is very stable against the variation of n in the initial condition.

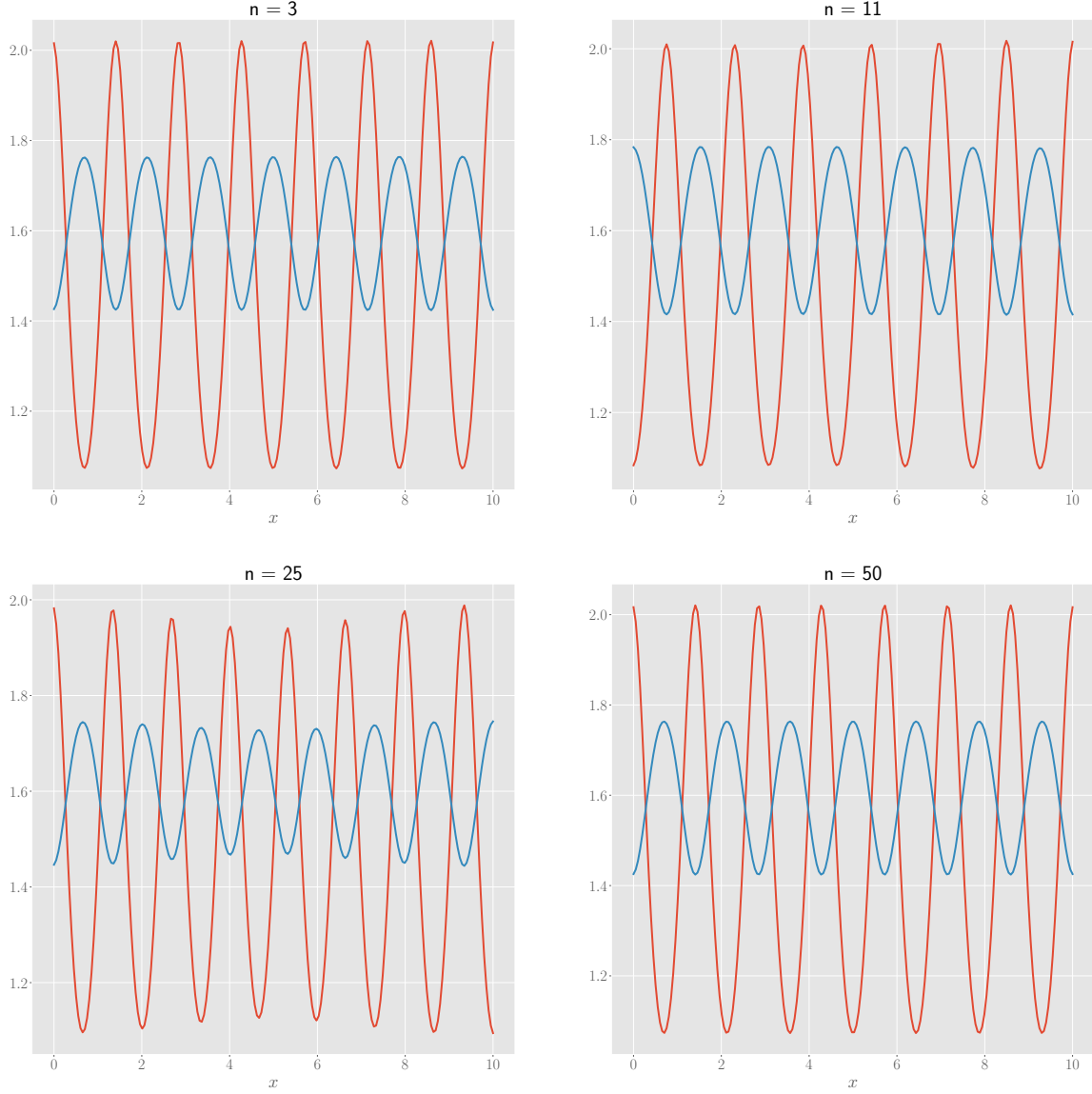


Figure 9.3.4: Varying n in the initial condition of sine wave perturbations.

The variation of the amplitude of white noise is shown in Figure 9.3.5. Essentially the same discussion as above can be repeated. The only difference is that the amplitudes of

the pattern seem less stable against this variation, although the effect is rather small. In the Python notebook, we also repeat the analysis with a uniform distribution in the interval $[-A, A]$ rather than a Gaussian distribution from which the white noise samples are drawn. The results are almost identical, such that it appears that the choice of distribution does not alter the pattern. Hence we conclude that the system is very stable against a change of the initial conditions in general.

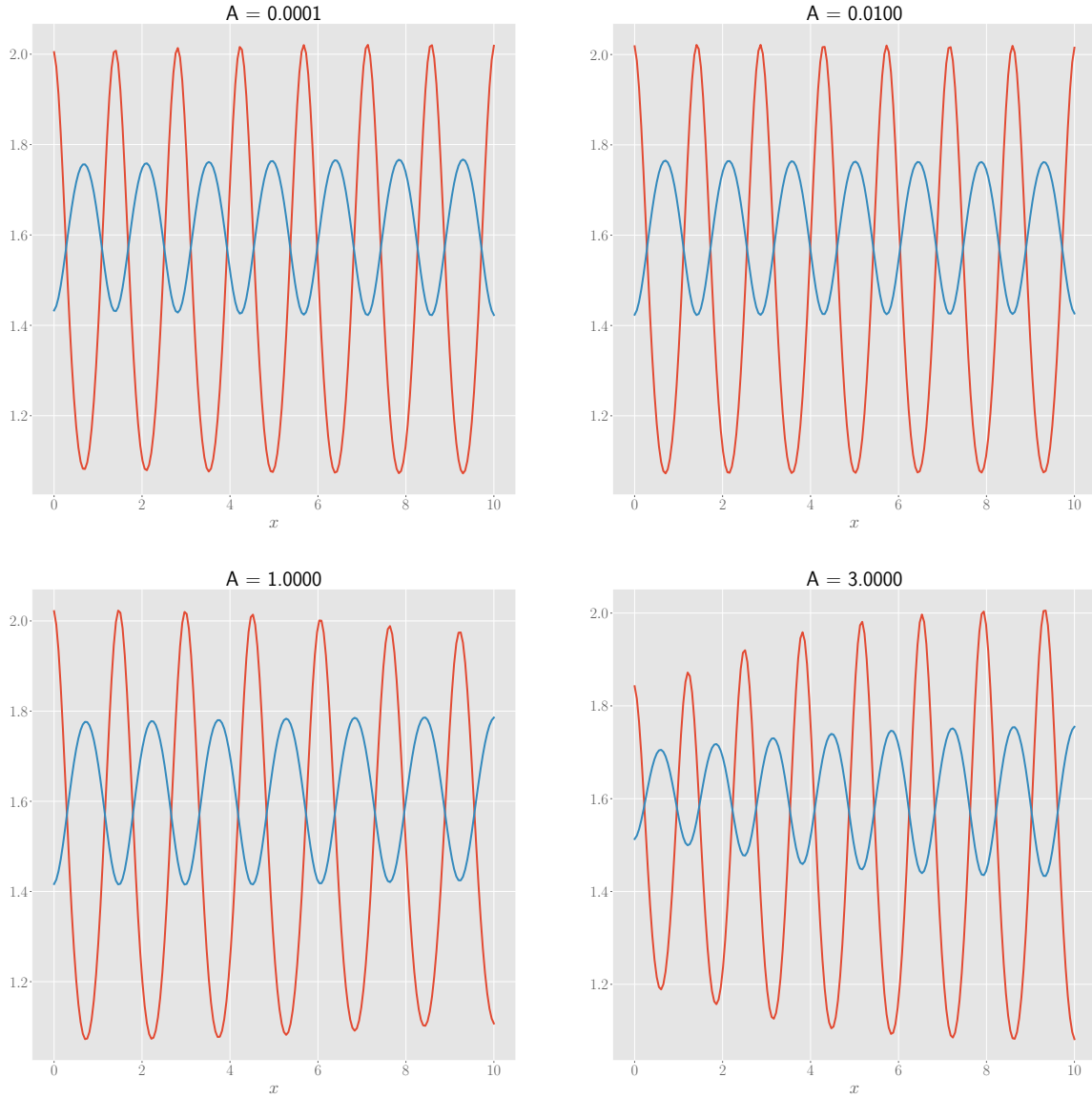


Figure 9.3.5: Varying A , the standard deviation of the Gaussian distribution, in the white noise perturbation.

9.3.3 Varying domain size

Figure 9.3.6 shows the effect of varying the domain size L . In the figure, we look at increasing values of L , so larger domains. We see that varying the domain size has a more significant impact compared to the variation of the initial conditions. While the shape of the pattern for $L = 15$ is similar to the one for $L = 10$, we see that the pattern for $L = 20$ has a different shape, in which the solution for u has some sort of deeper structure, where the maxima differ in height in some sort of regular way. Of course, it could be that the convergence towards the final pattern is not yet complete, hence explaining the sub-structure of the plot. However, a plot in the notebook where we integrate until $t = 10$ (compared to $t = 5$ in the figure below) gives a result which is almost identical in shape to the plot below, excluding this possibility. When we use a different initial condition, the same pattern is observed as well. Note also that the wavelength of the pattern changes if L is changed. This is due to the fact that the critical wavenumber, which has the largest real part of its growth rate and hence is expected to give the wavelength of the final pattern, depends on γ , which on itself depends on L .

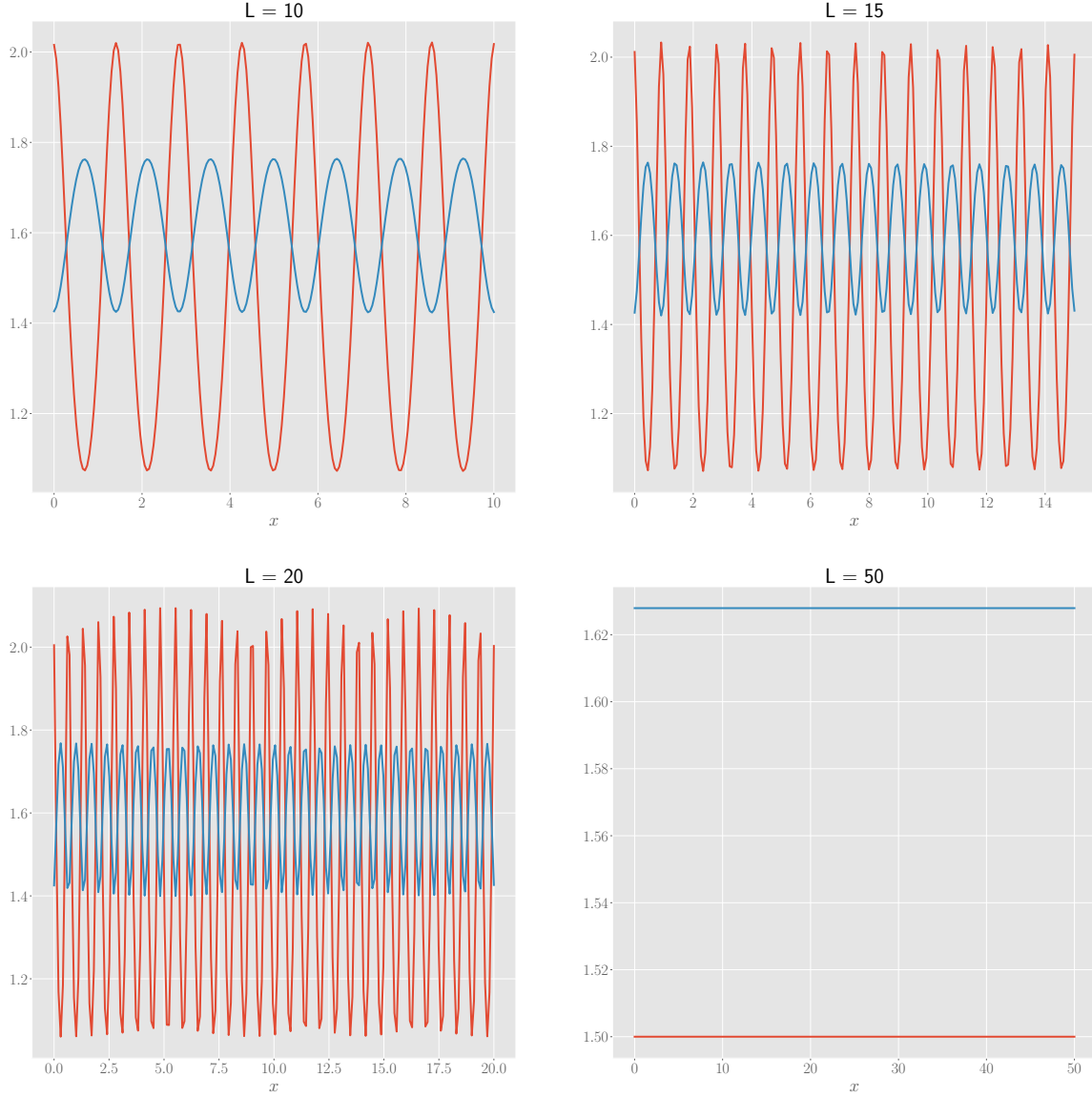


Figure 9.3.6: Varying the domain size L of the system.

Even more striking is that no pattern is formed at all for $L = 50$. In the Python notebook, we plot the solution for an initial condition with $n = 10$ (rather than $n = 1$) or where the integration time is increased to $t = 10$ (rather than $t = 5$), but still no pattern formation is observed. It seems that the pattern starts to change around $L = 20$ and gets completely disrupted for a value of L between 20 and 50. This is confirmed by Figure 9.3.7, where it is clear that for L between 20 and 30, there is still pattern formation, but the shape of the pattern becomes highly irregular (possibly because the discretization of space should be improved at higher L). For some L between 30 and 35, the system no longer tends towards a pattern solution.

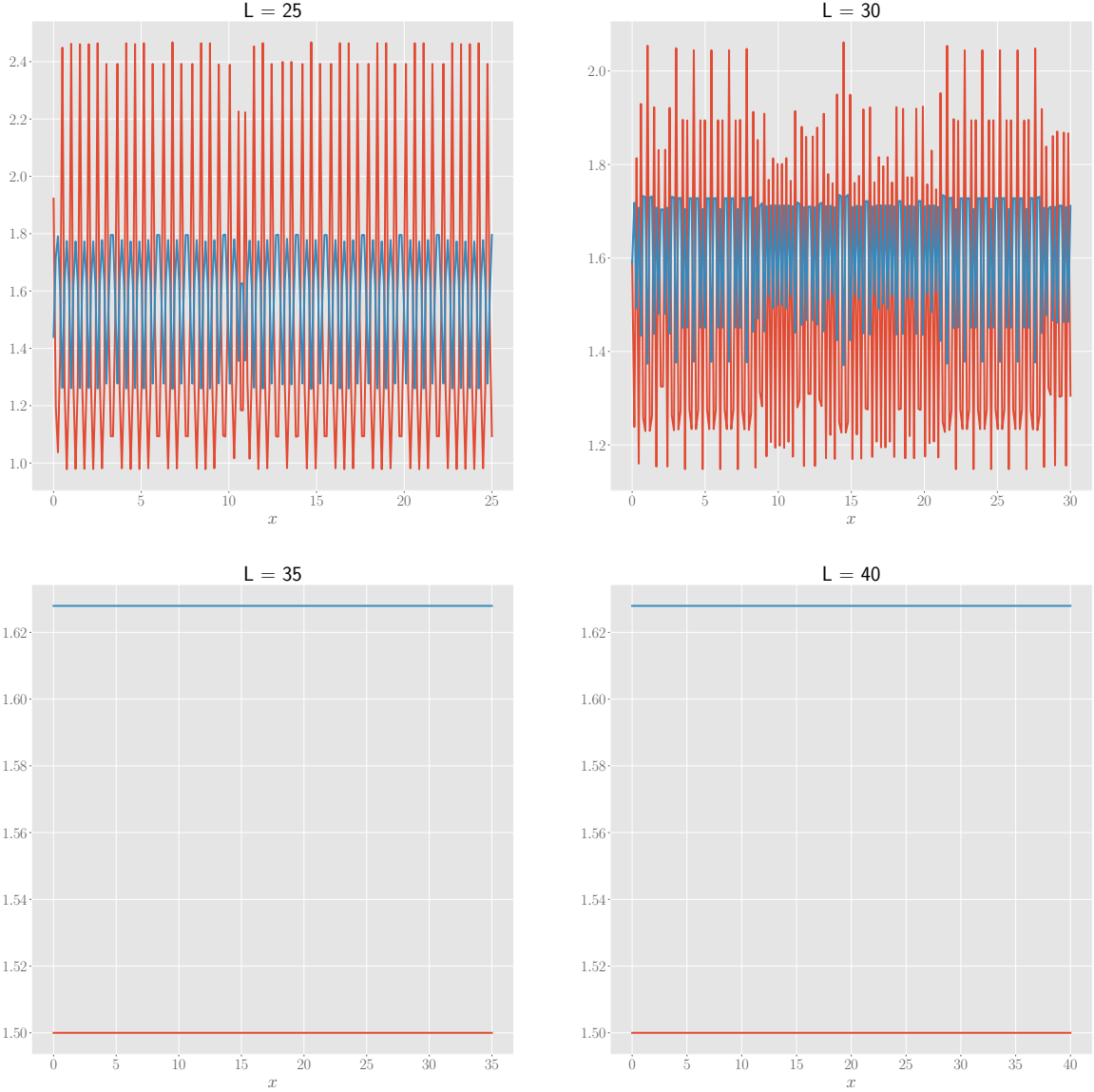


Figure 9.3.7: More variations on the domain size L , between 20 and 50, demonstrating that pattern formation stops if the domain size becomes too large.

It could be that, whereas it was unimportant for small domain sizes, the initial condition could have a significant importance for the pattern formation at large domain sizes. As observed during our analytic calculations, there is a range of unstable wavenumbers, i.e. there are bounds k_-^2, k_+^2 such that a perturbation with wavenumber $k_-^2 < k^2 < k_+^2$ is unstable. These bounds are the zeroes of $h(k^2)$, so one finds from the general formula derived in the previous section

$$k_{\pm}^2 = \frac{\gamma}{2d} \left[(df_u + g_v) \pm \sqrt{(df_u + g_v)^2 - 4d \det J} \right]. \quad (9.3.3)$$

These bounds are hence proportional to γ . If we compute these bounds for $L = 50$ and $b = b_c + 0.1$, we find that a sine wave perturbation with for example $n = 350$ has a wavenumber $k = n\pi/L$ which (when squared) lies between these bounds, and hence should be an unstable wave number. However, the numerical integration does not agree with this result and does not develop a pattern.

One possible explanation is the fact that the unstable wavenumbers are quantised in systems with a finite domain, with $k = n\pi/L$. Since the range of unstable wavenumbers is shifted towards large values, we need larger values for n , but this implies that the distance between unstable wavenumbers becomes larger, which possibly makes it more difficult for the system to converge towards a pattern. Another possible explanation is that k_c increases with γ (and hence L) such that the wavelength of the pattern decreases for increasing domain sizes (see for example Figure 9.3.6). It could be that if ω_c is too small, it becomes impossible for the system to self-organize into a pattern on such a small scale.

We want to stress that one should be careful in concluding that no pattern is formed at high L , since this can not be made rigorous by an analytic calculation. Moreover, we could continue the numerical exploration in the high L region, but in order to reduce computational errors, we should make our discretization of space finer, which means the calculations will take a lot of time. Hence we conclude the exploration of high domain sizes with the observation that above some L , pattern formation becomes difficult, perhaps even impossible, although this is hard to prove exactly.

Instead of extending towards higher domains, we also investigated the behaviour of the system in smaller domain sizes, i.e. with $L \leq 10$. It turns out that if the domain is too small, no patterns are formed. Contrary to the high L regime, this can be argued from an analytic point of view. Recall the range of unstable wavenumbers with bounds given by equation (9.3.3) and proportional to γ (therefore proportional to L^2). The unstable wavenumbers become quantised in finite domain systems with lowest possible wavenumber squared being π^2/L^2 . Hence if L is sufficiently small, there exist no (quantised) wavenumber in the range of unstable wavenumbers, such that no pattern is formed.

References

- [1] Uri Alon. *An introduction to systems biology: design principles of biological circuits*. CRC press, 2019.
- [2] Enrico Carlon. Goodwin oscillator. https://www.youtube.com/watch?v=yY4wZTJM74g&ab_channel=ECarlon.
- [3] Nick Metropolis, ML Stein, and PR Stein. On finite limit sets for transformations on the unit interval. *Journal of Combinatorial Theory, Series A*, 15(1):25–44, 1973.

- [4] JD Murray. *Mathematical biology II: spatial models and biomedical applications*, volume 2. Springer-Verlag, 2001.
- [5] Steven H Strogatz. *Nonlinear dynamics and chaos: With applications to physics, biology, chemistry, and engineering*. CRC press, 2018.
- [6] John J Tyson. Biochemical oscillations. In *Computational cell biology*, pages 230–260. Springer, 2002.